UNIVERSITY OF CALIFORNIA
Los Angeles

Phase Change near the Contact-line:
A Bio-inspired Approach

Dissertation Submitted in Partial Satisfaction of the Requirements for

Degree of Doctoral of Philosophy

in Mechanical Engineering

by
Elaheh Alizadeh-Birjandi

2019

Abstract

Phase Change near the Contact-line:
A Bio-inspired Approach

By

Elaheh Alizadeh-Birjandi

Doctor of Philosophy in Mechanical Engineering

University of California, Los Angeles, 2019

Professor H. Pirouz Kavehpour, Chair

The processes of phase transformation continue to affect our natural and industrial worlds in a range of scales from large-scale lava flows in nature to micro-and nano- scale applications in industry. Enhancement of the knowledge framework of these processes and understanding the accompanying physical phenomena are keys to resolve challenges in scientific research and obtain rational engineering evaluations for a wide range of industrial application such as 3D printing, rapid prototyping, thermal spray coating, power plants, aerospace and turbine industries. A great deal of work has been done in the past few decades on these matters, and significant progress has been made; however, much of it remains unraveled. The main difficulty stems from the intertwined effect of heat transfer, fluid dynamics, and phase change physics with the combination of complex wetting behaviors of the contact-line. In this thesis, we focus on solidification and condensation near the contact-line. For solidification near the contact-line, we have studied the onset of solidification and its relevant physical parameters and explored ways to delay the start of solidification inspired by the unique ice-resisting abilities of penguin feathers and certain plant leaves. The dynamics of solidification and spreading is also studied and new hypothesis is introduced to explain the contact-line pinning due to solidification. Finally, in

condensation near the contact-line, we have introduced a novel biphilic surface with large scale cost-effective manufacturing process and analyzed and compared its heat transfer efficiency and water droplet mobility to traditional hydrophobic and hydrophilic structures.

The dissertation of Elaheh Alizadeh-Birjandi is approved.

Jeff D. Eldredge

Adrienne G. Lavine

Joseph M. Teran

Hossein Pirouz Kavehpour, Committee Chair

University of California, Los Angeles

2019

Dedication

To my parents, my everlasting source of inspiration. Thank you for all your sacrifices, unconditional love, and unwavering support.

Table of Contents

List of Figures

List of Tables

Acknowledgment

I would like to thank my advisor Professor Pirouz Kavehpour for supporting me during these past five years with his constructive guidance, unlimited attention, and encouragement. I extend my thanks to Professor Jeff. D. Eldredge, Professor Adrienne Lavine, and Professor Joseph M. Teran for serving on my thesis committee and for their brilliant comments and suggestions.

I would like to thank my lab mates for their continued support. They are all a fun bunch with lots of enthusiasm and optimism, and they made my experience in graduate school and in the lab exciting and fun.

Last but not least, I would like to express my deepest gratitude to my family. This dissertation would not have been possible without their warm love, sacrifice, continued patience, and endless support.

Vita

2014	B.S (Mechanical Engineering), Sharif University of Technology, Iran
2015	M.S (Mechanical Engineering), University of California, Los Angeles

1. Introduction

1.1. Motivation

Understanding the physics of the phase change at different scales and for different applications is essential in improving those applications through controlling the course and outcome of these processes. Here, we are going to discuss some of these applications and explain how understanding the phase transformation processes can be advantageous in improving these applications.

The three-dimensional fabrication, 3D printing, is used in diverse areas including biomaterials fabrication the vitality of which in saving patient lives is unmatched. Solidification of molten materials is the building block in 3D printing. The shape of each droplet and the apparent contact angle of the liquid deposited control the shape and structure of the final part. In order to 3D print a structure that has relevant size, shape, and structural integrity, understanding the physics behind the spreading and solidification of liquid droplets on solid substrates is highly critical.

Another important example is the aircraft industry. In aircraft industry, solidification and adhesion of liquid droplets can cause severe complications for airplanes. The result of numerous experimental studies has shown that even a very small amount of ice accumulation at critical locations on an aircraft can have a negative impact on performance. Some of the observed effects include: a substantial decrease in lifting capability; a reduction in control surface effectiveness; frequent occurrences of control surface anomalies; an increase in drag; and, in some cases, a reduction in engine performance and stability. Ground-based de-icing is both expensive and time consuming. In this method, a mixture of a chemical is heated and sprayed under pressure to remove ice on the aircraft. The toxicity of the deicing fluids is an environmental concern, and

also the frequent use of these chemicals may cause residues to collect in aerodynamic quiet areas or cavities. The development of surfaces that resist icing both on the ground and in the air is therefore a significant advantage for both commercial and military aircraft.

Ice accretion can also reduce the performance of wind turbines considerably by affecting the aerodynamic profile of the blade and finally the operational loading of the entire rotor leading to significant energy loss and reduction of power production. Current de-icing methods used for turbines require the turbine to be stopped or get their power from turbine itself, which decreases the proficiency. A number of strategies have been developed in the past to find suitable materials to delay or prevent ice formation; none of them though have proven efficiency. Knowledge of imperative parameters inherent in the droplet spreading and subsequent phase change is essential for controlling and hopefully preventing the growth of ice on airplane parts or turbine blades.

Lastly, the industrial condensers are another application where understanding phase change processes can lead to significant improvements. One of the main technical challenges in a variety of industrial fields including aircrafts, power plants, and water desalination systems is the effective discharge of excessive heat generated inside the system. From a thermal management point of view, for majority of these industrial applications, condensation is considered the optimum way to remove waste heat from the system as condensation provides high heat transfer rate due to the phase change process. These condensers are not very efficient, and several researchers have tried to address the issues and find ways to improve this efficiency, which is equivalent to savings millions of dollars in annual investments and operating costs. Currently, the majority of industries rely on film-wise condensation for waste heat removal. However, film-wise condensation offers low heat transfer coefficient due to thermal resistance imposed by the liquid layer as when the film is formed, it acts as a barrier to thermal transfer and impedes the

continuous heat transfer from the condensing surface. One way to improve the efficiency of condensation is to enhance drop-wise condensation on the condensing surfaces. Unlike film-wise condensation, in drop-wise condensation, there is a continuous surface renewal by falling drops resulting in at least 10-fold enhancement in heat transfer rate compared to the film-wise condensation.

1.2. Background

The phase change study of droplets is a multi-physics problem, which requires solving the heat transfer and fluid dynamics equations simultaneously considering the wetting behavior of the contact line and thermal characteristics of the droplet at all phases. Coupling of these physical phenomena, along with the fact that dynamic wetting operates on scales ranging from macroscopic to molecular render the physical understanding of the process challenging.

From a scientific point of view, phase change of droplets near the contact-line analysis is an intricate free-boundary problem with moving contact line and temperature gradient. Besides, continuum formulation of both heat transfer and fluid flow contains singularities, even though the stress singularity can be avoided, the heat flow singularity cannot be resolved.

From theoretical standpoint, a set of equations including continuity, energy of solid and liquid, and Navier-Stokes should be solved to provide accurate description of the process. The precise answers to these equations are practically impossible due to the presence of multiple parameters, such as conduction through a contact resistance, deforming geometry of drops, solid-liquid transformation, and two distinct singularities. The two mathematical singularities at the contact line are introduced by fluid dynamics and heat flux. No theoretical mechanism has been suggested to circumvent the heat flux singularity at contact point and immediate adjacent region,

unlike stress singularity. In order to avoid the heat flux singularity, Schiaffino and Sonin[1,2] proposed the cut-off distance that brings their continuum theory into agreement with experimental results. Although many theoretical studies have been done in this field, little can be found to address evolution of drop's contact angle and diameter during spreading and phase change.

A common interest in the drop research field is to predict the maximum spreading diameter, which representing the maximum extent to which a drop can be deformed during spreading. In the case of non-isothermal spreading, the maximum diameter shows where the solidified material stops spreading. The maximum spreading is an important factor in determining the performance of 3D printers as well as the quality of the final structures and surfaces. Also, an accurate estimation of the maximum spreading is essential to predict the tendency of drop rebound because the surface energy at the maximum spreading is indicative of the energy available for receding. Prediction of the maximum spreading diameter has already been attempted by several authors using either completely empirical or semi-empirical models. All of the models employed are based on the energy balance of the drop. In all of these approaches the drop shape is assumed to be a disc at the instant when the drop diameter reaches its maximum value. Moreover, the total kinetic energy of the drop at this instant is assumed to vanish.

Analyzing the spreading diameter and contact angle of impact droplet becomes even more complicated when it is combined with phase change. Although, the experimental measurements of contact angle and radius variation during droplet impact and solidification are available in literature, which will be discussed in the following chapter, no analytical solution can be found to explain the phenomena behind the arrest of the moving triple contact line of the solidifying droplet.

Another concern in the phenomenon of solidification is to recognize the affecting parameters and determine methods to control the initiation and speed of the process. In some cases, solidification can lower the efficiency of the systems and cause unforeseen circumstances; therefore, many investigators are trying to find ways to impede solidification. For example, for structures working in high-humidity environments, ice formation and accumulation would lead to great energy loss, and finding surfaces that can resist icing is a challenge for many industries.

Finally, the condensation process in another area of interest due to its broad applications in industry. Efficiency of the thermal transfer during condensation strongly depends on the mode of condensation, namely drop-wise and film-wise condensation, where the former has at least one order of magnitude higher heat transfer efficiency. The mode of condensation is determined by the thermophysical properties of the condensing surface. Transition from film to drop wise condensation can improve the efficiency of thermal management applications and result in considerable savings in investments and operating costs by millions of dollars every year.

This thesis is devoted to the study of phase transformation at the contact-line. The main challenge is to obtain different parameters involved in contact-line phase change process with goal of controlling the onset and rate of these phenomena as well as improving their efficiencies.

1.3. Organization of Thesis

This thesis is focused on droplet phase change physics and is structured into two main sections, solidification and condensation. We begin with the study of solidification onset with the aim of obtaining the most efficient and practical way to control the initiation and speed of solidification and more specifically the freezing process inspired by nature. Chapter 3 is devoted to the study of drop spreading and solidification. A new hypothesis regarding the physical description of the

motion and arrest of contact-line is proposed and tested. The aim is to control and determine the final shape of the droplet after the solidification is complete and obtain the arrest footprint. The corresponding theoretical and experimental works are reviewed in this chapter. Finally, Chapter 4 focuses on studying drop-wise condensation and heat transfer enhancement using novel surfaces. A description of experimental facilities and details of condensation calculations are explained in this chapter as well. Conclusions are drawn in Chapter 5 and future directions are also mentioned.

2. Time Delay In Solidification Initiation

Ice adhesion and excessive accumulation on exposed structures and equipment are well known to cause serious problems in cold-climate regions. Atmospheric icing occurs when super-cooled water droplets come into contact with the surface of exposed structures, which may lead to material damage and socioeconomic costs in many areas of the economy, including power transmission and distribution, telecommunication networks, and aircrafts.

The aviation industry over the years has suffered many catastrophic accidents as a result of icing. Even a small amount of ice can change the pattern of flow and streamlines around the airplanes causing a significant change in lift and drag while adding to the weight of the airplane [3]. Ice accretion can also reduce the performance of wind turbines considerably by affecting the aerodynamic profile of the blade and adding to the operational loading of the entire rotor leading to a significant energy loss, reduction of power production, mechanical failure, and high amplitude structural vibrations due to the mass imbalance on the blades.

There are systems to prevent ice or to remove ice. The current de-icing techniques can be categorized into two groups: (1) active and (2) passive de-icing methods. Active de-icing techniques require an external source of energy, which can be in the form of mechanical, thermal, or electrical energy. Although these methods have high efficiency, they are extremely energy-intensive, they require the machine to be stopped to get de-iced or they get their power from the machine itself which reduces the efficiency of the system, e.g. hot air injection systems or resistive heaters [4].

Passive anti-icing surfaces or icephobic surfaces can be the solution to the icing problem; they are the area of great interest because of their significant economic, energy and safety implications in the prevention and easy removal of ice in many facets of society. The passive

anti-icing methods do not need an external energy to perform. They take advantage of the physical and chemical properties of the surface to eliminate or delay the ice formation. Lubricated surfaces, for instance, minimize the contact angle hysteresis and ice-adhesion through the application of an oil-layer on the surface. The issue with this method is that the oil-layer might be displaced or removed by the water or ice droplets; hence a continuous application of oil on the surface is required. Anti-freeze fluid is occasionally used as a substitute for oil. Although proven to be effective, the anti-freeze solution contains chemicals stimulating corrosion. Icephobic coatings, however, take advantage of surface chemical and topographic features [5] to reduce the adhesion strength to the surface and/or crystallization temperature of water.

The ice formation is a complex multi-physics process and this inherent complexity mostly emerges from the highly sensitive phase-change behavior of water making any effort to understand the whole process, factors involved, and ways to impede the freezing onset extremely challenging.

Nature-inspired surfaces have been the subject of interest in the past decade [6-13]. This chapter of this dissertation is focused on the study of the anti-icing properties in nature and its survival techniques encountering sub-zero temperatures and freezing conditions. Understanding the rationale behind the ice formation delay in biological species and the governing factors would serve as a guide towards designing practical ice-repellent coatings for industrial applications. An in-depth experimental and theoretical study on how these surfaces can prevent icing has been performed.

2.1. Delay of Ice Formation on Penguin Feathers

The work done in this chapter was inspired by penguins; they live in a bitterly cold place, where the air temperature can drop to -40 degrees Celsius and the winds can hurtle at speeds of 40 meters per second. Penguins are constantly diving in and out of the water and getting splashed by waves. Yet, even in these sub-zero conditions of Antarctica, macroscopic ice crystals do not form on their feathers. In this chapter, we reveal the secret behind penguins ice-resisting abilities, the unique nano-structures on their feathers. This nano-sized surface topography combined with the penguins' hydrophobic preen oil makes the feathers extremely icephobic. Experimental measurements showed a dramatic delay in the onset freezing of water droplets on cold-weather penguin feathers as compared to warm-weather penguin feathers, and the physic of this delay is explained through the development of a heat transfer model. The upshot of this study can be used to motivate the designs of biomimetic surfaces to minimize ice formation in extreme conditions for a number of important engineering applications; especially in the aircraft manufacturing industry as the ice accretion on aircraft can negatively affect the aerodynamic profile of wings and rotor blades, often with serious consequences.

2.1.1. Introduction

Penguins are flightless birds living in diverse geographical locations in the southern hemisphere. Humboldt penguins live in temperate zones near the equator whereas circumpolar species like the Gentoo, Macaroni, Emperor, and Adelie have adapted to the extreme cold in Antarctic regions, where air temperatures may reach −40°C with wind speeds of 40m/s and water temperatures around −2.2°C [14,15]. Penguins jump in and out of the water every day. Yet, no macroscopic ice formation can be observed on their feathers in nature or in captivity even on the

coldest days of the year. A better understanding of the origins of the amazing anti-icing ability of Antarctic penguins could help address one of the major challenges in the aerospace industry, ice formation and buildup on the surface of aircraft wings.

The results of numerous experimental studies have shown that even a very small amount of ice accumulation at critical locations on an aircraft can have a negative impact on its performance [4]. Some of the observed effects include: substantial decrease in lifting capability, frequent control-surface anomalies, increase in drag, and, in some cases, reduction in engine performance and stability [3,16]. Ground-based de-icing is both expensive and time consuming. In this method, a mixture of chemicals is heated and sprayed under pressure to remove ice on the aircraft. The toxicity of the deicing fluids is also an environmental concern[16,17]. The development of surfaces that can resist icing both on the ground and in flight is therefore a significant advantage for both commercial and military aircraft.

Ice accumulation can also reduce the performance of other lifting surfaces such as the blades of wind turbines by changing the aerodynamic profile of the blades and adding to the operational loading of the entire rotor, which can lead to significant energy loss and reduction of power production [18,19]. Current de-icing methods require the turbine to be stopped or use power from the turbine itself which decreases the efficiency of the system [20,21]. A number of strategies have been developed in the past to find suitable materials to delay or prevent ice formation [22-27], all with limited success.

Here, we turn our attention to nature and the anti-icing property of Antarctic penguins for inspiration in the development of novel and efficient ice-phobic surfaces. We also demonstrate that penguin ice-resisting ability is the product of a unique combination of surface chemistry, the physical structure of the penguin feathers, and a heat transfer mechanism directly related to

contact angle. Through a theoretical and experimental study of ice formation on the feathers of a series of different penguins, we show that cold-weather penguin feathers are more ice-resistant than those of warm-weather penguins due to differences in both the surface chemistry and fine structure of the feathers. The results are extended to superhydrophobic surfaces in general through the development of a heat-transfer model that explains the primary mechanism behind the delay of solidification on water-repellent materials. It should be noted that the main concern of this work is to prevent the initiation of freezing as when the trijunction starts solidifying, the drop adheres to the surface, and it becomes almost impossible for the drop to roll off of the surface under normal circumstances.

2.1.2. Penguins and Their Habitat

Penguins are a group of flightless, aquatic birds found on every continent in the Southern Hemisphere. Approximately 17 species occupy a variety of habitats and climates; some penguins live on thick sheets of ice most of the time due to the extremely cold weather. Others live on sandy beaches and small islands for instance, Magellanic and Humboldt penguins live in temperate zones near the equator while circumpolar species like the gentoo, Emperor and Adelie have adapted to the extreme cold in Antarctica.

Penguins are highly adapted to the marine environment and live on islands or remote areas of continents that have few or no land predators, as they cannot fly to escape. All of these habitats also provide access to nutrient-rich waters with an abundant supply of food.

In this study, five different types of penguins are used. Before going into the details of the experiments and analyses, it is important to learn about these different kinds of penguin and their habitat and distribution.

2.1.2.1. Adelie penguin:

This is a medium-sized penguin recognized by its white eye-ring. Feathers on the back of the head are slightly elongated and can be raised to form a small crest. Adélie penguins live on the Antarctic continent and on many small, surrounding coastal islands. They spend the winter offshore in the seas surrounding the Antarctic pack ice.

2.1.2.2. Emperor penguin:

The Emperor penguin is the tallest and heaviest of all living penguins. It is distinguished from smaller King penguins by its size, more robust structure, and a broad light yellow connection between yellow ear patches and the upper breast. Emperor penguins spend the long winter on the open ice and even breed during this harsh season. It breeds during Antarctic winter and exhibits many adaptations to the extreme cold.

2.1.2.3. Gentoo penguin:

Gentoo penguins are characterized by a white patch around and behind the eye that joins on the crown. These species populate the Antarctic Peninsula and numerous islands around the frozen continent. Gentoos are partial to ice-free areas, including coastal plains, sheltered valleys, and cliffs. Many adults remain around the colony throughout the year, whilst others take the opportunity during the winter months to make longer foraging trips further afield.

2.1.2.4. Macaroni penguin:

This is probably the most abundant of all penguins in terms of total numbers with an estimated world population of over 9 million breeding pairs. The head and upper-parts are black, and the under-parts are white; the eyes are red and the legs and feet are pink. The most distinctive features are the orange crests, which extend from the center of the forehead and sweep

backwards above the eyes. The distribution of Macaroni Penguin extends from the sub-Antarctic to the Antarctic Peninsula, but overall they are found further south than the rest of the crested penguins.

2.1.2.5. Humboldt penguin:

Humboldt penguins are medium-sized penguins; they have a black head with a white border that runs from behind the eye, around the black ear-coverts and chin, and joins at the throat. Endemic to the cold nutrient-rich waters of the Peru Current, the Humboldt Penguin breeds in a hot Mediterranean to desert climate. Comparing to the other types of penguins discussed above, Humboldt penguins are living warm weather environments.

2.1.3. Freezing Experiments on Penguin Feathers

In Figure 1, the equilibrium contact angles of water droplets on various penguin feathers are shown. The results are remarkable in that the feathers of penguins in colder environments always have higher contact angle with water than do warm-weather penguins. This observation suggests there might be a direct relationship between the contact angle and the penguins' habitat. Our hypothesis is that Antarctic penguins have evolved in part to improve their anti-icing properties, and to quantify and compare penguins ice-resisting abilities, we have performed a number of freezing experiments on different penguin feathers and measured the time of icing initiation.

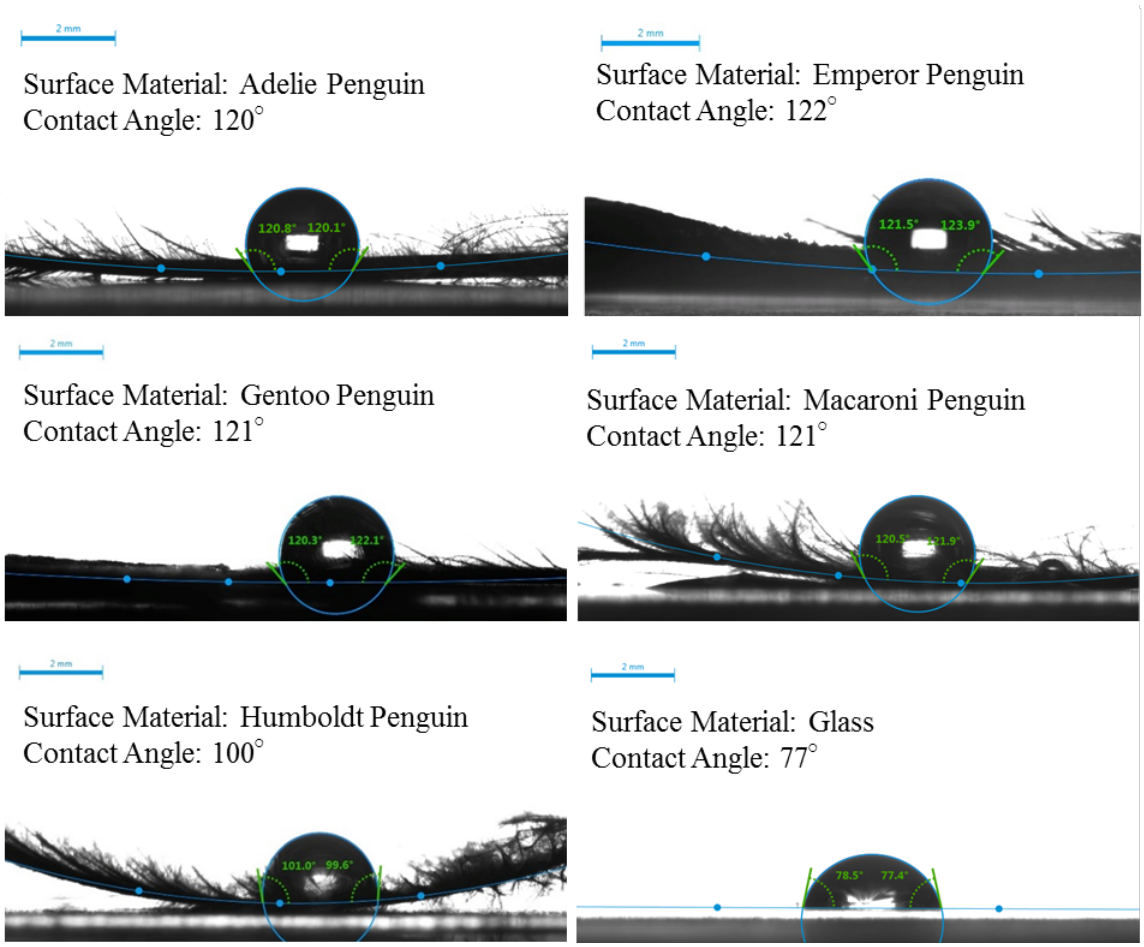

Figure 1. Static contact-angle measurements on penguin feathers. The contact-angles for water droplets on different penguin feathers and a glass substrate are measured using the ellipse fitting method [28]. The reported values on the figure are the roundup average contact angles, and the exact numbers are: Adelie 119.40 (± 1.58)°, Emperor 121.21 (± 1.23)°, Gentoo 120.27 (± 1.75)°, Macaroni 120.73 (± 2.21)°, and Humboldt 99.12 (± 4.11)°.

A series of images showing the freezing process on a cold-weather penguin feather (Adelie), a warm-weather penguin feather (Humboldt), and a clean, smooth glass substrate is presented in Figure 2a. In this experiment, the water drop at room temperature with the volume of $5\mu l$ is deposited on each surface at −20°C. On the glass substrate, the water drop begins to solidify roughly one second after the start of the experiment, resulting in a pointed frozen droplet shape at the end of freezing process consistent with the work of Anderson et al. [29]. Under the same conditions, when a water droplet is placed on a warm-weather Humboldt penguin feather, the

solidification process is delayed considerably. As shown in Figure 2a, the onset of solidification process on a Humboldt penguin feather is 30 seconds after the droplet deposition. Even more interesting, for a water droplet deposited on a cold-weather Adelie feather, the freezing does not begin until 57 seconds after droplet deposition as shown in Figure 2a. The result is roughly a fifty-fold increase in the solidification initiation time on an Adelie feather when compared to the glass substrate and a two-fold increase when compared to the Humboldt feather. The same set of experiments is carried out for several examples of warm-weather and cold-weather penguin feathers and the results are presented in Figure 2b. Depending on where a penguin resides, these results clearly show that the water-repellency and anti-icing characteristics of the penguin's feathers can be quite different. The change in wettability appears to make cold-weather penguin feathers better suited for forestalling ice formation and for keeping the penguins free of ice even in the harshest climates on earth.

It should be noted that although large contact angles appear to delay the solidification process, it is not the sole factor governing the ice formation. For instance, the feathers of Adelie penguins are less ice-resistant compared to other cold-weather penguins even though their contact angles are comparable.

a

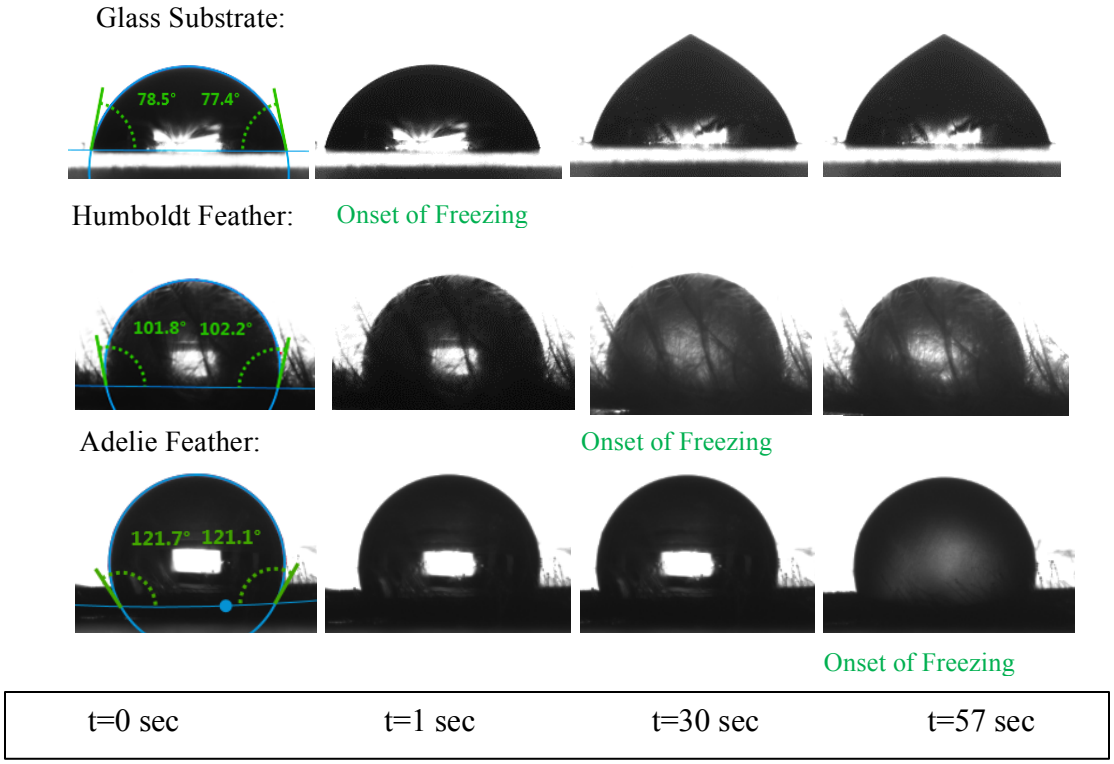

b

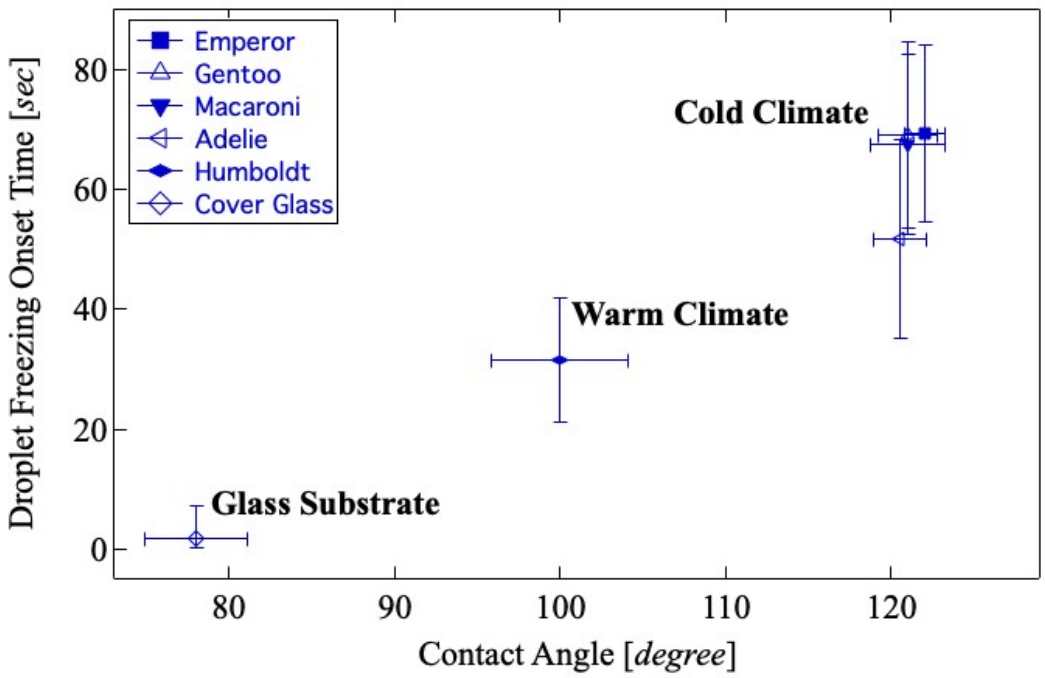

Figure 2. Freezing experiments on penguin feathers. a, Video sequence of water freezing on different substrates at −20℃. The droplets were deposited on the solid target with the flow rate of 2ml/min and total

volume of 5μl. The elapsed times are 0 s, 1s, 30s, and 57s, respectively. b, Time required for the onset of droplet freezing as a function of contact angle for a 5μl water drop on a series of penguin feathers in an environmental chamber cooled to T = -20C. There are significant differences between the freezing delay time of cold-weather penguins (Adelie, Emperor, Gentoo, and Macaroni) and the warm-weather one (Humboldt) (F(4, 60)=4.406, p= 0.00345). For comparison, the onset time of freezing for a droplet on a smooth glass substrate with a contact angle of 75 degrees was found to be close to one second.

2.1.4. Feather Structure Analyses

Feathers are the most prominent, complex and varied integumentary derivatives of birds. The basic plan of a penguin feather consists of a shaft with regularly spaced branches on either side. The branches, called barbs, form interconnected sheets or vanes which are the most visible part of a feather. A barb repeats most of this plan, having a central axis with tightly spaced barbules on either side. Although there have been many studies on morphology and structure of bird feathers [30-32], none of them has studied the nano-size pattern on penguin feathers that makes them excellent ice-repellent surfaces. To determine the important parameter making penguin feathers ice-phobic, it is essential to analyze the feather structure of penguins living in diverse environmental conditions.

Therefore, a series of SEM (Scanning Electron Microscopy) images of feathers of three different penguins were taken as shown in Figure 3. The SEM images in Figure 3a reveal the micron-scale features of the Emperor penguin feathers. In this figure, the barbs and barbules are clearly visible with the barbs roughly 20μm in diameter and spaced 300μm apart with a dense array of barbules less than 5μm in diameter protruding from the side of each barb. A further increase in the magnification shows the hooks branching from the barbules and the microstructure along the surface of the barbules creating a hierarchical structure enhancing the non-wetting properties of the feathers.

A closer look at the feathers is presented in Figure 3b. These images reveal an extremely fine structure along the surface of the shaft which appears to be a series of dimples and cavities. For the cold weather Gentoo penguin feather, the surface features are found to be in the range of 80-260 nm in diameter with average of 174 nm and population density of $4.02/\mu m^2$. The highly packed structure and complex nano-texture of the feathers provide the roughness necessary to trap air between and along the barbules, the barbs and the shaft making the feathers naturally hydrophobic [33].

However, for the warm weather penguin, Humboldt, these features are slightly different. The surface patterns are larger in size, smaller in depth, and more dispersed. The diameter of the surface features for Humboldt feather is between 350 to 600 nm with the average size of 462 nm and population density of $1.01/\mu m^2$. These features increase the surface hydrophobicity and increase the water droplet contact angle on Humboldt feather although slightly less than cold-weather feathers. It should be noted that this is the first time these nano-structures are observed on the penguin feathers. The work done by Wang et al [34] is the only previous study on icephobicity of penguin feathers and their potential to provide a passive anti-icing system. However, the only type of penguin studied was the Humboldt, the warm-weather penguin, and such nano-structures were not reported.

In addition to their surface structure, feathers have a unique surface chemistry. They are made of keratin which has a critical surface tension of ≈20 dyne/cm [35] and are covered by preen oil produced *via* the uropygial gland located at the base of the penguins tail [36]. Penguins cover the surface of their feathers with preen oil sometimes several times a day. The chemical composition of preen oil is primarily monoester waxes with fewer triglycerides and hydrocarbons [37]. To examine the preen oil composition and abundance on different penguin feathers in nature and

subject to the experiment, a complete Gas Chromatography/Mass Spectrometry (GC/MS) analysis is performed and the details are presented in Appendix 1. The GC/MS analysis reveals that both samples subject to the experiment and the control group, freshly collected feathers, have a similar profile, and the intensities of the components are in close proximity.

A comparison between preen oil composition of different penguins was also performed by Jacob [15], and it was shown that the chemical compositions of preen-oil vary with species. He studied the preen waxes of three species of penguins and showed that preen-oil compositions of penguins have two different wax patterns; the cold-weather penguins (Gentoo penguin and rock-hopper penguin) have the same pattern and it is mostly 3-methyl-branched acids; however, the warm-weather penguins (Magellanic penguin) has the second pattern in which 2- and 4-methyl-substituted fatty acids are dominant. It is believed that preen oil has many functions including protecting keratin, providing antibacterial properties, acting as an odorant, as well as improving the non-wetting properties of the feathers by reducing their surface energy and increasing their contact angle with water. Jacob's results show that depending on where penguins reside, the preen oil composition and consequently the water-repellency characteristics of these penguins are extremely different.

Therefore, the combination of the feather surface nano-structures as well as the preen oil compositions according to data obtained by Jacob[38], the water droplet contact angle and surface hydrophobicity defer depending on penguins' habitat, resulting in higher contact angle values for cold-weather penguins.

a

Emperor Feather:

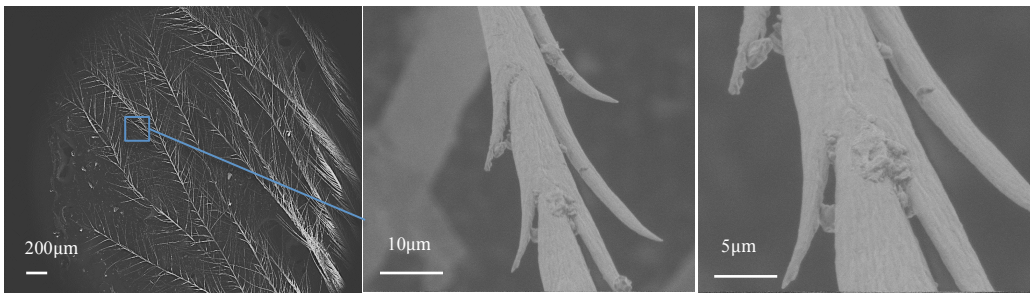

b

Gentoo Feather:

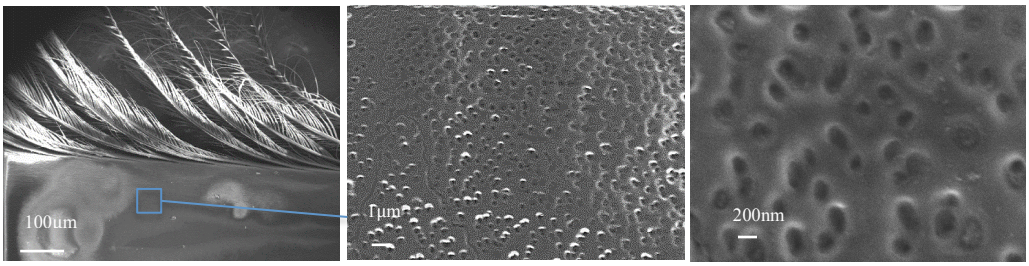

Humboldt Feather:

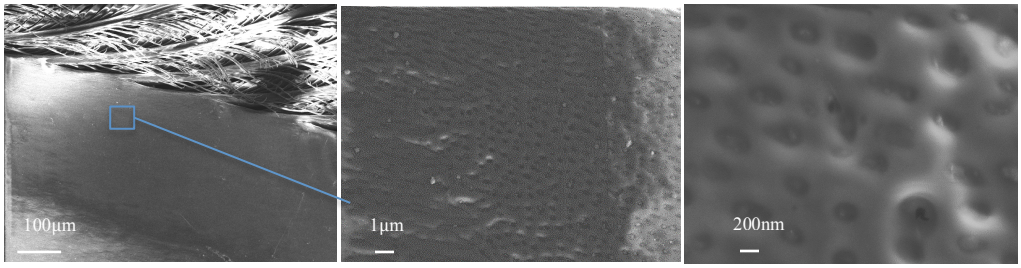

Figure 3. Feather structure analysis. a, The SEM pictures of the surface of the barbules of the Emperor penguin feather. The pictures show the hooks branching from the barbules and also the micro-texture along their surface. b, SEM images of feathers of the Gentoo and Humboldt feathers with three different magnifications to observe the submicron size air cavities on the shaft surface at three different magnifications increasing from left to right.

2.1.5. Theoretical modeling of heat transfer on superhydrophobic surfaces

The combination of the hierarchical structure of the feathers along with low critical surface tension of keratin and preen oil in these birds increases their contact-angle with water and

reduces their contact-angle hysteresis making the feathers hydrophobic [39,40]. A number of different theories have been proposed to explain the significant delay in the solidification time of water drops and the reduction of the adhesion strength of the incipient ice formation on hydrophobic and superhydrophobic surfaces [22,24,26,41-43]. Nonetheless, the underlying mechanism of the icephobicity of hydrophobic and superhydrophobic surfaces is still debated [23,42,44-49].

Quéré and his coworkers believe that on hydrophobic surfaces, a droplet sits on a composite surface of air and solid, and the presence of this insulating trapped air layer reduces the adhesion and delays the freezing process by slowing the rate of heat transfer [50]. Another study of icing behavior of superhydrophobic surfaces has been done by Alizadeh et al. [51]. They showed that the icing delay on superhydrophobic surfaces could be due to the lower probability of heterogeneous nucleation and the reduction of water-solid interfacial area. Although some of these factors are likely to be effective, the dominant physical mechanism that governs the anti-icing properties of hydrophobic and superhydrophobic surfaces in general and penguin feathers in particular is subject to controversy.

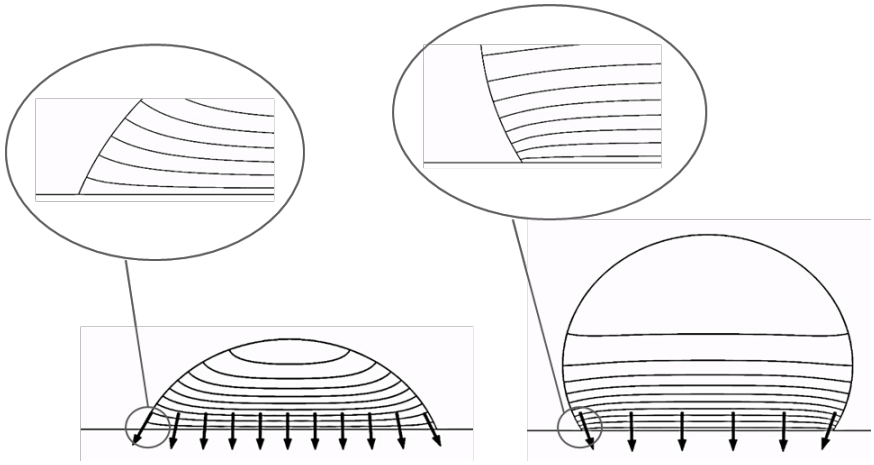

Figure 4. Isotherms propagation inside droplets on hydrophilic and hydrophobic surfaces. Schematic diagram of isothermal lines on droplets of contact angle smaller (left) and larger (right) than 90 degrees.

Based on our experimental results, we believe that there is a strong correlation between the start of freezing and contact angle. Our hypothesis is that, for droplets on penguin feathers and other high contact angle surfaces, there is a further delay in solidification resulting from a geometrical constraint on the heat flow. In other words, as the contact angle of the droplet increases above 90 degrees, the curvature and shape of the isotherms change (See Figure 4) confining the conduction heat flow to a smaller surface.

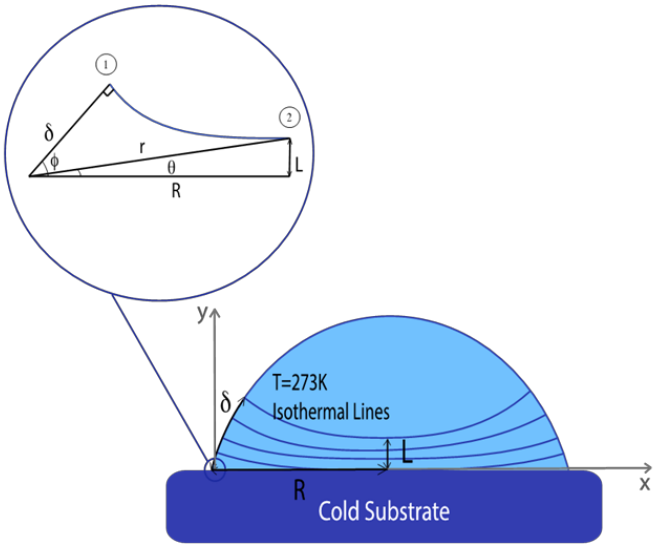

Figure 5. Geometrical parameters near the contact-line. Growth of isotherms on a droplet placed on cold solid surface.

To test our hypothesis, an approximate theoretical heat-transfer model was developed. In our model, the water droplet with initial temperature of T_0 was approximated as a spherical cap with radius R and contact-angle φ as appeared in Figure 5. The change in surface temperature, T_w, and convective heat losses to the air were assumed to be negligible. To obtain the solidification rate, the observable growth of the isotherms at the liquid-air interface, δ, was calculated. In the vicinity of the contact line, the quasi-steady two-dimensional heat transfer equation in a wedge [52] was solved to determine the temperature field and surface heat flux near the contact-line. The rationale is that the diffusion time scale near the contact line is much shorter than the solidification time scale $(\delta^2/\alpha t_0 \ll 1)$; hence, a quasi-steady assumption. Under these conditions, the heat transfer equation simplifies to the Laplace's equation:

$$\nabla^2 T = 0 \qquad (1)$$

The local general solution of equation (1) in polar coordinates was found as follows [53]:

$$T(r,\theta) = r^{\tau}[A cos\tau\theta + B sin\tau\theta] + C\theta + D \qquad (2)$$

where τ, A, B, C, and D are constants.

The temperature at the wall was fixed ($\theta = 0, T = T_w$) and the air/liquid interface was assumed to be a perfect insulator (i.e. heat loss at the edge is negligible, $\theta = \varphi, \partial T/\partial\theta = 0$). Therefore, the resulting temperature profile within the drop becomes:

$$T(r,\theta) = T_w + Br^{\tau}sin\tau\theta \qquad \tau = \frac{(m+1/2)\pi}{\varphi} \qquad m = 0,1,2,\ldots \tag{3}$$

Equation (3) is the solution for the steady heat transfer in a wedge. However, we need to obtain the time-dependent temperature profile to determine whether or not solidification is delayed. Because of the symmetry, it is reasonable to assume that at the centerline, the solidification process is not affected by the presence of a contact-line. Thus, the heat flux and temperature gradient on the centerline were obtained using the unsteady one-dimensional heat conduction equation (i.e. the centerline acts as a part of a semi-infinite body). As shown in Figure 5, points (1) and (2) lie on the same isotherm, i.e. $T_1 = T_2$. As a result,

$$T_w + Br_1^{\tau}sin\tau\theta_1 = T_w + Br_2^{\tau}sin\tau\theta_2 \tag{4}$$

Considering the polar coordinates of points (1) and (2), ($r_1 = \delta, \theta_1 = \varphi$) and ($r_2 = r, \theta_2 = \theta$), equation (4) can be rewritten:

$$\delta^{\tau}sin\tau\varphi = r^{\tau}sin\tau\theta \tag{5}$$

The heat conduction equation for a semi-infinite body indicates that the thermal penetration depth is proportional to $\sqrt{\alpha t}$, where α is the thermal diffusivity. Based on the geometry presented in Figure 5, $r = \sqrt{L^2 + R^2}$, where $L \approx \sqrt{\alpha t}$ and R is the contact radius of the droplet. Using non-dimensional time- and length-scale ($\eta = \alpha t/R^2$ and δ/R respectively), the dimensionless growth of solidification front was obtained as a function of time and contact angle:

$$\frac{\delta}{R} = \sqrt{\eta + 1}\left(sin\frac{(m+1/2)\pi\tan^{-1}\sqrt{\eta}}{\varphi}\right)^{\frac{\varphi}{(m+1/2)\pi}} \tag{6}$$

In Figure 6, the variances of the location, δ, of an isotherm (e.g. freezing temperature) for different contact angles at any time, η, is shown. Here $\delta = 0$ corresponds to the location of the freezing isotherm at the contact-line. It is clear that at a given time, the isotherm at the liquid-air interface travels shorter distances for the larger contact angles. This observation implies a delay in the onset of solidification for droplets on surfaces with large contact angles. The dashed line on Figure 6 shows $\delta/R = 0.2$ which is an arbitrary value in our calculation assuming to be the location where the freezing front becomes observable. The three contact angle values in Figure 6 (70º, 100º, and 120º) correspond to the contact angle of water droplet on glass, Humboldt feather, and Adelie feather respectively in order to link our theoretical results to the experiments.

Comparison of the time delay in the freezing onset using the values obtained from the theoretical model (Figure 6) and the experimental data (Figure 2) shows good agreement between the model and experiment. The time delay in the onset of solidification for cold weather penguin feathers is 2.47× more than the warm weather penguin feather based on the analytical model, and from the experimental data, the ratio of average delay time for cold weather penguin feather to warm weather penguin feather is 2.11.

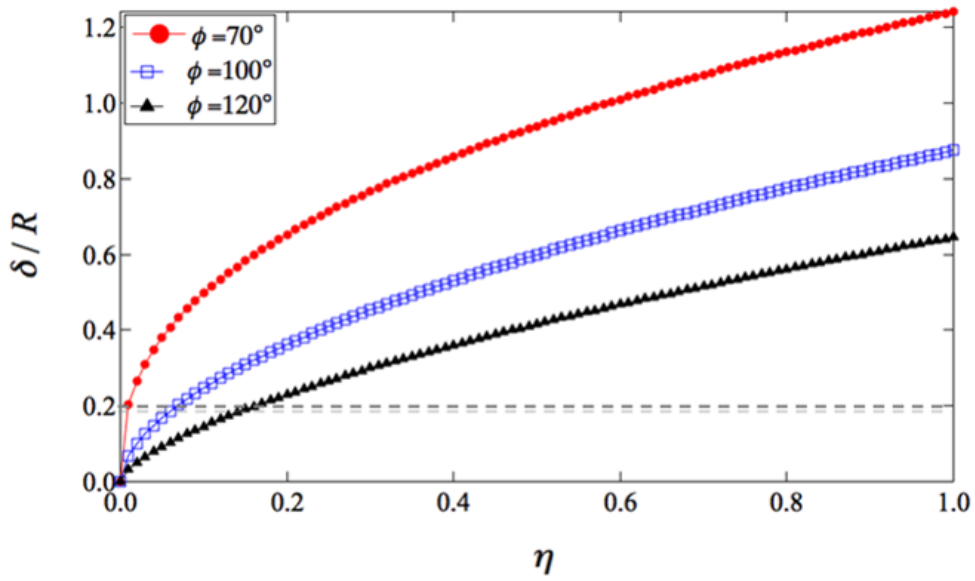

Figure 6. Theoretical modeling of heat transfer through the droplet of different contact angle. Progression of solidified layer at the edge of the droplet versus time for surfaces of different contact angle from hydrophilic to superhydrophobic. $\delta = 0$ corresponds to the surface of the substrate. At a constant time, the solidified layer ascended less along the drop's liquid-gas interface for drops of higher contact angle.

2.1.6. Numerical simulation of freezing front propagation for static droplets

A set of numerical simulations was carried out with COMSOL Multiphysics to obtain the determining factors in the time delay of freezing onset and to corroborate our experimental and analytical studies. In these simulations, three different water drops with initial temperature of 300K were placed on a glass substrate at an initial temperature of 250K. Temperature profiles one second after droplet deposition are presented in Figure 7. Droplet A had the same contact area with the solid surface as droplet B but the contact angle was smaller than 90°. As shown in Figure 7, the ice front advances less into the droplet with a larger contact angle; therefore, the rate of heat transfer was lower and the eventual solidification was delayed. However, the simulations for droplets B and C, which have the same contact angles but different contact areas with the solid surface, showed that the propagation of isotherms was nearly the same for these droplets. This result was consistent with our theoretical analyses suggesting the delay in

solidification was mostly due to a geometrical constraint in the heat flow caused by the increase in contact angle.

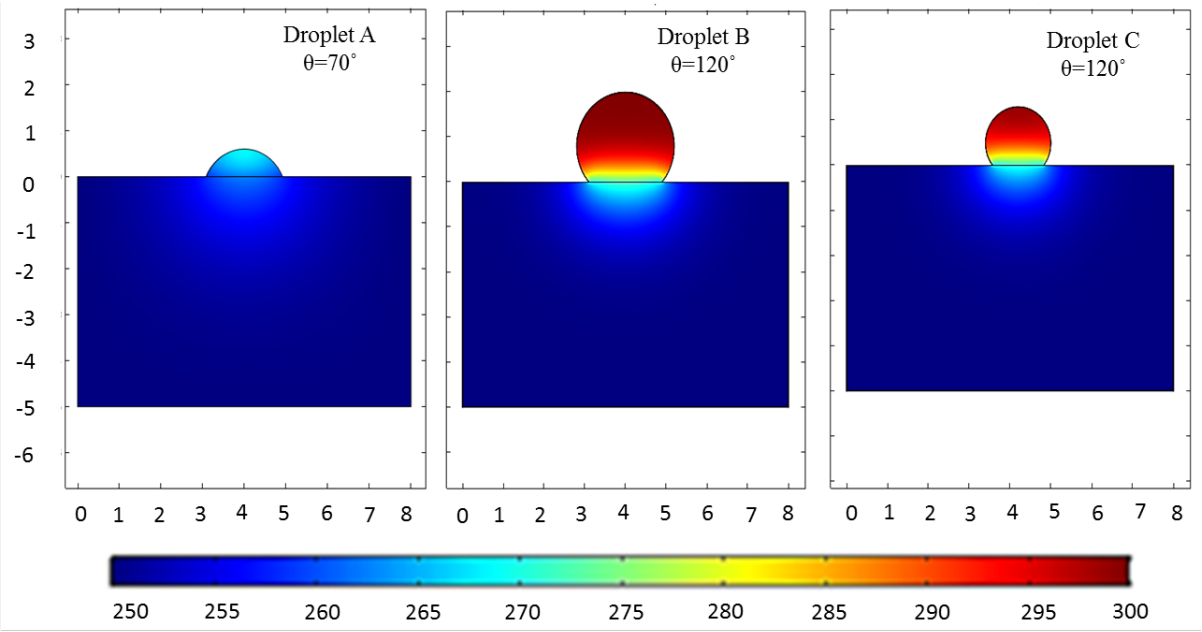

Figure 7. Heat-transfer simulations for water droplets at $300K$ for drops with different contact angles and contact areas on a surface with temperature at $250K$ at t=1 *sec*. Droplets A and B have the same contact area with substrate but different contact angles, and droplet C has the same contact angle as the droplet B but a smaller contact area. The spatial scales are in millimeters.

It should be noted that there is a disparity between the reported time of initiation of freezing from the experiments and the values predicted from the theoretical modeling mainly due to the use of constant temperature boundary condition to solve the energy equation. To understand the effect of varying temperature of the substrate, we have plotted the temperature of the liquid near the triple contact-line for droplets A, B, and C with respect to time in Figure 8a using the simulation results. For droplet A, the temperature of the liquid near the substrate decreased almost immediately by nearly 20K and reached the freezing condition in less than 1 second (freezing condition showed by the dashed line in Figure 8a); however, for droplets B and C, the trijunction temperature decreased to 290K, and it took ≈20 seconds for the substrate to cool down to a sub-

freezing temperature which is 20 times longer than the droplet A. These results are consistent with our theoretical analyses predicting a 17-fold increase in the onset of freezing for droplet on cold-weather penguin feather compared to glass substrate. As a side note, experiments showed that water does not freeze exactly at 273K, and freezing usually happened at sub-freezing temperatures. In our simulations, we assumed that freezing happens 10 degrees below the freezing point (~263K). The same set of simulations were performed (Figure 8b) for droplet of volume of 5μl on a surface with the measured contact angles of cold and warm-weather penguins, see Figure 1, to show the effect of contact angle on the solidification delay. The results showed a 2.5× delay in the start of freezing on cold-weather penguin feather (θ=120º) compared to warm-weather penguin feather (θ=100º), which is in excellent agreement with our theoretical (2.47×) and experimental (2.11×) data.

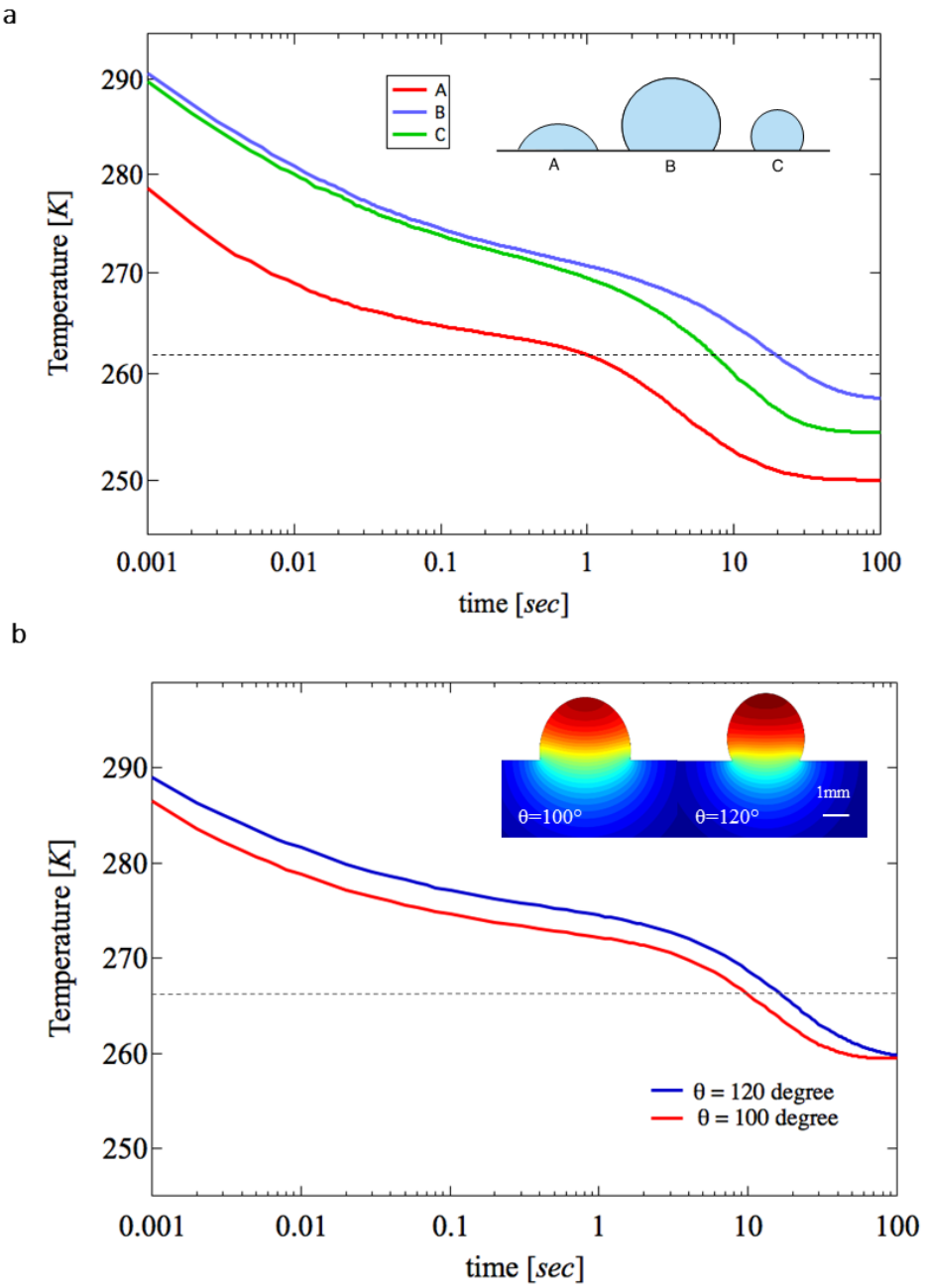

Figure 8. Temperature at the trijunction. a, Temperature variation with time at the trijunction for three water droplets at $300K$ with different contact angles and contact areas on a surface with temperature at $250K$. The contact angle with the surface for these three droplets, starting from the left, are 70˚, 120˚, and 120˚ respectively. b, Change in contact-line temperature with time for a droplet on warm-weather penguin $\theta = 100°$ and cold-weather penguin $\theta = 120°$. Dashed line shows the onset of freezing at triple contact-line.

As a result of these simulations, the ice front advanced less into the droplet of larger contact angle; therefore, the rate of heat transfer is lower and the eventual solidification is delayed. It is also shown that the propagation of isotherms is nearly the same for droplets of same contact angle but different contact area with solid. Thus, for droplets of the same contact angle, regardless of the volume or contact area with the substrate, the rate of heat transfer and growth of isotherms are approximately the same. It should be noted that the simulation results agree with our early assumption that convection to the air was negligible compared to conduction from the solid into the droplet.

2.1.7. Other Governing Factors in Incipient Freezing Delay:

Aside from the geometrical effect due to increase in contact angle, the time delay in the start of freezing happens as a result of different factors including the ice nucleation delay time and the presence of an insulating layer in between the droplet and the substrate due to the entrapment of air in surface cavities as discussed in the literature.

We believe that the most dominant factor, not the sole factor, that delays the onset of freezing is due to the change in the profile of isotherms inside the droplet caused by increase in contact angle. To support this claim, we have calculated and compared the delay caused by other factors such as nucleation energy barrier and insulating air layer to the geometrical heat barrier.

Based on classical nucleation theory, the free energy barrier ΔG for heterogeneous nucleation for a supercooled droplet on a surface depends on the temperature of the droplet, the ice-water contact angle, and surface roughness. Surface roughness can affect the ice nucleation only if the roughness curvature is close to the critical nucleus radius, which is not the case for penguin feathers ($(R/r_c \approx 60) \gg 10$). To predict the onset of freezing, we are concerned about the ice

nuclei formed on the substrate; therefore, for a droplet on a cold- and warm-weather penguin feather, the mean ice-water contact angles are 120° and 100° at Ts=−20°C respectively. Using the measured values of contact angle, the ratio of free energy barrier for cold and warm weather penguin feathers ($\Delta G_{Het,Cold}/\Delta G_{Het,Warm}$) is 0.84/0.63 leading to 1.33-fold increase in nucleation energy barrier and 0.81-fold decrease in the rate of formation of ice nuclei; in other words, it takes 1.23-fold more time for one nucleus to form on the cold weather penguin feather compared to the warm weather penguin feather at the nucleation temperature. This is based on the assumption that the droplet (or at least liquid close to the substrate) has reached the nucleation temperature; however, since the droplet and feathers have different temperatures (corresponding to water and air temperature in Antarctica), there is a time delay in reaching the nucleation temperature, and based on our theoretical model, that temperature diffusion time delay strongly depends on contact angle, and the geometrical delay in temperature diffusion time caused by increase in contact angle for cold weather penguin feathers is 2.47-fold more than the warm weather penguin feather based on the model. This value is not only in good agreement with the experimental data (ratio of average delay time for cold weather penguin feather to warm weather penguin feather is 2.11) but also the most dominant of all other factors.

In the case of the air layer beneath the droplet, it is important to know that the average diameter of the air cavities for penguin feathers is about 100 nanometers and they are only 50-100 nm in depth. As the air layer thickness is very small, the time delay by insulating air layer is in the order of microseconds.

2.1.8. Discussion and conclusion

This chapter was inspired by the examination of penguins in their natural habitat and the realization that penguins have the ability to completely prevent macroscopic ice formation on their feathers. Our investigations reveal that the anti-icing properties of penguin feathers are in large part due to the micro- and nano-porous surface texture of their feathers and the low critical surface tension of the preen oil covering them make penguin feathers hydrophobic a property that is necessary but not sufficient. The freezing of the drops must be slow enough that drops cannot adhere to the feathers before rolling off.

An experimental and theoretical study was conducted to understand the solidification delay on both cold and warm-weather penguin feathers and the results were extrapolated to superhydrophobic surfaces in general. The results of experiments showed that transition from instantaneous freezing and large footprints to delayed solidification and less ice adhesion was possible using penguin feathers with cold water feathers delaying ice formation by approximately fifty times compared to a smooth surface and two times compared to a less hydrophobic, warm-weather penguin feathers. The freezing times were found to directly correlate to the static contact angle of the feather.

Inspired by this observation, a theoretical model was developed to explain the heat transfer delay with increasing in contact angle on any generic water repellent surfaces, penguin feather or man-made superhydrophobic surface. Our theoretical analysis and numerical simulation results confirm that, for higher-contact-angle droplets, the inception of freezing was delayed. There are, however, other factors that can contribute to the icephobicity of a surface including the insulting air layer beneath the droplet and the scarcity of nucleation sites on the surface amongst others, which their effects are less substantial compared to the geometric delay. The effect of these

additional mechanisms was not included in this model, and the evaluation of their impact remains to be fully studied.

2.2. Delay of Ice Formation on Plant Leaves

The following section is a continuation of the icephobicity study in nature. This chapter was inspired by nature and ice-resistivity and superhydrophobicity of plants leaves. Kale is a winter plant with superhydrophobic behaviors, which is normally known as an advantage for cleaning the leaves; however, this work reveals that the kale leaves have a special surface microstructure that delays the ice formation process making it a good candidate for designing an ice-repellent coating. The organization of this section is quite similar to the ice formation study on penguin feathers. In-depth experimental analyses, IR thermography, contact angle measurements, and scanning electron microscopy (SEM) of the leaves were performed to discover how different plants can prevent icing in search of an optimal design for an artificial ice-repellent coating.

2.2.1. Introduction

Some plant leaves have the ability to avoid and tolerate freezing, as it is crucial to their existence. Intracellular freezing is well known to damage the plant cell partitioning and disrupt the metabolic activity of the membrane [54]; therefore, winter plants have developed mechanisms to prevent ice formation and moderate its effect. Their anti-icing techniques under realistic conditions are not yet fully understood. Here, the three icing quantifications for two different types of plant leaves (Kale and Lettuce leaves) are measured and compared, and the process of heat transfer and ice propagation is monitored using high speed IR thermography.

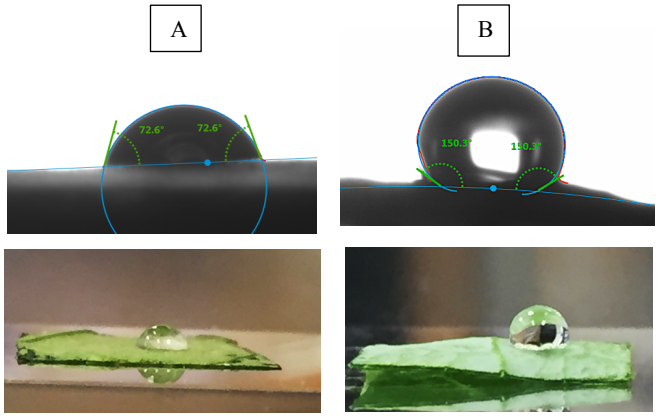

Figure 9. Optical images of the freezing experiments on Lettuce and Kale leaves. Images are processed to measure the contact angle of water droplet on the plants leaves. The average static contact angles of water droplet on the (A) Lettuce and (B) Kale leaves at −10°C are 74.28° and 147.16° respectively.

2.2.2. Results and Discussion

The contact angle measurements are performed at temperature −10°C (Fig. 9). Kale leaves show superhydrophobic behavior with average contact angle 147.16±2.53 degrees (95% Confidence Interval) while the lettuce leaves have relatively small contact angle 74.28±4.98 degress (95% Confidence Interval). The increase in contact angle is shown to delay the formation of ice by changing the profile of isotherms and confining the heat flow to a smaller surface that reduces the rate of heat transfer and increases the time of onset of solidification in which ideally the drop would run off the surface before solidifying [55]. The study of ice formation on penguin feather shows that there is a strong dependence between the freezing incipient or in general the rate of heat transfer and the contact angle of the droplet on the surface. The proliferation of the solidification front is calculated analytically at any time by solving the heat transfer equation near the contact-line. The equation (6) shows the observable growth of isotherms at the triple contact-line, δ, as a function of time of freezing, t, and contact angle, φ.

The predicted growth of freezing isotherms are plotted in Figure 10 using the contact angles of the Kale and Lettuce implemented into equation (6), and it shows that δ is smaller and its growth is slower for a droplet on Kale leaf compared to the Lettuce leaf. Furthermore, at high contact angles, the adhesion strength is lower [56-58] and drop can easily roll off of the surface maintaining a drop-free and ice-free surface at all times.

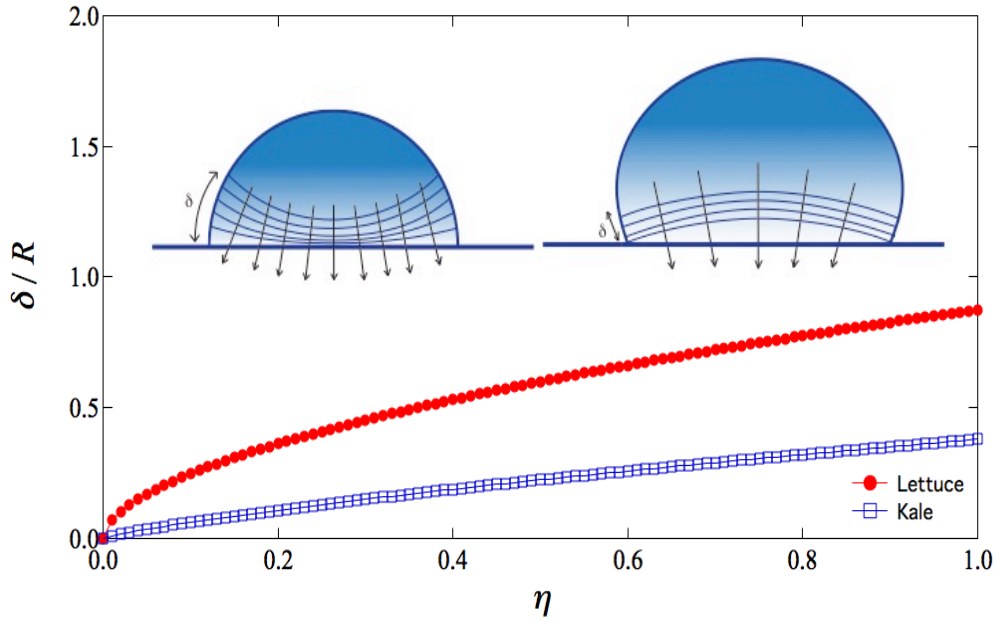

Figure 10. Growth of freezing front for a droplet on Kale and Lettuce leaves versus time. For droplet on the Kale leaf with higher contact angle, the growth of freezing front is gradual compared to Lettuce leaf.

The second factor in quantifying the icing delay is the average time of onset of solidification, i.e. the average time between the drops deposition on the substrate and the start of freezing. The droplet behavior on the leaf surface during freezing as time elapsed is shown in Figure 11 for both plants. For a water droplet on a Lettuce leaf (top row), droplet starts solidifying at $t=3.63\pm1.02$ *sec* after deposition on the leaf surface at −10ºC. Solidification begins after *83.78±18.50* seconds when same size droplet is placed on a Kale leaf surface (bottom row). These results indicate that Kale leaves have the ability to significantly delay the onset of freezing process compared to the Lettuce leaves.

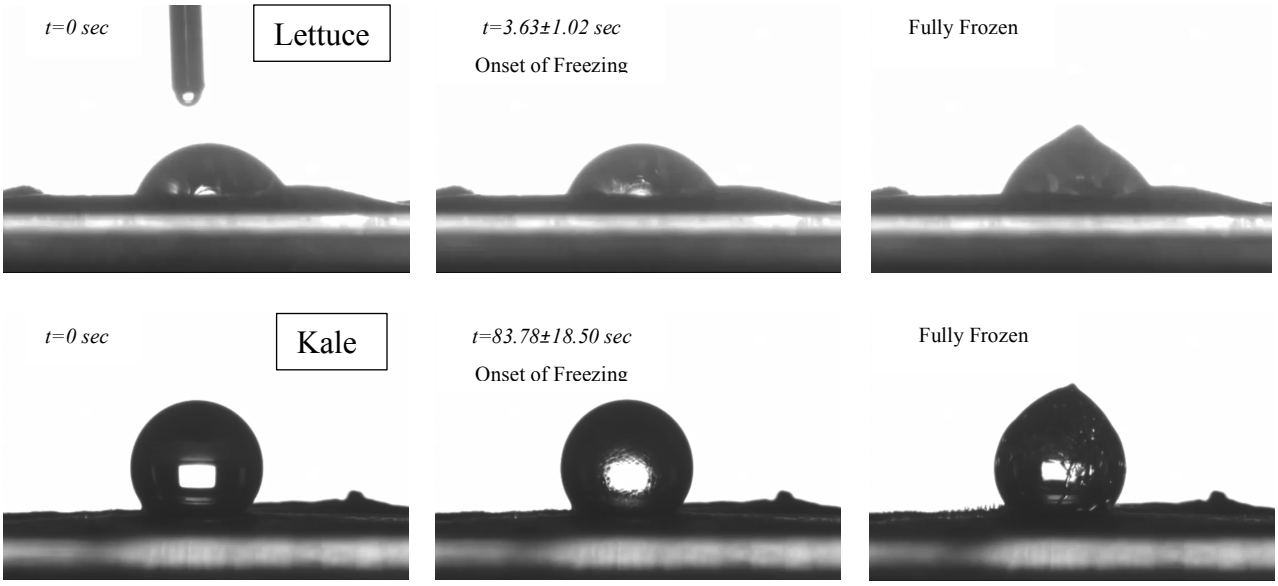

Figure 11. The video frames of the freezing process of the water droplet at room temperature on the Lettuce and Kale leaves at −10ºC.

The heat transfer process of a single droplet deposited on both plant leaves is studied using a high-speed IR thermography camera to further measure the rate of thermal transfer and temperature distribution through the leaves. Figure 12 shows the video sequence of the heat transfer from the water droplet into the leaves for both plants. The temperature of the surface of the leaf is 20ºC and water droplet initial temperature is 70ºC. The purpose of these experiments is to observe the typical rate of heat transfer from the drop to the surface of the leaves without having to consider the complexity of the freezing and phase change process.

As shown in Figure 12, droplet instantly forms a semi-spherical cap with large contact angles when deposited on the Kale leaf; however, droplet spreads widely over the Lettuce leaf surface as at room temperature the contact angle of water on the Lettuce leaf is ≈55° and gets absorbed into the surface for the most parts. To evaluate the average heat transfer rate on leaves surfaces, the non-dimensional area average temperature of the drop versus time is also plotted in Figure 12. In the case of the Lettuce leaf, the temperature of the droplet drops very quickly as it is

deposited on the surface, and there is an abrupt change in the temporal profile. However, for the Kale leaf, the change in temperature happens over longer times, and the rate of heat transfer is much slower compared to the Lettuce leaf at all times. These results show that Kale leaves have the ability to slow down the heat transfer process which causes a considerable delay in initial freezing process, and they have a high contact angle with water which makes them a perfect candidate for a hydrophobic coating to resist icing.

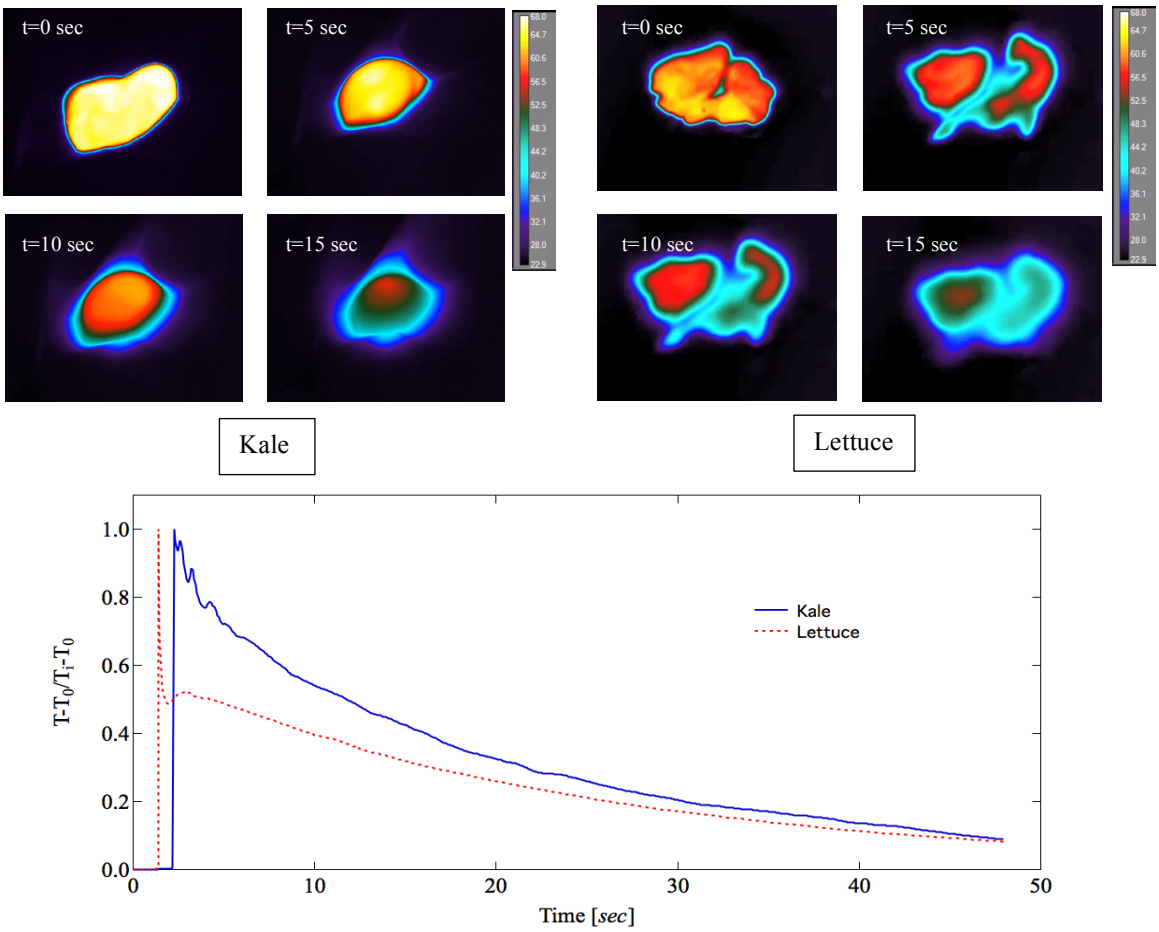

Figure 12. The IR camera images of the heat transfer process for a droplet on the Kale and Lettuce leaves. The plot at the bottom shows the time rate of change of non-dimensional temperature of the droplet on both leaves. Here, T_0 and T_i refer to temperature of the substrate (20 ºC) and initial temperature of the drop (70 ºC) respectively.

Finally, the effect of nucleation thermodynamics is another factor that needs to be considered when designing an ice-resistant coating. For a supercooled water droplet on Kale and Lettuce leaves, the nucleation energy barrier depends on contact angle, surface roughness, and temperature [59]. Under the same environmental conditions, the delay in the formation of critically sized ice nuclei is determined by surface roughness radius of curvature and contact angle. In the framework of classical nucleation theory, the nucleation activation energy is not contingent upon the surface roughness for values ten times greater than the ice nucleus critical radius, $r_c \approx 4$ nm at

−10°C; therefore, in the case of both Kale and Lettuce leaves, using the surface roughness calculated based on the scanning electron microscopy (SEM) images of the leaves, the effect of surface roughness on icing delay is insignificant. The SEM images of the leaves on Lettuce and Kale are shown in Figure 13. The column on the left shows the SEM image of the shaft of the leaves. For both Kale and Lettuce, the shaft microstructure appears to be analogous; on the contrary, for the surface of the leaf (right column), the structures are quite different as for the Lettuce leaf, the structural units on the surface are larger compared to Kale and they are porous. Therefore, as soon as the water droplet sits on the Lettuce leaf surface, it spreads over the leaf, wets the surface quickly, and gets absorbed into it. Nonetheless, in the case of Kale leaf, the texture of the leaf is more condensed, and water droplet on the Kale leaf has a larger contact angle with a smaller contact area.

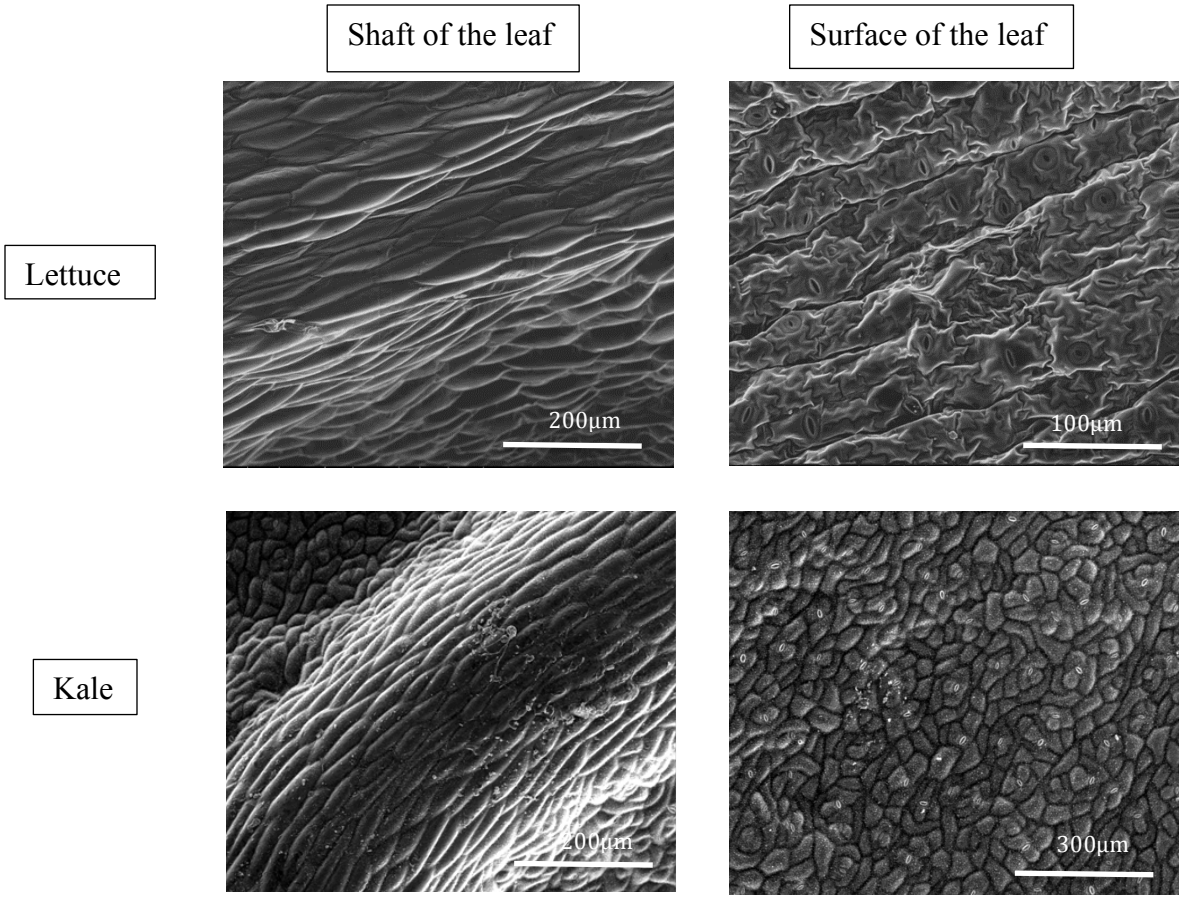

Figure 13. The SEM images of the surface and shaft of the Lettuce and Kale leaves. The microstructure on the surface of the leaves seems to be different, while the shafts have the similar patterns.

The rate of formation of ice nuclei on the leaves, therefore, depends on the contact angle of water droplet on these surfaces. The nucleation rate equation (7) can be written as:

$$J = C_1 \, exp\,(-C_2(2 - 3cos\varphi + cos\varphi^3) \qquad (7)$$

where C_1 and C_2 are constant. The nucleation rate is ≈15 times smaller for a water droplet on Kale leaf compared to Lettuce leaf, which indicates that the average freezing delay time is ≈15 times higher for superhydrophobic Kale leaf (the measured delay time ratio via experiments is ≈23).

In conclusion, a comprehensive experimental study was performed to study icephobicity on various plant leaves. The results of icing experiments and IR thermography on Kale and Lettuce

leaves revealed that the start of freezing is delayed considerably for a water droplet on the Kale leaf compared to Lettuce, and the anti-icing properties of the winter plant, Kale, were shown to be largely due to the surface microstructure, low nucleation rate, and large contact angle. The surface morphologies were also investigated so as to find a rational design for an icephobic coating. Thus, there exists a possibility to design a coating that can resist icing even in the extreme cold by increasing the hydrophobicity of the surface of the exposed structures, which is of a wide range of applications.

2.2.3. Methods and Materials

We conducted ice formation experiments on two types of plants; 1) Kale (Brassica oleracea var. sabellica) which can be harvested in winter, has the ability to survive temperatures as low as −10ºC, and more interestingly shows superhydrophobic behaviors [60-62], and (2) Lettuce (Lactuca sativa) that grows best in Spring and Fall with air temperature around 15 ºC and cannot tolerate temperatures lower than 10ºC [63-65].

A drop shape analyzer (KRÜSS, DSA 100) equipped with a temperature controlled environmental chamber and a Peltier plate that accurately measures the contact angle, time of onset of freezing, and drop base diameter was used for freezing experiments on the plants leaves. The environmental chamber is capable of reaching temperature of -30°C in a controlled humidity environment. The temperature of the substrate is set and controlled by the Peltier elements and temperature controller unit inside the DSA. De-ionized water was used for the experiments. Using de-ionized water minimizes the concentration of minerals (i.e. calcium) that may affect the ice formation initiation and nucleation sites. Commercially available plants were chosen for these experiments. Sample surface area of 2x2 in^2 cut were selectively made from each plant and

placed on a substrate. Substrate was gradually cooled down to −10ºC and stabilized for 5 minutes. A 5µL volume droplet at room temperature was deposited on the leaf surface. Optical images were obtained from the ice formation process, and the freezing initiation was detected visually by using high-speed camera (100fps). The experimental setup is shown in Figure 14.

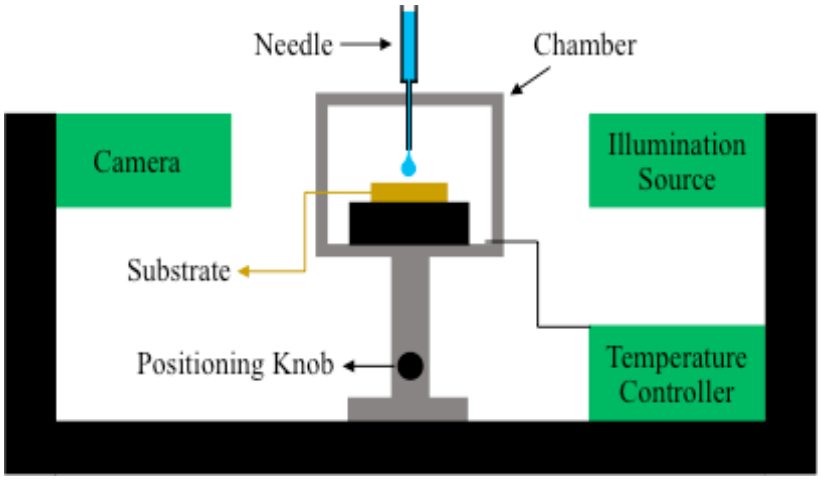

Figure 14. Schematic of the experimental setup on a drop shape analyzer (KRÜSS, DSA 100) equipped with a temperature controlled environmental chamber and a Peltier plate to set and monitor the temperature.

The freezing experiments are performed on the plant leaves to observe the rate at which water droplet freezes on the leaves and assess their ability to delay the ice formation process. The experiments were repeated 20 times for each sample. For each set of experiment, the geometry of the droplet is measured from the images to determine the contact radius and contact angle while tracking the propagation of the freezing front. In addition, to study the rate of heat transfer from the surface of different plant leaves and measure the temperature of the drop as a function of time, a high speed infrared temperature probe (FLIR, A6753 high speed IR camera) is used. The FLIR camera offers high-resolution imaging and short exposure times which allows monitoring and acquiring data with extreme accuracy.

3. Experimental and Theoretical Investigation of Impinging Drop Solidification

This chapter mainly focuses on determining the important physical parameters involved in the non-isothermal spreading of droplets as well as controlling the post-solidification geometry of impinging droplets with moderate impact velocities where spreading is driven by impact velocities, but fingerings or instabilities do not occur at the contact-line. A set of analytical modeling with possible explanation for contact-line arrest is done that shows the final radius of droplet of moderate impact velocity is independent of the initial conditions including the impact dynamics and temperature gradients. The experimental data also verify the accuracy of the theoretical results.

3.1.1. Introduction

Understanding the physics behind the non-isothermal spreading of droplet is of utmost importance due to its broad applications in diverse areas of industry such as 3D printing. 3D printing technology has been around since the 1980s. This technology has the ability to create complex parts via different deposition techniques. To fabricate mechanically robust and stable structures using 3D printing with material properties well suited to the application, all-around control of droplet size, solidification rate, temperature gradient in substrate and droplet, adhesion between the layers, and droplet impact velocity and direction is required. The complexity of the physics of 3D printing emerges from the intertwined effect of droplet impact dynamics and solidification. To enhance the resolution and integrity of the printed parts, it is essential to have a thorough understanding of the physical phenomena involved so as to determine and control the maximum spread factor, $\varepsilon = R_{max}/R_0$ where R_0 is the pre-impact droplet radius and the

engaged physical properties such as surface tension, σ, viscosity, μ, fluid density, ρ, thermal conductivity, k, and etc.[66-73].

3.1.2. Literature Review

Despite the wide range of experimental and numerical studies performed in this field, the physics of non-isothermal spreading and solidification arrest are still unknown. Most of the work done in this field is based on solving the energy conservation equation between the pre-impact kinetics and interfacial energies and the final energy loss to viscous dissipation and surface deformation[74]. For example, one of the first analytical studies considering coupled fluid spreading and solidification of impinging metal droplets has been done by Madejski[75]. In his attempt to find the maximum spread factor, he used the axisymmetric two-dimensional radial flow model with solidification emerging from the centerline and assumed that droplet forms a cylinder of radius R enlarging with time. His analytical model was based on the balance of the initial kinetic energy of the droplet and change in surface energy due to droplet deformation and work done in overcoming liquid viscosity during impact. In his calculations, he failed to include the effect of undercooling, surface wetting, and advancing contact angle, all of which lead to significant discrepancies between his theoretical model and experiments. Collings et al[76] also studied the impact dynamics and solidification of liquid droplets analytically. One modification that they implemented in their analysis was considering the effect of contact angle. However, they made the unfitting assumptions that viscous dissipation and initial surface energy are negligible and the advancing and equilibrium contact angles are inseparable, so as a result, the obtained values from their analytical modeling did not match the experiments.

Watanabe et al.[77] employed a simple numerical simulation method neglecting the effect of viscous dissipation to predict the maximum droplet deformation and solidification progress on a cold target. They considered the fluid dynamics and phase change process to be uncoupled and happen independently. In other words, they assumed that solidification occurs after the droplet deformation is complete regardless of the impact conditions and the temperature gradients. Pasandideh-Fard et al.[78] studied the impact of droplet on solid surface both experimentally and numerically. Measured values of dynamic contact angle from experiment were used as boundary conditions for the numerical model. In order to find the effect of droplet solidification on the maximum spread diameter, they assumed that all kinetic energy stored in the solidified layer is lost.

The scope of the experimental work done on the evolution of the drop base diameter upon simultaneous spreading and solidification is quite limited. Most of the previous researches are focused on bouncing and splashing effects of liquid droplets[79-82], and others remain limited to isothermal spreading[83,84] which is fundamentally different from the solidifying dynamic contact-line problem as solidification plays a crucial role in controlling the molten contact line arrest. Schiaffino and Sonin[2,85] performed an experimental study of the behavior of a deforming contact-line as the flow spreads and solidifies on a sub-cooled target. They realized that prior to arrest, the relationship between the dynamic contact angle and contact-line speed appears to obey the Tanner-Hoffman law[86,87] assuming the equilibrium contact angle is zero. However, their study was limited to non-isothermal spreading of liquid over the solid of the same material and had approximately the same thermal properties. They also made two improper assumptions that first, the solidification initiates from the basal plane at the trijunction, and second, the droplet

would stop spreading when the contact angle at the solidification front reaches the dynamic contact angle of spreading, none of which they were able to verify experimentally.

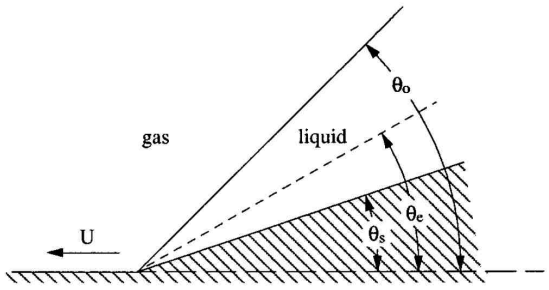

Figure 15. Suggested contact-line region in a melt advancing over a cold solid target[85]. Solid substrate temperature is lower than the fusion temperature of the liquid. θs is the solidification front angle, θ0 is the liquid's apparent dynamic angle, and θe is the equilibrium contact angle.

Bhola and Chandra[88] did an experimental study on the molten droplet impact for low impact velocities only. Aziz et al.[89] studied the impact and solidification of molten metal droplets experimentally under different initial impact velocity and target temperatures. They also used the energy balance criterion to assess the maximum spread factor for metal droplets. Their main focus was to study the spray coating process and to find a prediction for the number of fingers created by the impact of molten droplets, and more importantly, they were only interested in metal droplets with high contact angles.

Tavakoli et al.[90] performed an experimental and theoretical study on the dynamics of spreading drops on undercooled glass substrate. They proposed a new hypothesis to explain the arrest of solidification layer during spreading. They believed that the droplet stops spreading when the volume of the solidified region reaches a critical value. Their hypothesis is based on the initiation of solidification at the contact line and its progression through the liquid following the isotherms. They were able to show that the spread factor is proportional to $Ste^{-1/3}$ for low velocity

deposition of droplets using scaling analysis and verify their results with experiments; however, there are still some unresolved issues in their work. First, their analytical results are based on merely mathematical justifications and the physics behind the critical volume is left unexplained. Secondly, their work is limited to low-velocity forced spreading.

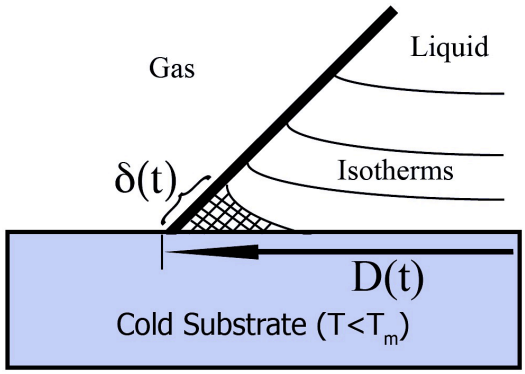

Figure 16. Side view schematics of the initial solidified volume of spreading drop on a cold solid substrate. Isotherms are shown as solid lines perpendicular to liquid surface. Hatched region shows an initial solidified region at the trijunction[90].

Therefore, the models of droplet impact and solidification to this date either have not been validated by experimental results, or cannot explain the physics behind the non-isothermal spreading entirely. Furthermore, the majority of the analytical studies are based on solving the energy balance equation, which is not sufficient for describing the motion and dynamics of impinging droplets[91]. It should also be noted that the prior works in this field focus on either low impact velocity deposition where the impact dynamics are easily negligible or the very high impact velocities in the splashing regime, both of which are extremely hard to control and predict.

This chapter focuses on filling the gap between the very low and very high impact velocities, a region which is referred to as the moderate impact velocities, Table. 1. In this chapter, we aim to

examine the coupled solidification and spreading for a droplet of impact velocity in the intermediate region where the deposition velocities are still high but no splashing is observed and explain the process both analytically and experimentally. The ultimate goal of this chapter is to fully control and predict the final shape of the droplet and maximum spread factor in order to maximize the resolution and efficiency of 3D printers.

Table 1. The previous studies on different regimes of impact velocities for droplet spreading on solid substrate followed by solidification.

$We \ll 1$	$We \sim 1$	$We \gg 1$
Schiaffino et al. 1997[85]		Bennett et al. 1993[94]
Clanet et al. 2004[92]	**This work**	Aziz et al. 2000[89]
Tavakoli et al. 2014[90]		Dhiman et al. 2005[95]
Ruiter et al. 2017[93]		

We present, here, a new hypothesis explaining the arrest of spreading droplets of moderate impact velocities, and a set of experiments to verify the validity of this hypothesis. Based on our hypothesis, for the droplet impinging on a sub-cooled surface at moderate velocities, the final spreading diameter is determined by liquid and surface properties and is independent of impact velocity and degree of sub-cooling. First, we start by analyzing the governing equations for flow in this regime, and obtain the final diameter of spreading based on the proposed hypothesis. The analytical modeling is followed by a series of experiments for different alkanes, all of which show great agreement with the model predictions. The details of the analytical model and experiments are presented in the following section.

3.1.3. Theoretical Analysis

Figure 17 shows the droplet configuration before and during droplet spreading and solidification on a flat plate. In our proposed mathematical model, it is assumed that droplet of initial diameter D_0 strikes a surface perpendicularly with the free fall impact velocity V_i. The fluid flow during droplet impact and spreading is formulated using the axisymmetric coordinate system. The liquid is assumed to be incompressible. The droplet is characterized by initial temperature T_i, density ρ, kinetic viscosity μ, and thermal diffusivity α, and the substrate has a fixed temperature of T_w lower than the droplet melting temperature. Any effect from the ambient air on the droplet including the convective heat transfer is considered negligible. As the droplet hits the surface, it starts spreading in the r-direction; however, because of the temperature gradient at the substrate, liquid near the surface at the trijunction starts solidifying as it spreads. As the liquid at the contact-line solidifies, the solidified region gets pinned to the surface and stops the spreading. The solidification onset mode can be either basal or lateral [43] depending on the droplet contact angle where 90° is the crossing. Here, we focus on the motion and arrest of the contact-line for fluids of contact angle less than 90° where solidification mode is lateral, meaning it initiates from the trijunction and propagates inside the droplet following the isotherms.

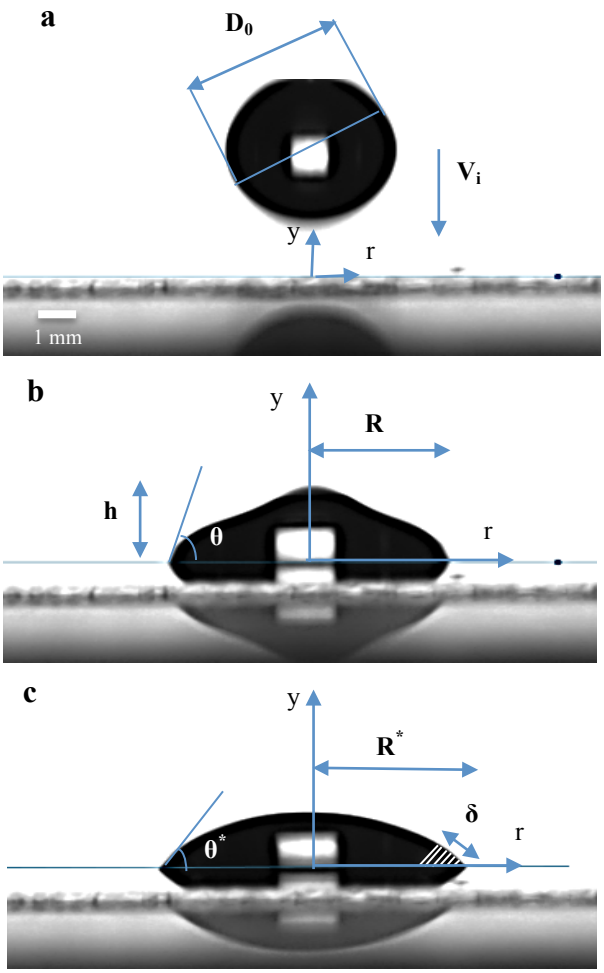

Figure 17. Sequence of droplet deposition and spreading on a solid substrate of temperature lower than its melting point.

To determine the arrest diameter and quantify the effect of different initial conditions such as impact velocity, target temperature, fluid properties, and etc. on spreading of the droplet on a cold substrate followed by phase-change, we have performed scaling analysis of the governing equations. We start by momentum equation at the contact-line:

$$\left[\frac{\partial \vec{V}}{\partial t} + (\vec{V}.\nabla)\vec{V}\right] = -\frac{\nabla P}{\rho} + \vec{g} + \nu\nabla^2\vec{V} \qquad (8)$$

Based on the scaling analysis of the continuity equation, it can be shown that $v \sim Uh/R$ where U and v are the velocity in the r and y directions respectively. We plugged this result into the r-

momentum equation, using the assumption that $h/R \ll 1$, which is valid for wetting liquids, and simplified the remaining terms to obtain an order of magnitude relation between the terms:

$$\frac{U^2}{R} \sim \frac{\Delta P}{\rho R} \sim \frac{\nu U}{h^2} \tag{9}$$

In the limit of moderate impact velocities, where spreading is driven by impact-induced forces but no fingering or instabilities occur at the trijunction, i.e. $We = \rho V^2 D/\sigma > 1$ and $Re = \rho VD/\mu > 1$, the flow at the contact-line is driven by impact-induced forces and resisted via inertia and capillary pressure at the contact-line. Here, we have neglected the viscous effects on the grounds that at relatively high *Re*, the thickness of the boundary layer is very small compared to other flow dimensions; hence, an inviscid flow assumption. For inviscid flow inside the droplet, the force balance at the contact-line becomes:

$$\frac{U^2}{R} \sim \frac{\Delta P}{\rho R} \tag{10}$$

At the free surface, the normal stresses are replaced by an equivalent surface pressure, calculated from the interface mechanical equilibrium condition given by the Laplace's equation, $\Delta P = \sigma\kappa$, where σ is the liquid-gas surface tension, and κ is the interface mean curvature at the trijunction. This curvature can be easily obtained using the geometry of droplet, $\kappa = R_0/R^2$. Using these equations, we can simply find the spreading radius as a function of time and fluid properties as follows:

$$R \sim \sqrt[4]{\frac{\sigma R_0}{\rho}}\, t^{\frac{1}{2}} \tag{11}$$

It should be noted that equation (11) corresponds to the kinematic stage of spreading, which is the initial stage of spreading after the droplet hits the substrate. For moderate impact velocities,

the onset of solidification, the solidified front growth, and its subsequent arrest happen while in the kinematic spreading stage.

As the droplet is spreading over the surface, the liquid near the surface at the trijunction starts solidifying. Before the onset of solidification, the droplet spreading follows the isothermal spreading dynamics regardless of the degree of undercooling. As the liquid starts solidifying and solidification front grows, it pines the contact-line to the surface and stops the spreading. The solidification front grows in time following the well-known solidification equation[96], $\delta = \sqrt{4\alpha t Ste}$, where $Ste = C_p(T_m - T)/L_f$. It should be noted that since the size of the droplets is small, no nucleation consideration is necessary[97,98]. There are different hypotheses regarding the contact-line pinning due to solidification, all with limited success.

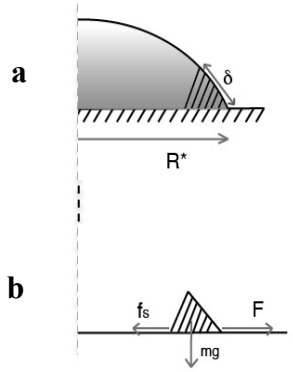

Figure 18. a) The axisymmetric view of the growth of solidification front following the isotherms for a droplet on a surface with contact angle smaller than 90 degrees. b) The force balance on the solidified region.

Our hypothesis for solidification arrest is that as the mass of solid is enlarging, the friction force increases (the friction force is proportional to the mass of the solidified region), and eventually, the friction force will reach the static friction force, f_s, which stops the movement of the contact-line and spreading of droplet on the surface (Figure 18). In other words, the arrest of contact-line in non-isothermal spreading happens due to the increase in the friction force applied to the

solidified material, which further stops the spreading of the liquid behind it. To entertain this hypothesis, we have studied the force balance at the solidified region:

$$\frac{d}{dt}(m_s U) = \mu m_s g \tag{12}$$

$$m_s = \pi R \rho_s \delta^2 tan\theta \tag{13}$$

where R, θ, ρ_s, and μ are spreading radius and contact angle, density of solidified material, and friction coefficient. Equation (12) is the force balance for the solidified material. The solidified material is growing and moving at the contact-line as a result of droplet spreading, while the friction between the solidified material and substrate is resisting this motion. Equation (14) is the result of the order of magnitude analysis of equation (12), which shows the balance of inertia and friction force for the solidified region.

$$\frac{U}{t} \sim \mu g \tag{14}$$

Taking the scaling analysis one step further, the contact-line velocity in r-direction is scaled by the ratio of spreading radius over time of spreading as shown in equation (15).

$$\frac{R}{t^2} \sim \mu g \tag{15}$$

Finally, combining the previously derived equation for spreading dynamics, equation (11), with equation 8, the time factor is eliminated.

$$\frac{\sigma R_0}{\rho R^3} \sim \mu g \tag{16}$$

Based on our hypothesis, the spreading stops when the friction force reaches its maximum value, the static friction. Thus, to find an order magnitude estimate for the final arrest radius, R^*, the friction coefficient is replaced by static friction coefficient, μ_s that results in the following:

$$\frac{\sigma R_0}{\rho R^{*3}} \sim \mu_s g \tag{17}$$

By rearranging equation (17), we can simply obtain equations 18 and 19, which show the arrest radius and spread factor for the droplet impingement onto a solid substrate with moderate impact velocity, respectively. It should be noted that based on these results the arrest radius is independent of impact velocity and/or the degree of undercooling, and it only depends on solid and fluid physical properties as well as the initial volume of the droplet.

$$R^* \sim \sqrt[3]{\frac{\sigma}{\rho \mu_s g}} \sqrt[3]{R_0} \tag{18}$$

$$\varepsilon \sim \sqrt[3]{\frac{\sigma}{\rho \mu_s g R_0^2}} \tag{19}$$

3.1.4. Experimental Study

To verify the results of the analytical modeling, experimental measurements for two different liquids of similar properties and same initial volume are performed over a variety of dynamic and thermal conditions.

Experiments are carried out inside Krüss DSA 100 at various combinations of the substrate temperature, droplet impact velocity, dispensing needle position, and dispensing flow rate. Krüss DSA100 is also used for recording the droplet spreading dynamics and subsequent data evaluation. In principle, the Krüss DSA 100 machine consists of three main components (i) the specimen table with three manual knobs for accurate 3D positioning (ii) the video system with CCD camera, prism, light source and aperture (iii) a software-controlled multiple dosing unit. This state-of-the-art apparatus provides accurate measurement of the dynamic contact angle and base diameter of the spreading fluid. The intelligent dosing system of Krüss DSA 100 allows

liquid to be dispensed without the risk of contaminating the sample. The bright light with extremely low radiated heat provides us with the illumination required for measuring drop radius evolution. The drop is illuminated from one side and a camera at the opposite side records images of the drop spreading and solidification. Temperature of the solid targets can be adjusted by a Peltier element situated in Krüss DSA100 machine from -30 °C to 160 °C.

The free fall impact experiments of single drops are conducted for a range of *We* from 0.5 to 53.1 and *Ste* from 0.1 to 0.3 on glass slides with dimensions of 50×24×0.15 mm^3 (VWR microcover glass). The substrate is rinsed successively in acetone, methanol, and DI water. Different impact velocities are obtained by changing the height of the needle with respect to the solid target. Higher elevations of the injection needle correspond to higher Weber numbers. During the liquid discharge from the injection needle, the drop becomes larger in size and eventually falls under its own weight. The volume of droplet is set to $5\mu l$ and kept constant for all the experiments. In all experiments, the arrested base radius, R^* is measured at the moment that the drop gets pinned down due to solidification initiation.

In these experiments, n-Hexadecane and n-Pentadecane are used as test fluids. The fluid characteristics are listed in Table 2. The reported values for the fluid properties are provided by the manufacturer. The contact angle values, equilibrium and advancing, are measured for each set of experiment, and all the values are consistently below 90°, which is the criterion for the analytical modeling.

Table 2. Properties of the fluids at room temperature

Fluid	Density (kg/m^3)	Absolute Viscosity (kg/m.s)	Surface Tension (mN/m)	Latent Heat (J/kg)	Specific Heat Capacity (J/gr.K)	Thermal Conductivity (W/m.K)	Melting Point (°C)

n-Hexadecane	773	3.34×10^{-3}	29.23	2.29×10^{5}	2.31	0.21	18.6
n-Pentadecane	769	3.70×10^{-3}	25.90	2.05×10^{5}	2.23	0.17	9.9

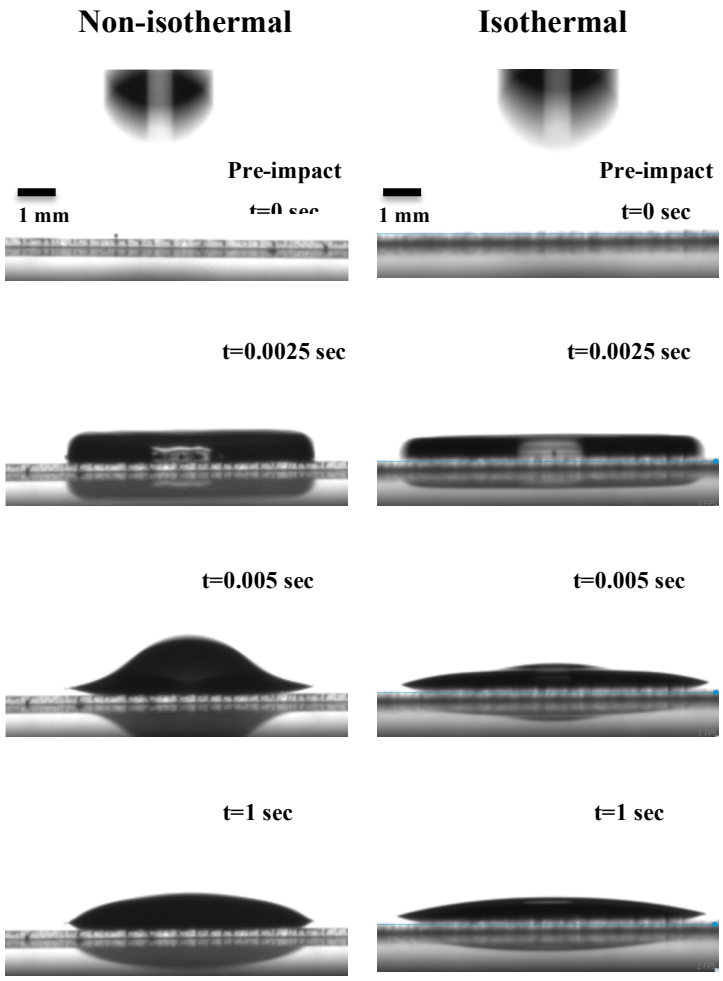

Figure 19. The video sequence of the impact and spreading of an n-Hexadecane droplet on with and without solidification. The drop has the initial volume of 5µl. The comparison of non-isothermal and isothermal spreading of impinging drops under the same impact dynamics shows the effect of lateral solidification on the arrest of contact-line. The substrate temperatures for non-isothermal and isothermal experiment are −20°C and 20°C respectively.

Figure 19 shows a comparison between the isothermal and non-isothermal spreading under the same impact conditions. It can clearly be seen how solidification pins the spreading contact-line to the surface, and changes the profile and final shape of the solidified droplet. Based on the

experimental data presented in Figures 20, 21, and 22, as the impact velocity increases, the arrest radius becomes entirely independent of *Ste* and *We,* which is aligned with the prediction of our analytical model. Figure 20 shows the spread factor, versus *Ste* for different impact velocities of n-Hexadecane droplet on a cover glass substrate. Each point on this plot is the average of five sets of experiments at arbitrary locations. It is clear that for low *We* experiment (*We=0.55*), the radius of droplet is changing rapidly with *Ste;* however, as *We* increases and the droplet impact velocity falls within the moderate velocity regime, the plot becomes a plateau and the arrest radius becomes independent of both *Ste* and *We*. Figure 21 shows the results for droplets of moderate impact velocities with and without solidification. For sub-cooled substrates, it is shown that as *We* increases, all the lines merge into one single value for final radius of droplet. This outcome is consistent with the prediction of our analytical model (dashed line on Figures 20, 21, and 22) and prior experimental data[75,88]. For the isothermal spreading, on the other hand, the final radius is clearly increasing with increase in impact velocities and is much higher than the final radius of spreading coupled with solidification, all of which highlights the importance of solidification on controlling the spreading dynamics in the moderate regime.

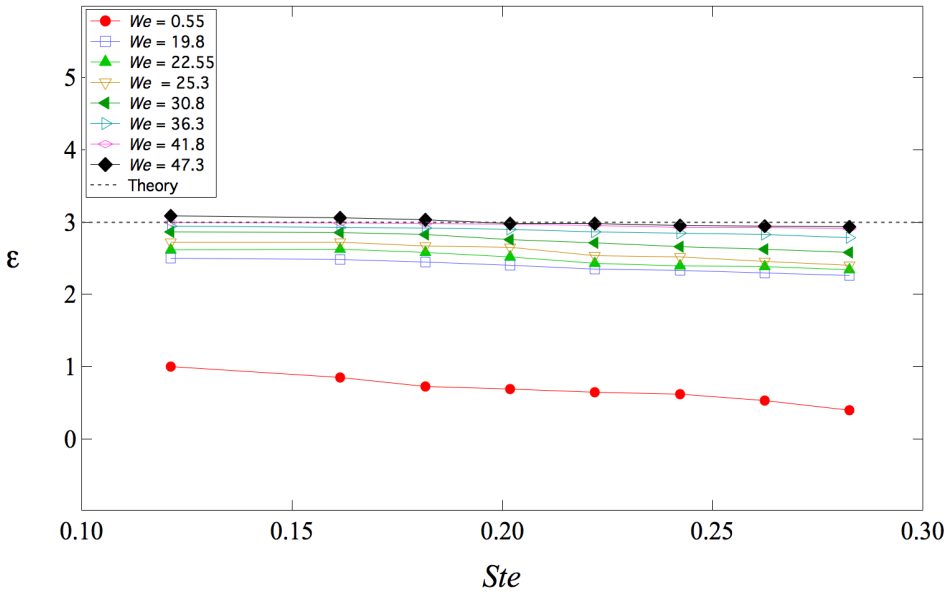

Figure 20. Spread factor as a function of Ste for free fall of n-Hexadecane on glass substrates. The values of impact velocities corresponding to different *We* are the following: 0.44, 2.65, 2.83, 3, 3.31, 3.59, 3.86, and 4.1 m/s.

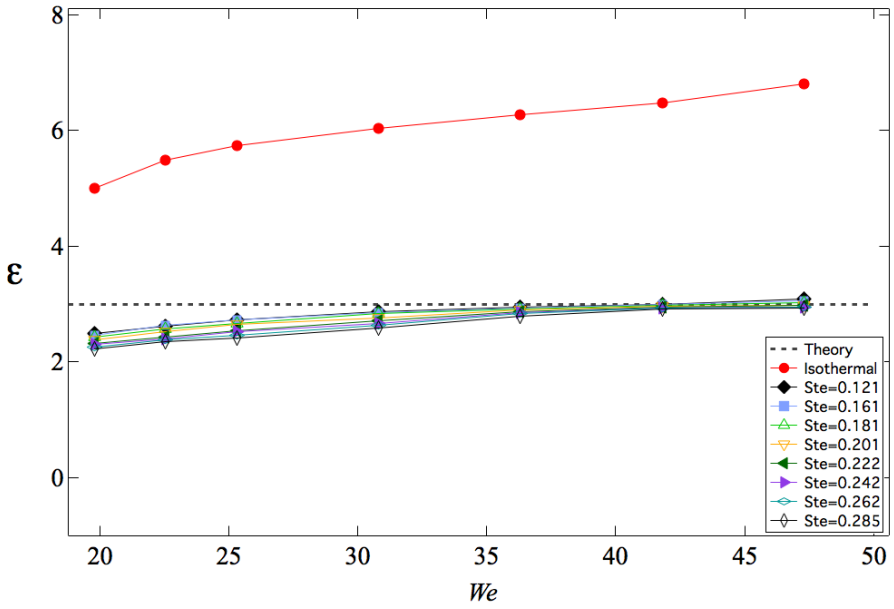

Figure 21. Spread factor as a function of *We* for free fall of n-Hexadecane on glass substrates at moderate impact velocities with and without solidification.

As both n-Hexadecane and n-Pentadecane droplets have similar properties and initial volume, the measure of arrest radius should be approximately the same based on the proposed hypothesis. To test our hypothesis further, same sets of experiments are performed using n-Pentadecane, and the results are plotted and superimposed with n-Hexadecane data in Figure 22. For low *We* experiments of both fluids, it is shown that arrest radius is decreasing as *Ste* increases, and the measured values of arrest radius for n-Pentadecane are considerably different in comparison to the n-Hexadecane. However, at moderate impact velocity experiments, the spread factor becomes approximately the same and in great agreement with the predicted value from the analytical model.

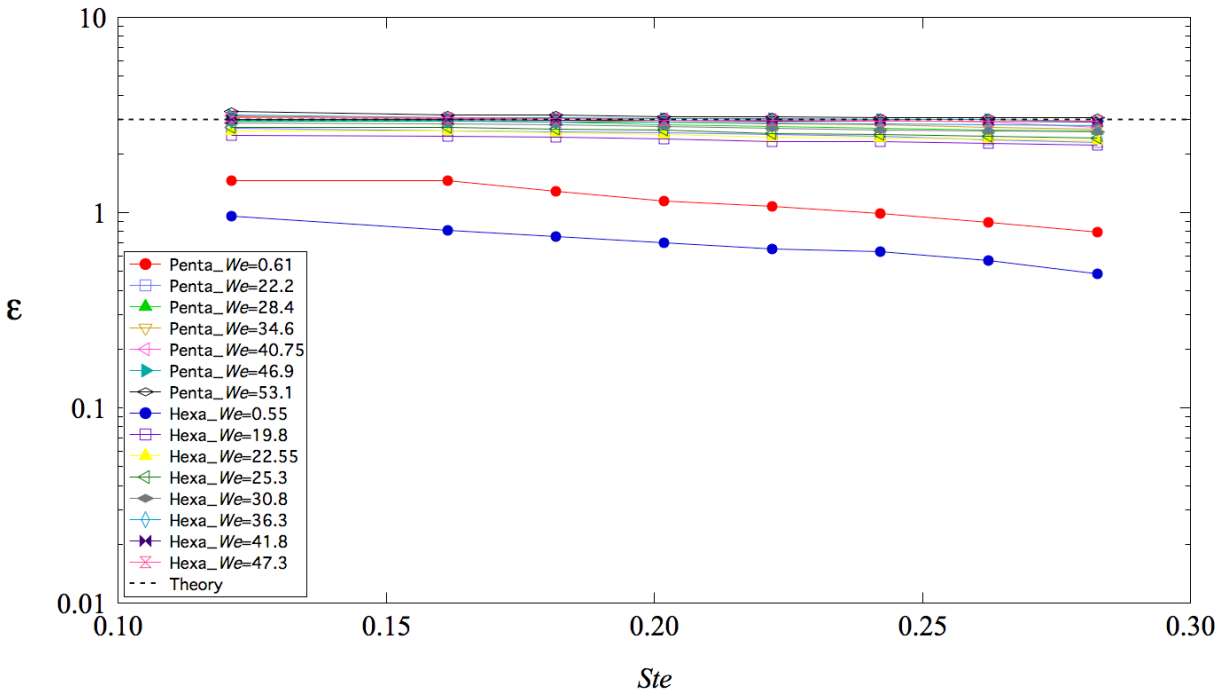

Figure 22. Spread factor as a function of *Ste* for free fall of n-Pentadecane and n-Hexadecane on glass substrates. The dashed lines on all figures represent the predicted value by the analytical model which is in great consistency with the experimental results. The values of impact velocities for both fluids are the following: 0.44, 2.65, 2.83, 3, 3.31, 3.59, 3.86, and 4.1 m/s.

3.1.5. Conclusion

We have performed an experimental and theoretical study on the dynamics of non-isothermal spreading of impinging droplets with moderate impact velocities. In this range of velocities, the impact velocities are high enough that the impact-induced forces play an important role in droplet spreading and cannot be neglected, but the velocities are low enough to ensure fingering and/or break-ups do not occur.

A new hypothesis is presented aiming to explain the physics behind the spreading dynamics followed by solidification. This hypothesis is based on the initiation of the solidified layer from the contact-line and ascending through the liquid bulk. We have shown that as the mass of the

solid is growing due to solidification, the measure of kinetic friction is growing with the same rate, and eventually, the kinetic friction reaches the value of static friction, which stops the movement of the contact-line. The scaling analysis suggests that in the case of moderate impact velocity deposition of droplets, the arrest radius of drop only depends on fluid and surface properties and initial volume of droplet and is independent of initial impact velocity and temperature difference between solid substrate and droplet.

To verify the analytical results, a series of experiments are performed using different liquids under variety of initial conditions. The values of arrest radius for moderate velocities are measured using a high-speed photography. The results show that the R^* for moderate impact velocity experiments (no fingering or breakup instabilities) and small arrested contact angles (less than 90°) is independent of *We*, *Ste*, and other initial conditions. Therefore, the effect of solidification on the spreading dynamics in this region is very important as it limits the spreading to a certain arrest radius that cannot be altered by merely changing the impact velocities and temperature gradients.

Thus, there exists a stable non-isothermal spreading regime independent of initial conditions, which allows us to entirely control and adjust the footprint which is applicable to many areas of industry for such as 3D printing.

4. Enhanced Condensation Heat Transfer on Surfaces with Biphilic Topography

Optimization of the efficiency of the condensers *via* different surface engineering techniques is a subject of interest due to its wide range of application in thermal management for aerospace vehicles, power generation systems, and etc., which will further result in considerable savings in annual investments and operating costs by millions of dollars. However, the current technologies are lacking either the necessary condensation enhancements or cost-effective, large-scale fabrication method. In this work, we present a new surface topography to enhance drop-wise condensation at low manufacturing costs. These surfaces consist of macro-scale hydrophobic patterns on hydrophilic structures. Due to their high wettability contrast, the biphilic surfaces enhance drop-wise condensation with long-term functionality, and more importantly, they can be easily manufactured in large-scale using conventional methods as no nano- or micro-features are needed. The analytical and experimental analyses presented in this work also verify the heat transfer enhancements of these surfaces.

4.1.1. Introduction

One of the main technical challenges in a variety of industrial fields including aircrafts, power plants, and water desalination systems is the effective discharge of excessive heat generated inside the system. From thermal management point of view, condensation or phase change in general is considered the most optimum way of removing waste heat from the system due to its high heat transfer rate. Efficiency of the thermal transfer during condensation strongly depends on the mode of condensation, namely drop-wise and film-wise condensation [99-103]. The current industrial condensers, however, are very inefficient because they rely on film-wise condensation for waste heat removal. The film-wise condensation offers low heat transfer coefficient due to

thermal resistance imposed by the liquid layer as when the film is formed, it acts as a barrier to thermal transfer and impedes the continuous heat transfer from the condensing surface.

Several researchers have tried to address this issue and find ways to improve the heat transfer efficiency by enhancing drop-wise condensation on the condensing surfaces [104-106]. Unlike film-wise condensation, the drop-wise condensation is achieved on a surface that is not wetted by the condensate. In drop-wise condensation, there is a continuous surface renewal by falling drops resulting in at least 10-fold enhancement in heat transfer rate compared to the film-wise condensation [99,107-112].

The current technology to promote drop-wise condensation is limited to hydrophobic coatings [113-116] or nano-engineered textured surfaces [105,117-121]. The hydrophobic coatings have short life span and tend to come off depending on the working conditions in a few hours. These coatings are mainly polymer based with low thermal conductivity; thus, covering the condensing surface with the coating impedes the heat transfer and reduces the overall efficiency.

The superhydrophobic nano-patterned surfaces allow sustained drop-wise condensation and have shown considerably higher enhancements in heat transfer compared to hydrophobic coatings due to variety of reasons. For example, superhydrophobic surfaces can significantly increase the mobility of the droplets leading to a combination of both gravity-driven falling droplets as well as self-propelled jumping droplets. These surfaces are mostly metal substrates with nano-features, hence high thermal conductivity. However, the nucleation energy barrier is much higher on superhydrophobic surfaces compared to hydrophilic surfaces, which causes a significant reduction in droplet number density, and more importantly the manufacturing process for nano-engineered surfaces is neither cost-effective nor scalable.

Therefore, the state-of-the-art condensing surfaces cannot be applied to industrial applications due to their high manufacturing costs and difficulty in maintaining drop-wise condensation in long run. In order to tune the advantage of lower energy barrier accompanied with hydrophilic surfaces and higher drop mobility of super-hydrophobic surfaces, Kumagai et al.[122] entertained the possibility of using biphilic patterning of surfaces. Results showed a great potential of using such surfaces with heat transfer performance bounded by the two extreme cases, i.e. film and drop wise condensation. After this work, several researchers studied different configurations, such as biphilic strips[123-125], biphilic dotted surfaces[126] and biphilic pillars[127].

This chapter focuses on development of biphilic surfaces with high wettability contrast to boost drop wise condensation, while maintaining high conduction rate through the surface at low manufacturing costs. Previously engineered biphilic surfaces are different arrangements of superhydrophobic designs on hydrophilic substrates that despite their high heat transfer efficiency, cannot overcome the large-scale fabrication challenges and are inapplicable to industrial systems [121,128,129]. The unique aspect of our work is to design a hybrid hydrophilic-hydrophobic surface in which the variation in interfacial energy is achieved through crafting millimeter-sized hydrophobic patterns on metal substrates that not only leads to high thermal transfer efficiency but also can be manufactured using scalable fabrication techniques.

4.1.2. Biphilic Surfaces

Biphilic surfaces consist of hydrophobic patterns on hydrophilic structures as shown in Figure 23. The hydrophilic base provides high thermal conductivity and low nucleation activation energy resulting in enhanced vapor condensation rate, and the hydrophobic patterns inhibit

transition to film-wise condensation and enhance the rate of droplet removal from the condensing surface, all of which increases the overall heat transfer efficiency.

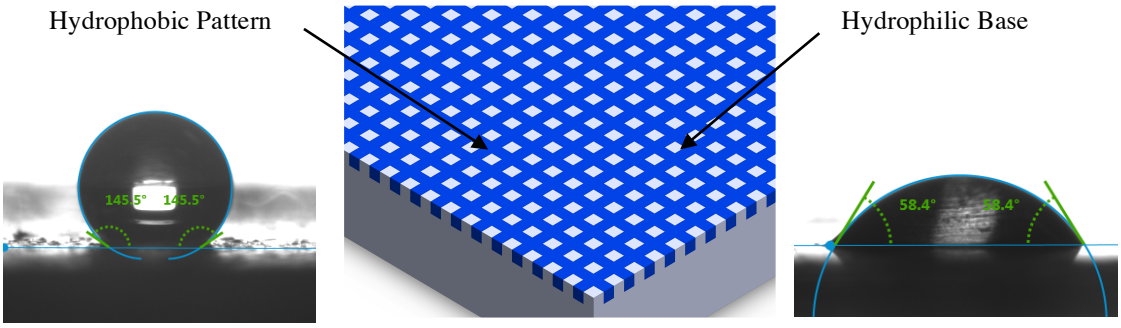

Figure 23. Schematic drawing of biphilic surface showing the hydrophobic pattern on a hydrophilic base. The contact angle of water on the hydrophobic and hydrophilic sites are 145° and 58° respectively.

4.1.3. Mathematical Modeling

Understanding the mechanism of drop-wise condensation is essential in design and optimization of durable surfaces with enhanced drop-wise condensation for industrial applications. There are several theories on drop formation and heat and mass transport during drop-wise condensation [101,130-132] The most commonly used theory for modeling of drop-wise condensation was first introduced by Eucken (1937) [133], which is based on small droplet formation by direct condensation on nucleation sites randomly distributed over the condensing surface. According to this theory, as the clusters of vapor reach a maximum size adjacent to the condensing surface, they form small drops of stable thermodynamically minimum radius at sites with the smallest free energy barrier. The small drops grow by direct condensation only until they reach the mean nucleation site spacing at which the neighboring drops start to coalescence. The large droplets then fall-off of the condensing surface reaching the critical drop size due to the force instabilities at the contact-line. To properly model the drop-wise condensation and calculate the overall heat flux and heat removal efficiency via different condensing surfaces, a comprehensive

understanding of all the sub-processes is necessary. Drop-wise condensation consists of a series of random fundamentally unsteady sub-processes over a wide range of time- and length-scales, viz. initial nucleation, droplet growth by direct condensation, coalescence, droplet instability and fall-off, and renucleation of fresh droplets [134].

The first step in drop-wise condensation process is the heterogeneous nucleation, which depends on the number of active nucleation sites on the condensing surface. The nucleation site density, $\boldsymbol{N_s}$, varies with surface topography and thermodynamic properties of fluid, and extent of subcooling [134,135]. Based on the experimental data, the nucleation site density was found to be within the range of 10^9 m^{-2} to 10^{15} m^{-2} [136,137]. For the purpose of the heat transfer modeling of drop-wise condensation, we assume the nucleation site density to be at 10^{10} m^{-2}.

The small drops that are formed by nucleation continue to grow by direct condensation. The smallest stable droplet radius, $\boldsymbol{r_{min}}$, can be found using the classical nucleation theory [100,111].

$$\boldsymbol{r_{min} = \frac{2T_{sat}\sigma}{h_{fg}\rho(T_{sat}-T_w)}} \tag{20}$$

For small non-interacting droplets, the droplet size distribution is calculated following the population balance theory. The population balance theory is based on the droplet number conservation in a certain droplet radius range. In other words, for an arbitrary size range of $(r_1 - r_2)$, the number of droplet entering the size range minus the number of droplet leaving the size range is equal to the number of droplet fall-off of the surface [111,138,139]:

$$\boldsymbol{An_1G_1dt = An_2G_2dt + Sn_{1-2}dtdr} \tag{21}$$

$$\boldsymbol{G = \frac{dr}{dt}} \tag{22}$$

where A, G, n_1, n_2, S, and $n_{1\text{-}2}$ are the surface area, droplet growth rate, number density of the droplet of radius r_1, number density of the droplet of radius r_2, sweeping (or falling) rate, and average population density in the size range. In the limit of infinitesimally small size range, equation (21) reduces to:

$$\frac{d(Gn)}{dr} = \frac{-n}{\tau} \tag{23}$$

where $\boldsymbol{\tau = A/S}$ is the sweeping period. The number density for small droplets can be eventually obtained by solving equation (23), which requires additional information discussed in the following steps.

The next step is the large droplet growth by coalescence of the neighboring drops. There is a well-known equation for number distribution of large droplets derived by Le Fevre and Rose in 1966 [140] and Glicksman in 1972 [141].

$$\boldsymbol{N(r) = \frac{1}{3\pi r^2 r_{max}} \left(\frac{r}{r_{max}}\right)^{-2/3}} \tag{24}$$

where $\boldsymbol{r_{max}}$ is the maximum radius beyond which the drop falls off of the surface. The maximum droplet radius is where the tangential component of droplet weight reaches the interfacial force at the contact-line. Following the force balance equation, the fall-off radius can be determined as [142]:

$$\boldsymbol{r_{max} = \sqrt{\frac{6\sigma(cos\theta_r - cos\theta_a)sin\theta_{avg}}{\rho g\pi(2 - 3cos\theta_{avg} + cos^3\theta_{avg})sin\alpha}}} \tag{25}$$

Where $\boldsymbol{\rho}$, $\boldsymbol{\sigma}$, $\boldsymbol{\theta_r}$, $\boldsymbol{\theta_a}$, $\boldsymbol{\theta_{avg}}$, and $\boldsymbol{\alpha}$ are liquid density, surface tension, receding contact angle, advancing contact angle, equilibrium contact angle, and the substrate inclination angle, which is 90° for vertical substrate, respectively. The fall-off radius, as seen in equation (25), strongly depends on the contact angle of the liquid droplet on the condensing surface, for example, for

hydrophobic substrates, the fall-off radius is smaller than hydrophilic surfaces. It should be noted the reduction in fall-off radius is equivalent to better thermal transfer as large droplets are removed and replaced by small droplets at a faster rate.

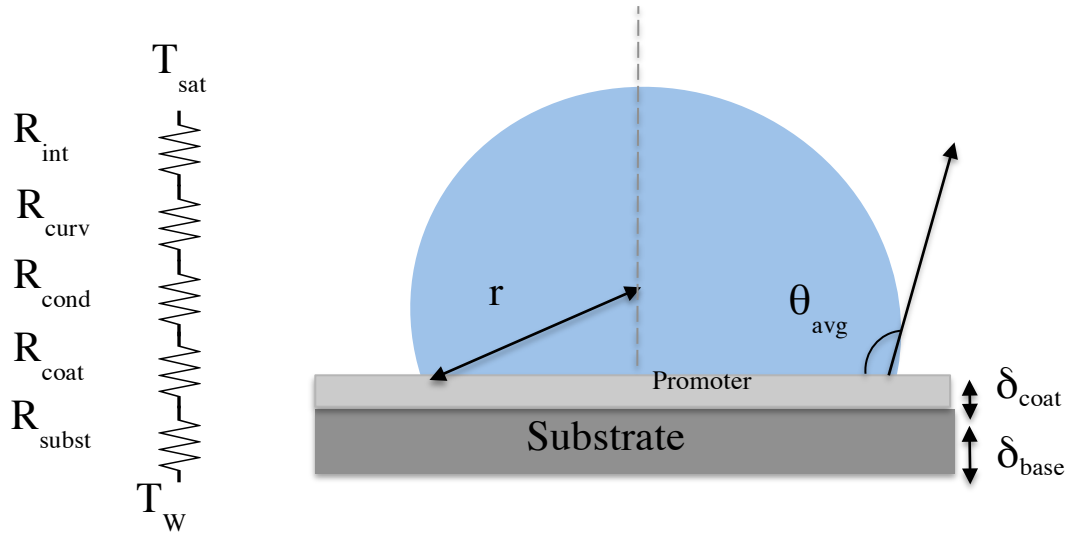

Figure 24. Drawing of droplet on a condenser surface with the related thermal resistance network that includes the liquid-vapor interface resistance, the curvature resistance, the droplet conduction resistance, the hydrophobic promoter resistance, and finally the thermal resistance in the substrate. The hydrophobic promoter has the thickness of δcoat on hydrophobic sites and zero on hydrophilic base.

The overall heat transfer through the condensing surface is calculated by integrating the heat flux through one single droplet over the condenser surface area for all the droplets both large and small based on the number densities calculated earlier [112,139,143]. The heat transfer rate for a single droplet, $\boldsymbol{q_d}$, is determined using the standard thermal resistive model [134,138] shown in Figure 24. The temperature drop from the saturated vapor, $\boldsymbol{T_{sat}}$, to the substrate, $\boldsymbol{T_w}$, is calculated considering all the thermal resistances in between namely the vapor-liquid interface resistance, the droplet curvature resistance, conduction resistance, coating resistance, and finally resistance through the substrate. The equation for the total temperature drop, $\Delta \boldsymbol{T_t}$, is given by:

$$\Delta \boldsymbol{T_t} = \boldsymbol{T_{sat}} - \boldsymbol{T_w} = \Delta \boldsymbol{T_{int}} + \Delta \boldsymbol{T_{cur}} + \Delta \boldsymbol{T_{cond}} + \Delta \boldsymbol{T_{coat}} + \Delta \boldsymbol{T_{sub}} \quad (26)$$

$$T_{sat} - T_w =$$

$$\frac{q_d}{2\pi r^2 h_{int}(1-cos\theta_{avg})} + \frac{r_{min}(T_{sat}-T_w)}{r} + \frac{q_d\theta_{avg}}{4\pi r k_l sin\theta_{avg}} + \frac{q_d\delta_{coat}}{\pi r^2 k_{coat}(1-cos^2\theta_{avg})} + \frac{q_d\delta_{base}}{\pi r^2 k_{base}(1-cos^2\theta_{avg})} \quad (27)$$

where δ_{coat}, δ_{base}, h_{fg}, h_{int}, k_l, k_{coat}, and k_{base} are the coating thickness, the base thickness, the latent heat of vaporization, the interfacial heat transfer coefficient, liquid thermal conductivity, the coating thermal conductivity, and the base thermal conductivity. The heat transfer rate through a single droplet can be replaced using the latent heat equation for a droplet of growing radius and changing contact angle:

$$q_d = \pi\rho h_{fg} r^2 G\left\{\left(1 - cos^2\theta_{avg}\right)sin\theta_{avg}\frac{d\theta_{avg}}{dr}r + \left(1 - cos\theta_{avg}\right)^2\left(2 + \cos\theta_{avg}\right)\right\} \quad (28)$$

It should be noted that the first term in equation (28) associated with the change in contact angle across the surface is only zero for surfaces with constant wettability. By plugging in equation (28) back into equation (27), the droplet growth rate can be found in terms of the temperature drop and the liquid and substrate properties.

$$G =$$

$$\left(\frac{(1-cos\theta_{avg})\times\left(\frac{T_{sat}-T_w}{\rho h_{fg}}\right)}{(1-cos^2\theta_{avg})sin\theta_{avg}\frac{d\theta}{dr}r+(1-cos\theta_{avg})^2(2+\cos\theta_{avg})}\right)\times$$

$$\left(\frac{\left(1-\frac{r_{min}}{r}\right)}{\frac{1}{2h_{int}}+\frac{r(1-cos\theta_{avg})\theta_{avg}}{4k_l sin\theta_{avg}}+\frac{\delta_{coat}}{k_{coat}(1+cos\theta_{avg})}+\frac{\delta_{base}}{k_{base}(1+cos\theta_{avg})}}\right) \quad (29)$$

Finally, the number density for small droplets can be calculated from integrating equation (23) by replacing the droplet growth rate using equation (29). As the number density function has to be continuous, the value for number density of the small drops at its upper limit should be equal to the lower limit of the number density of large drops. The radius where the large and small

number density functions meet is called effective radius, $\boldsymbol{r_e}$, which is equal to the half of the spacing between the active nucleation sites, $\boldsymbol{l_c}$, beyond which neighboring droplets can merge.

$$\boldsymbol{r_c = \frac{l_c}{2} = \frac{1}{\sqrt{4N_s}}} \tag{30}$$

$$\boldsymbol{N(r_e) = n(r_e)} \tag{31}$$

Therefore, the overall heat transfer rate, $\boldsymbol{q''}$, through the condensing surface can be calculated *via* the following equation [143]:

$$\boldsymbol{q'' = \int_{r_{min}}^{r_e} q_d(r) n(r) dr + \int_{r_e}^{r_{max}} q_d(r) N(r) dr} \tag{32}$$

4.1.4. Biphilic vs. Hydrophobic and Hydrophilic

Here, we are going to numerically compare the performance of the biphilic surfaces to all-hydrophobic and all-hydrophilic substrates. The previous models on condensation heat transfer are mostly applicable to substrates with constant wettability across the surface area; hence zero contact angle gradient with respect to droplet radius. However, for biphilic surfaces, the contact angle changes throughout the surface depending on the pattern size, γ. Another important thing to consider when studying biphilic surfaces is the maximum or fall-off radius. For biphilic surfaces, first of all, the fall-off radius for droplets on hydrophobic site is different than fall-off radius on hydrophilic base due to the change in dynamic and equilibrium contact angles on these surfaces, and secondly, the fall-off radius is not determined by equation (26) solely, but it also depends on the pattern size as for example, droplets growing on hydrophilic base cannot extend past the hydrophobic boundary on account of the reduction in adhesion forces. Thus, the maximum droplet radius on biphilic surfaces is found using the contact-line force balance combined with the pattern spacing.

We have incorporated the details, listed above, specific to biphilic surfaces in our model to provide a more accurate heat transfer analysis for these surfaces. To assess the quality of the biphilic surfaces compared to all-hydrophobic and all-hydrophilic substrates, first thing to consider is the number density of small and large droplets on these surfaces, shown in Figure 25. The hydrophobic surface seems to have the highest number densities for both the large and small droplets, the hydrophilic surface has the lowest number densities, and finally the biphilic surface sits somewhere in between. It should be noted that higher number densities especially for small droplets are more favorable in terms of enhancing the rate of heat transfer. Therefore, to this point, merely based on the number densities, the hydrophobic substrate appears to be the better option.

The fall-off radius is another important quantity that should be considered. The smaller fall-off radius represents a better thermal transfer for rapid droplet removal from the surface makes room for fresh small droplet formation and consequently continual heat removal from the condensing surface. The values for fall-off radii are shown in Figure 25. The hydrophobic surface has smaller fall-off radius compared to hydrophilic surface as expected. The biphilic surface, on the other hand, has two fall-off radii, one for the droplet sitting on hydrophobic pattern and one for hydrophilic base. The hydrophobic pattern fall-off radius is same as all-hydrophobic substrate only if the pattern spacing is bigger than the fall-off diameter because the droplet would fall-off of the surface before it can grow outside the pattern. For the hydrophilic base, however, the fall-off radius is limited by the pattern spacing, which is much smaller than fall-off radius on the all-hydrophilic surface.

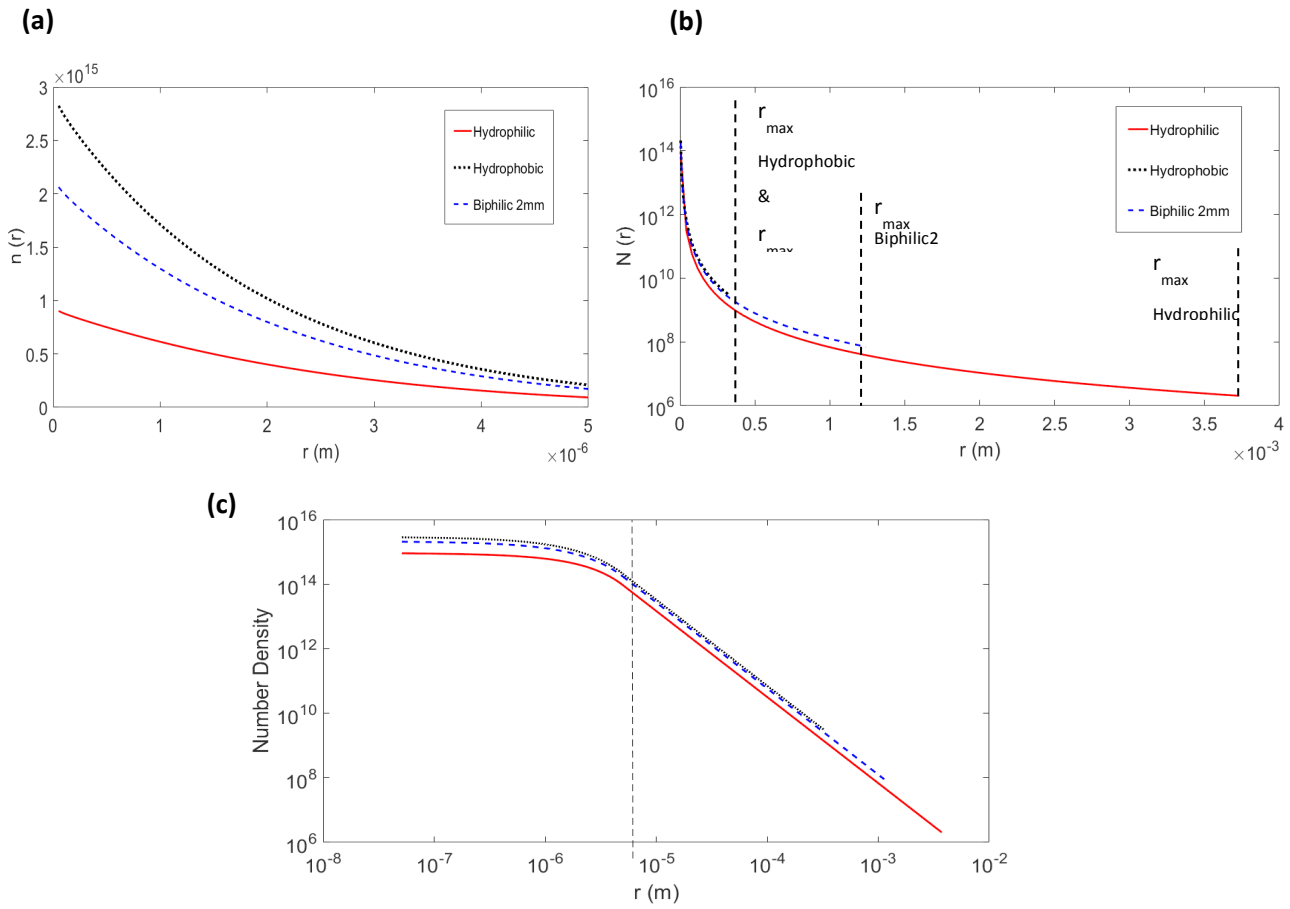

Figure 25. Droplet size distribution as a function of droplet radius for hydrophilic, hydrophobic, and 2mm biphilic substrates. (a) The number densities are shown for small droplets formed by direct condensation. (b) The number densities are shown for large droplets formed by coalescence. The fall-off radii are shown for each substrate. The biphilic surface has two separate fall-off radii corresponding to the hydrophobic sites and hydrophilic base marked as biphilic1 and biphilic2 respectively. (c) The log-log graph of combined number densities for all droplets from initial nucleation to fall-off. The dashed line shows the borderline between small droplets and large droplets. The associated model parameters are: T_{sat} = 20°C, T_w = -10°C, δ_{coat} = 1µm, k_{coat} = 0.15 W/m.K, γ = 2mm, hydrophobic θ_a and θ_r are 150° and 144°, and hydrophilic θ_a and θ_r are 73° and 34°.

The third important factor is the rate of heat transfer for droplets of specific radius, single drop heat transfer rate multiplied by number density at that desired radius, and finally the overall rate of heat transfer through the surface. Figure 26 shows the heat transfer rate versus the droplet radius. As you can see, the heat transfer rate strongly depends on the value of contact angle as

increase in contact angle imposes a barrier to thermal transport through the droplet by changing the profile of the isotherms within the drop [43]. As a result, the rate of heat transfer for drops of specific radius is much smaller on hydrophobic substrate all around the range of droplet radius, and the hydrophilic surface has the highest values at all points. Although the hydrophobic surfaces had very high number densities, their local heat transfer rate is comparably small. However, biphilic surfaces have the number density and fall-off radius close to those of hydrophobic surface and the local rate of heat transfer close to hydrophilic surface; hence best of the two categories.

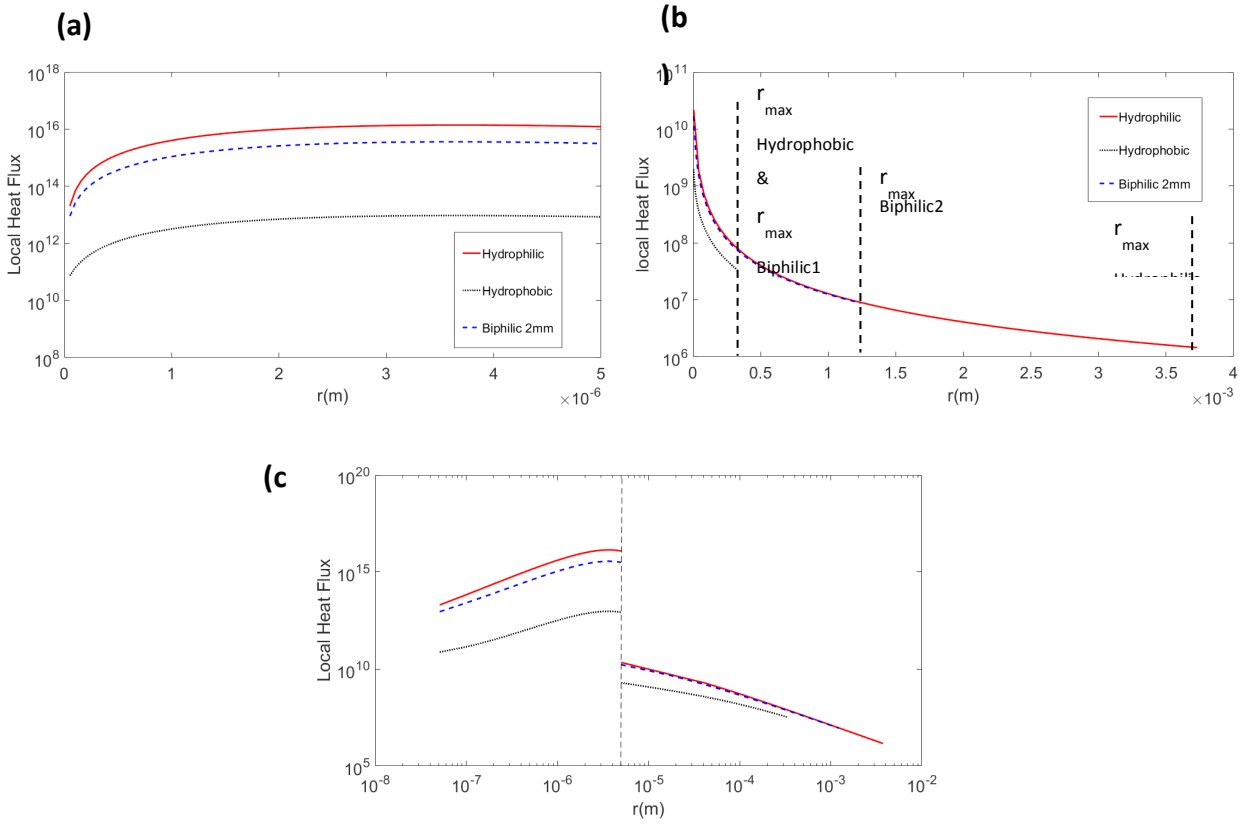

Figure 26. The steady-state single droplet condensation heat flux as a function of droplet radius for hydrophilic, hydrophobic, and 2mm biphilic substrates. (a) The heat flux is shown for small droplets formed by direct condensation. (b) The heat flux is shown for large droplets formed by coalescence. The fall-off radii are shown for each substrate. The biphilic surface has two separate fall-off radii corresponding to the hydrophobic sites and hydrophilic base marked as biphilic1 and biphilic2 respectively. (c) The log-log graph

of combined heat flux for all droplets from initial nucleation to fall-off. The dashed line shows the borderline between small droplets and large droplets. The associated model parameters are: T_{sat} = 20°C, T_w = -10°C, δ_{coat} = 1μm, k_{coat} = 0.15 W/m.K, γ = 2mm, hydrophobic θ_a and θ_r are 150° and 144°, and hydrophilic θ_a and θ_r are 73° and 34°.

The overall heat transfer rate is calculated using equation (32) or measuring the area underneath the plot in Figure 26, and based on the results in Table 3, as already predicted, the biphilic surfaces have the highest heat transfer rate compared to all-hydrophobic and all-hydrophilic substrates. It should be noted that although the hydrophobic surfaces have smaller local heat flux compared to the hydrophilic surfaces, their overall heat flux is almost twice as large as that of hydrophilic substrate simply because their fall-off radius is small and drops tend to roll-off of these surface quickly making room for small droplet formation via nucleation with orders-of-magnitude larger local heat flux. The biphilic substrate with *2mm* pattern spacing has the highest overall heat flux making it a good candidate for enhancing high efficiency drop-wise condensation. Another advantage of using biphilic surfaces, as mentioned before, is their ability to be mass-produced. Since the size of the patterns are in millimeters as opposed to nano-scale features on superhydrophobic surfaces, their manufacturing process is scalable and cost-effective; hence applicable to industrial applications.

Table 3. The overall heat flux through the condenser surface for hydrophilic, hydrophobic, and 2mm biphilic substrates.

Substrate	Overall Heat Flux [W/m^2]
Hydrophilic	**4.38×10^5**
Hydrophobic	**7.08×10^5**
Biphilic 2mm	**1.28×10^6**

The analysis performed to this point were based on parttern spacing of *2mm*, which was chosen arbitrarily. To obtain an optimum pattern spacing is essential in designing an efficient thermal system at reasonable manufacturing cost, that is, the smaller pattern size is favorable for heat transfer as it decreases the fall-off radius, but the fabrication technology for small pattern size is limited and highly costly. The overall heat flux is calculated and presented in Table 4 for surfaces of different pattern spacings. As shown, for surfaces of pattern spacing higher than 4*mm*, the biphilic substrate loses its advantage as the overall heat flux drops below the all-hydrophobic surface heat flux. Therefore, there exists an upper boundary to how large the pattern spacing can be, while to determine the lower boundary or a definite optimum, a comprehensive cost analysis is necessary which is part of the future work for this study.

Table 4. The overall heat flux through the condenser surface for 2mm, 3mm, 4mm, 5mm, and 6mm biphilic substrates. The overall heat flux decreases as the pattern spacing size increases. For biphilic surfaces of pattern spacing of 5mm and higher, the overall heat flux drops below the associated value for all-hydrophobic surface.

Substrate	Overall Heat Flux [W/m^2K]
Biphilic 2mm	**1.28×10^6**
Biphilic 3mm	**8.98×10^5**
Biphilic 4mm	**7.26×10^5**
Biphilic 5mm	**6.08×10^5 < Hydrophobic**
Biphilic 6mm	**5.71×10^5 < Hydrophobic**

4.1.5. Material and Method

The experimental setup consists of three main components, the condenser, the cooling module, and an environmental chamber. The condensing surface was attached vertically, using thermally conductive paste, to a cooling module, which consists of a series of Peltier plates and a temperature controller unit. The sample surface temperature was recorded by thermocouples. The vapor generation system was an automatic humidifier with controlled humidity. Finally, a high-speed camera was used to capture real-time videos of the experiments for further image analysis. All experiments were performed inside the environmental chamber to regulate and maintain consistent humidity and temperature at 80% relative humidity and 20°C saturated temperature. The chamber has a vent to atmosphere to mitigate the buildup of pressure and therefore inaccurate humidity measurements.

Three different samples, hydrophilic, biphilic, and hydrophobic, are placed on the same substrate for comparison. All substrates are made of aluminum with thermal conductivity of $205 W/K.m$. The hydrophobicity, however, is achieved by spraying the WX2100^{TM} spray on the aluminum substrate everywhere on the surface for all-hydrophobic surface and on precisely positioned patterns for biphilic surface. The dynamic and equilibrium contact angles on each of these substrates are measured using Krüss DSA 100 machine. The DSA 100 is equipped with high-resolution camera and a controlled dispensing system that allows measuring the contact angles with precision. The advancing and receding contact angles on the hydrophobic and hydrophilic sites are $\theta_a = 150°$, $\theta_r = 144°$, $\theta_a = 73°$, and $\theta_r = 34°$ respectively.

4.1.6. Experimental Results and Discussion

Experiments are performed to compare the condensation heat transfer efficiency of biphilic surfaces to all-hydrophobic and all-hydrophilic substrates and to test our analytical predictions of the condensation behavior of the biphilic surfaces. To qualitatively assess the efficiency of condensation, five important factors, corresponding to condensation sub-processes, should be considered namely, nucleation, the droplet growth rate, coalescence, the droplet removal rate, and finally renucleation. Figure 27 shows images of condensation experiment on a sample at -10°C for hydrophobic, 2*mm*-biphilic, and hydrophilic substrates. These images are taken every 15 mins during the experiment. Initially, the condensate starts forming on the hydrophilic sites on both biphilic and hydrophilic substrates. Droplets on biphilic substrate grow and merge at a quicker rate compared to the hydrophilic and hydrophobic substrates. The wettability contrast on the biphilic substrate appears to decrease the maximum droplet size, which leads to faster droplet removal and renucleation, the key components in efficient drop-wise condensation. The condensation experiments are repeated for samples at -5°C, -10°C, and -15°C for all of which the biphilic substrate shows better condensation efficiency. It can be seen that the drops tend to form, grow, and fall rapidly on biphilic substrate with no sign of liquid film formation. On hydrophobic substrates, although the number densities are visually higher than the other substrates, the slow droplet coalescence and departure limit their performance and cause ice formation in some cases. The reason of reducing the substrate temperature below the freezing point, while below-dew point would be sufficient, is to increase the condensation rate, which would be consistent with the case for pure vapor condensation. Because this work does not evaluate heat transfer quantities, the effect of latent heat of fusion effect does not affect droplet dynamic.

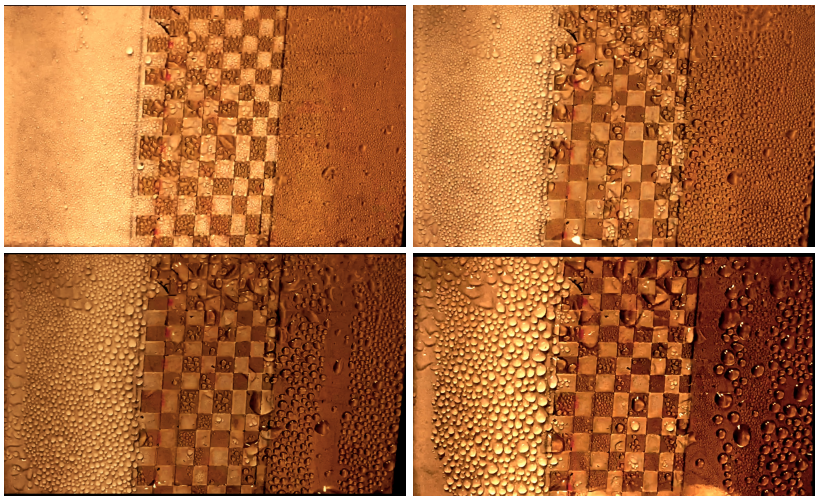

Figure 27. The comparison of time evolution of condensation process on hydrophobic (left), 2mm biphilic (center), and hydrophilic (right) regions. The images are taken every 15 mins. The biphilic substrate shows better droplet nucleation and removal throughout the experiment. The experimental parameters are: T_{sat} = 20°C, T_w = -10°C, humidity = 80%RH, γ = 2mm, hydrophobic θ_a and θ_r are 150° and 144°, and hydrophilic θ_a and θ_r are 73° and 34°.

4.1.7. Conclusion

The previously established mathematical model for drop-wise condensation was modified to study the heat transfer performance of textured surfaces with high wettability contrast, biphilic surfaces, compared to hydrophilic and hydrophobic surfaces. The analytical model predictions show that the biphilic surfaces of pattern spacing below 5mms can achieve a higher drop-wise condensation heat transfer rate *via* continuous droplet nucleation and consistent and controlled droplet removal. The experimental results also verify the advantage of using biphilic structures over the conventional hydrophilic or hydrophobic surfaces. However, there are still challenges and unknown aspects to this technology; hence room for improvements and future study. For instance, the sustainability of the hydrophobic promoter should be studied by calculating the wall-shear stress to assess whether or not these substrates can withstand long-term continuous

droplet formation and removal. In addition, the shape and size of the wettability patterns, as mentioned before, need to be optimized for both manufacturing and thermal transfer purposes.

5. Conclusion

This thesis aimed to study the physics behind the phase transformation phenomena and the dominant factors involved in these processes. We started by studying the delay in the onset of solidification in order to find an optimum icephobic surface. We examined penguins in their natural habitat and were inspired by their unique ice-resisting abilities. We investigated the anti-icing properties of penguin feathers both experimentally and theoretically. Through our investigations, we realized that the anti-icing abilities of penguins is largely due to the micro- and nano-porous surface features of their feathers and the low critical surface tension of the preening oil covering them. The results of our freezing experiments reveal that not only are cold-weather penguins more hydrophobic and have higher water contact-angle, but also they have the ability to delay the solidification initiation time two times more compared to warm-weather penguins. Finally, our scaling analysis results confirm that inception of freezing depends largely on droplet contact-angle, and the geometrical factor that confines the heat flow on high contact-angle droplets is the most dominant factor contributing to icephobicity.

We also expanded our nature-inspired icephobicity study to plant leaves, and explored and compared the ice-resisting abilities of different plant leaves through characterizing their icing criteria. Our comprehensive experimental study showed that the onset of freezing was delayed considerably for a water droplet on the Kale leaf compared to Lettuce leaf, and the anti-icing properties of the winter plant, Kale, were shown to be largely due to the surface microstructure, low nucleation rate, and large contact angle.

Thus, there exists a possibility to design a coating that can resist icing even in the extreme cold by increasing the hydrophobicity of the surface of the exposed structures, which is of a wide range of applications.

After understanding the factors involved in the solidification initiation, we have looked at the dynamics of solidification and non-isothermal spreading. Our main objective was to find a stable non-isothermal spreading regime that allows us to entirely control and predict the footprint after solidification is complete, which is applicable to many areas of industry for such as 3D printing. For that, we focused our attention to understanding the solidification dynamics for impinging droplets with moderate impact velocities, where the impact velocities are high enough that the impact-induced forces play an important role in droplet spreading, but no fingerings and/or break-ups occur. Our scaling analysis showed that for this dynamic regime, the arrest radius of drop only depends on fluid and surface properties and initial volume of droplet and is therefore independent of initial impact velocity and temperature difference between solid substrate and droplet. The experimental results also verified this hypothesis and showed that for moderate impact velocity experiments and small arrested contact angles (less than 90°), the final arrest radius is independent of *We*, *Ste*, and other initial conditions. Therefore, the effect of solidification on the spreading dynamics in this region is very important as it limits the spreading to a certain arrest radius that cannot be altered by merely changing the impact velocities and temperature gradients.

Finally, the last chapter is dedicated to studying condensation and finding scalable and cost-effective ways to enhance heat transfer efficiency for industrial condensations that operate at large scale. We employed a mathematical model for drop-wise condensation and expanded and modified this model to analyze heat removal capabilities of biphilic surfaces with high

wettability contrast patterns. Contrary to previous biphilic surfaces with nano-structures, the patterns on our biphilic surfaces are within a few millimeters, therefore, they can be easily mass-produced. The heat flux and drop number densities are calculated and compared for biphilic surfaces to all-hydrophilic and all-hydrophobic surfaces. The results revealed that biphilic surfaces achieved a higher drop-wise condensation heat transfer rate *via* continuous droplet nucleation and consistent and controlled droplet removal. Our experimental results also verified the high droplet mobility and heat transfer efficiency of biphilic structures over the conventional hydrophilic or hydrophobic surfaces. However, there are still challenges and unknown aspects to this technology; hence room for improvements and future study.

6. References

1 Schiaffino, S. & Sonin, A. A. On the theory for the arrest of an advancing molten contact line on a cold solid of the same material. *Physics of Fluids* **9**, 2227-2233, doi:10.1063/1.869345 (1997).

2 Schiaffino, S. & Sonin, A. A. Motion and arrest of a molten contact line on a cold surface: An experimental study. *Physics of Fluids* **9**, 2217-2226, doi:10.1063/1.869344 (1997).

3 Cooper, W. A., Sand, W. R., Veal, D. L. & Politovich, M. K. Effects of Icing on Performance of a research airplane. *Journal of Aircraft* **21**, 708-715 (1984).

4 Geer, W. C. An Analysis of the Problem of Ice on Airplanes. *Journal of the Aeronautical Sciences* **6**, 451-459 (1939).

5 Attinger, D. *et al.* Surface engineering for phase change heat transfer. *MRS Energy & Sustainability* **1** (2014).

6 Tyshenko, M. G., Doucet, D., Davies, P. L. & Walker, V. K. The Antifreeze Potential of the Spruce Budroom Thermal Hysteresis Protein. *Nature* **15**, 887-890 (1997).

7 Jiang, L., Zhao, Y. & Zhai, J. A Lotus-Leaf-like Superhydrophobic Surface: A Porous Microsphere/Nanofiber Composite Film Prepared by Electrohydrodynamics. *Angewandite Chemie International edition* **43**, 4338-4341 (2004).

8 Lin, J. *et al.* Fabrication of biomimetic superhydrophobic surfaces inspired by lotus leaf and silver ragwort leaf. *Nanoscale* **3**, 1258-1262 (2011).

9 Mei, H. *et al.* Multi-level micro-/nanostructures of butterfly wings adapt at low temperature to water repellency. *Soft Matter* **7**, 10569-10573 (2011).

10 Koch, K., Bhushan, B. & Barthlott, W. Multifunctional Surface Structures of Plants: An Inspiration for Biomimetics. *Progress in Material Science* **54**, 137-178 (2009).

11 Feng, L. *et al.* Petal Effect: A Superhydrophobic State with High Adhesive Force. *Langmuir* **24**, 4114-4119 (2008).

12 Sun, M., Watson, G. S., Zheng, Y., Watson, J. A. & Liang, A. Wetting properties on nanostructured surfaces of cicada wings. *Journal of Experimental Biology* **212**, 3148-3155, doi:10.1242/jeb.033373 (2009).

13 Liu, K., Du, J., Wu, J. & Jiang, L. Superhydrophobic gecko feet with high adhesive forces towards water and their bio-inspired materials. *Nanoscale* **4**, 768-772, doi:10.1039/C1NR11369K (2012).

14 Le Maho, Y., Delclitte, P. & Chatonnet, J. Thermoregulation in fasting emperor penguins. *Am. J. Physiol* **231**, 913-922 (1976).

15 Jacob, J. Uropygial gland lipids of penguins. *Biochemical Syst Ecol* **4**, 209-213, doi:10.1016/0305-1978(76)90040-5 (1976).

16 Gent, R. W., Dart, N. P. & Cansdale, J. T. Aircraft icing. *Phil. Trans. R. Soc. A* **358**, 2873-2911 (2000).

17 Agency, E. P. Effluent limitation guidelines and new source performance standards for the airport deicing category. (2012).

18 Jasinski, W. J., Noe, S. C., Selig, M. C. & Bragg, M. B. Wind Turbine Performance under Icing Conditions. *Trans ASME J Sol Energy Eng,* **120**, 60-65 (1998).

19 Carriveau, R., Edrisy, A. & Cadieux, P. Ice adhesion issues in renewable energy infrastructure. . *J. Adhes. Sci. Technol.* **26**, 37-41 (2012).

20 Dalili, N., Edrisy, A. & Carriveau, R. A Review of Surface Engineering Issues Critical to Wind Turbine Performance. *Renewable and Sustainable Energy Reviews* **13**, 428-438 (2007).

21 Machielsen, C. H. M. & Kerschbaumer, H. G. I. Influence of frost formation and defrosting on the performance of air coolers: standards and dimensionless coefficients for the system designer. *Int. J. Refrig.* **12**, 283-290 (1989).

22 He, M. *et al.* Superhydrophobic film retards frost formation. *Soft Matter* **6**, 2396-2399 (2010).

23 He, M., Wang, J. J., Li, H. L. & Song, Y. L. Superhydrophobic surfaces to condensed micro droplets at temperatures below the freezing point retard ice/frost formation. *Soft Matter* **7**, 3993-4000 (2011).

24 Cao, L. L., Jones, A. K., Sikka, V. K., Wu, J. Z. & Gao, D. Anti-icing superhydrophobic coating. *Langmuir* **25**, 12444-12448 (2009).

25 Meuler, A. J., Mckinley, G. H. & Cohen, R. E. Exploiting topographical texture to impart icephobicity. *ACS Nano* **4**, 7048-7052 (2010).

26 Mishchenko, L. *et al.* Design of ice-free nanostructured surfaces based on repulsion of impacting water droplets. *ACS Nano* **4**, 7699-7707 (2010).

27 Lv, J., Song, Y., Jiang, L. & Wang, J. Bio-inspired strategies for anti-icing. *ACS Nano* **8**, 3152-3169 (2014).

28 Law, K. & Zhao, H. *Surface Wetting: Characterization, Contact Angle, and Fundamentals*. (Springer, 2016).

29 Anderson, D. M., Worster, M. G. & Davis, S. H. The Case for a Dynamic Contact Angle in Containerless Solidification. *Journal of Crystal Growth* **163**, 329-228 (1996).

30 Robertson, J., Harkin, C. & Govan, J. the Identification of Bird Feathers. Scheme for Feather Examination. *journal of the Forensic Science Society* **24**, 85-89 (1984).

31 Du, N., Fan, J., Wu, H., Chen, S. & Liu, Y. An improved model of heat transfer through penguin feathers and down. *Journal of Theoretical Biology* **248**, 727-735 (2007).

32 Bormashenko, E., Bormashenko, Y., Stein, T., Whyman, G. & Bormashenko, E. Why do pigeon feathers repel water? Hydrophobicity of pennae, Cassie-Baxter wetting hypothesis and Cassie-Wenzel capillarity-induced wetting transition. *Journal of Colloid and Interface Schience* **311**, 212-216 (2007).

33 Bormashenko, E., Gendelman, O. & Whyman, G. Superhydrophobicity of Lotus Leaves versus Birds Wings: Different Physical Mechanisms Leading to Similar Phenomena. *Langmuir* **28**, 14992-14997 (2012).

34 Wang, S. *et al.* Icephobicity of Penguins Spheniscus Humboldti and an Artificial Replica of Penguin Feather with Air-Infused Hierarchical Rough Structures. *American Chemical Society* (2016).

35 Kamath, Y. K., Dansizer, C. J. & Weigmann, H. D. Wettability of keratin fiber surfaces. *Society of Cosmetic Chemists* **28**, 273-284 (1977).

36 Srinivasan, S. *et al.* Quantification of Feather Structure, Wettability and Resistance to Liquid Penetration. *Journal of The Royal Society Interface* **11** (2014).

37 Reneerkens, J. *Functional aspects of seasonal variation in preen wax composition of sandpipers* PhD thesis, University of Groningen, (2007).

38 Jacob, J. Uropygial gland lipids of penguins. *Biochemical Syst Ecol* **4**, 209-213, doi:10.1016/0305-1978 (1976).

39 Rothstein, J. P. Slip on Superhydrophobic Surfaces. *Annual Review of Fluid Mechanics* **42**, 89-109 (2010).

40 de Gennes, P.-G., Brochard-Wyart, F. & Quere, D. *Capillary and Wetting Phenomena: Drops, Bubbles, Pearls, Waves*. (Springer New York, 2004).

41 Li, K. Y. *et al.* Investigating the Effects of Solid Surfaces on Ice Nucleation. *Langmuir* **28**, 10749-10754, doi:10.1021/la3014915 (2012).

42 Jung, S. *et al.* Are Superhydrophobic Surfaces Best for Icephobicity? *Langmuir* **27**, 3059-3066, doi:10.1021/la104762g (2011).

43 Alizadeh-Birjandi, E. & Kavehpour, H. P. Plant leaves icephobicity. *J. Coat. Technol. Res.* **14**, 1061-1067 (2017).

44 Schutzius, T. M. *et al.* Physics of Icing and Rational Design of Surfaces with Extraordinary Icephobicity. *Langmuir* **31**, 4807-4821 (2015).

45 Maitra, T. *et al.* Supercooled Water Drops Impacting Superhydrophobic Textures. *Langmuir* **30**, 10855-10861 (2014).

46 Sun, X., Damle, , V. G., L., S. & Rykaczewski, K. Bioinspired stimuli-responsive and antifreeze-secreting anti-icing coatings. *Adv. Mater. Interfaces* **2** (2015).

47 Pengfei Hao, Lv, C. & Zhang, X. Freezing of sessile water droplets on surfaces with various roughness and wettability. *applied Physical Letter* **104** (2014).

48 He, M., Li, H., Wang, J. & Song, Y. Superhydrophobic surface at low surface temperature. *applied Physical Letter* **98** (2011).

49 HaiFeng Zhang, Y. Z., Rong Lv, Chun Yang. Freezing of sessile water droplet for various contact angles. *International Journal of Thermal Sciences* **202**, 59-67 (2016).

50 Tourkine, P., Le Merrer, M. & Quere, D. Delayed Freezing on Water Repellent Materials. *Langmuir* **25**, 7214-7216, doi:10.1021/la900929u (2009).

51 Alizadeh, A. *et al.* Dynamics of Ice Nucleation on Water Repellent Surfaces. *Langmuir* **28**, 3180-3186, doi:10.1021/la2045256 (2012).

52 Anderson, D. M. & Davis, S. H. Local Fluid and Heat Flow Near Contact Lines. *J. Fluid Mech.268*, 34 (1994).

53 Mills, A., F.;. *Heat Transfer*. (CRC Press, 1992).

54 Levitt, J. Responses of Plants to Environmental Stresses. *Academic Press, New York*, 87-90 (1980).

55 Alizadeh-Birjandi, E. *et al.* Delay of Ice Formation on Penguin Feathers (Under Review). *Nature Physics* (2017).

56 Engemann, S. *et al.* Interfacial Melting of Ice in Contact with SiO2. *Physical Review Letter* **92** (2004).

57 Kulinich, S. A. & Farzaneh, M. How Wetting Hysteresis Influences Ice Adhesion Strength on Superhydrophobic Surfaces. *Langmuir* **25**, 8854–8856 (2009).

58 Dodiuk, H., Kenig, S. & Dotan, A. Do Self-cleaning Surfaces Repel Ice? *Journal of Adhesion science and technology* **26**, 701-714 (2012).

59 Eberle, P., Tiwari, M. K., Maitra, T. & Poulikakos, D. Rational nanostructuring of surfaces for extraordinary icephobicity. *Nanoscale* **6**, 4874-4881 (2014).

60 International, t. E. P. *Kale*, <<http://home.howstuffworks.com/kale.htm> > (2007).

61 Britannica, T. E. o. E. *Kale*, <https://www.britannica.com/plant/kale> (2016).

62 The Columbia Encyclopedia, t. e. *Kale*, <http://www.encyclopedia.com/reference/encyclopedias-almanacs-transcripts-and-maps/kale> (

63 Culture, E. o. F. a. *Lettuce*, <http://www.encyclopedia.com/food/encyclopedias-almanacs-transcripts-and-maps/lettuce> (

64 Britannica, T. E. o. E. *Lettuce*, <https://www.britannica.com/plant/lettuce> (2009).

65 International, t. E. o. P. *Lettuce*, <<http://home.howstuffworks.com/lettuce.htm> > (2007).

66 Haferl, S. & Poulikakos, D. Experimental investigation of the transient impact fluid dynamics and solidification of a molten microdroplet pile-up. *Int. J. Heat Mass Transfer* **46**, 535-550 (2003).

67 Le Bot, C., Vincent, S. & Arquis, E. Impact and solidification of indium droplets on a cold substrate. *Int. J. Therm. Sci* **44**, 219-233 (2005).

68 Attinger, D. & Poulikakos, D. Melting and resolidification of a substrate caused by molten microdroplet impact. *Trans. ASME, J. Heat Transfer* **123**, 1110-1122 (2001).

69 Haferl. S *et al.* Freezing dynamics of molten solder droplets impacting onto flat substrates in reduced gravity. *Int. J. Heat Mass Transfer*, 3513-3528 (2001).

70 Gong, S. C. Spreading of droplets impacting on smooth solid surface. *Japan. J. Appl. Phys.* **44**, 3323-3324 (2005).

71 Li, R., Ashgriz, N. & Chandra, S. Maximum spread of droplet on solid surface: low Reynolds and Weber numbers. *Int. J. therm. Sci* **132** (2010).

72 Luo, J. L., Qi, L. H., Zhong, S. Y., Zhou, J. M. & J., L. H. Printing solder droplets for micro devices packages using pneumatic drop-on-demand (DOD) technique. *J. Mater. Process. Technol.* **212**, 2066-2073 (2012).

73 Wu, J., Wei, Z. Y., Chen, Z., Li, S. L. & Tang, Y. P. Numerical investigation of pile up process in metal microdroplet deposition manufacture. *Micromachines* **5**, 1429-1444 (2014).

74 Chandra, S. & Avedisian, C. T. On the collision of a droplet with a solid surface. *Proc. R. Soc. Lond. A* **432**, 13-41 (1991).

75 Madejski, J. Solidification of Droplets on a Cold Surface. *International Journal of Heat and Mass Transfer* **19**, 1009-1013, doi:10.1016/0017-9310(76)90183-6 (1976).

76 Collings, E. W., Markworth, A. J., McCoy, J. K. & Saunders, J. H. Splat-quench solidification of freely falling liquid-metal drops by impact on a planar substrate. *J. Mater. Sci.* **25**, 3677-3682 (1990).

77 Watanabe, T., Kuribayashi, I., Honda, T. & Kanzawa, A. DEFORMATION AND SOLIDIFICATION OF A DROPLET ON A COLD SUBSTRATE. *Chemical Engineering Science* **47**, 3059-3065, doi:10.1016/0009-2509(92)87006-c (1992).

78 Pasandideh-Fard, M., Chandra, S. & Mostaghimi, J. A three-dimensional model of droplet impact and solidification. *Int. J. Heat Mass Transfer* **45**, 2229-2242 (2002).

79 Engel, O. G. Waterdrop Collisions with Solid Surfaces. *Journal of Research of the National Bureau of Standards* **54**, 17 (1955).

80 Levin, Z. & Hobbs, P. V. Splashing of Water Drops on Solid and Wetted Surfaces: Hydrodynamic and Charge Separation. *Phil. Trans. Roy. Soc. London* **269**, 30 (1971).

81 Loeher, K. F. & Lasek, A. Splashing of Drops *Arch. Mech. Warszawa* **42**, 6 (1990).

82 Rein, M. Phenomena of Liquid Drop Impact on Solid and Liquid Surfaces. *Fluid Dynamic Research* **12**, 22 (1993).

83 Elliot, T. A. & Ford, D. M. dynamic Contact Angles. *Chemical Society Journal, Faraday Transactions I* **68**, 9 (1972).

84 Stow, C. D. & Hadfield, M. G. An Experimental Investigation of fluid Flow Resulting from the Impact of a Water Drop with an Unyelding Dry Surface. *Proc. Roy. Soc. London A* **373**, 22 (1980).

85 Schiaffino, S. & Sonin, A. A. Molten Droplet Deposition and Solidification at Low Weber Numbers. *Phys. Fluids* **9**, 3172-3187, doi:10.1063/1.869434 (1997).

86 Tanner, L. H. SPREADING OF SILICONE OIL DROPS ON HORIZONTAL SURFACES. *Journal of Physics D-Applied Physics* **12**, 1473-&, doi:10.1088/0022-3727/12/9/009 (1979).

87 Hoffman, R. L. STUDY OF ADVANCING INTERFACE .1. INTERFACE SHAPE IN LIQUID-GAS SYSTEMS. *Journal of Colloid and Interface Science* **50**, 228-241, doi:10.1016/0021-9797(75)90225-8 (1975).

88 Bhola, R. & Chandra, S. Parameters controlling solidification of molten wax droplets falling on a solid surface. *Journal of Materials Science* **34**, 4883-4894, doi:10.1023/a:1004680315199 (1999).

89 Shiraz, D. A. & Chandra, S. Impact, recoil and splashing of molten metal droplets. *Int. J. Heat Mass Transfer* **43**, 2841-2857 (2000).

90 Tavakoli, F., Davis, S. H. & Kavehpour, H. P. Spreading and Arrest of a Molten Liquid on Cold Substrates. *Langmuir* **30**, 10151-10155 (2014).

91 Bejan, A. & Gobin, D. Constructal theory of droplet impact geometry. *International Journal of Heat and Mass Transfer* **49**, 2412-2419 (2006).

92 Clanet, C., Beguin, C., Richard, D. & Quere, D. Maximal deformation of an impacting drop. *J. Fluid Mech.* **517**, 199-208 (2004).

93 Ruiter, R. D., P., C., Brunet, P., H., S. J. & Gelderblom, H. Contact line arrest in solidifying spreading drops. *Physical Review Fluid* **2** (2017).

94 Bennett, T. & Poulikakos, D. Splat-quench solidification: estimating the maximum spreading of a droplet impacting a solid surface *Journal of Material Science* **28**, 963-970 (1993).

95 Dhiman, R. & Chandra, S. Freezing-induced splashing during impact of molten metal droplets with high Weber numbers. *Int. J. Heat Mass Transfer* **48**, 5625-5638 (2005).

96 Stefan, J. Uber einige Probleme der Theorie der Warmeleitung. *S B Wien Akad. Mat. Natur.*, 473-484 (1889).

97 Clyne, T. W. Numerical Treatment of Rapid Solidification. *Metall. Trans. B* **15**, 369-381 (1984).

98 Dykhuizen, R. C. Review of impact and solidification of molten thermal spray droplets. *Journal of Thermal Spray Technology* **3**, 351-361 (1994).

99 Rose, J. W. Dropwise condensation theory and experiment: A review . *Proceedings of the Institution of Mechanical Engineers, Part A: Journal of Power and Energy* **216**, 115-128 (2002).

100 Schmidt, E., Schurig, W. & Sellschopp, W. Versuche über die Kondensation von Wasserdampf in Film- und Tropfenform. *Technische Mechanik und Thermodynamik* **1**, 53-63 (1930).

101 Song, Y., Xu, D., Lin, J. & Tsian, S. A study on the mechanism of dropwise condensation. *International Journal of Heat and Mass Transfer* **34**, 2827-2831 (1991).

102 Rose, J. W. Condensation Heat Transfer Fundamentals. *Chemical Engineering Research and Design* **76**, 143-152 (1998).

103 Leach, R. N., Stevens, F., Langford, S. C. & Dickinson, J. T. Dropwise Condensation: Experiments and Simulations of Nucleation and Growth of Water Drops in a Cooling System. *Langmuir* **22**, 8864-8872 (2006).

104 Paxson, A. T., Yagüe, J. L., Gleason, K. K. & Varanasi, K. K. Stable Dropwise Condensation for Enhancing Heat Transfer via the Initiated Chemical Vapor Deposition (iCVD) of Grafted Polymer Films. *Advance Materials* **26**, 418-423 (2014).

105 Miljkovic, N. *et al.* Jumping-Droplet-Enhanced Condensation on Scalable Superhydrophobic Nanostructured Surfaces. *Nano Letter* **13**, 179-187 (2012).

106 Xiao, R., Miljkovic, N., Enright, R. & Wang, E. N. Immersion Condensation on Oil-Infused Heterogeneous Surfaces for Enhanced Heat Transfer. *Scienific Report* **3**, 1988 (2013).

107 Welch, J. & Westwater, J. W. Microscopic Study of Dropwise Condensation,. *ASME International Developments in Heat Transfer,* **2**, 302-309 (1961).

108 Le Fevre, E. J. & Rose, J. W. Heat-Transfer Measurements During Dropwise Condensation of Steam,. *Int. J. Heat Mass Transfer* **7**, 272-273 (1964).

109 Kandlikar, S. G., Shoji, M. & Dhir, V. K. *Handbook of Phase Change: Boiling and Condensation* (1999).

110 Ma, X., Rose, J. W., Xu, D., Lin, J. & Wang, B. Advances in Dropwise Condensation Heat Transfer: Chinese Research,. *Chem. Eng. J.* **78**, 87-93 (2000).

111 Kim, S. & Kim, K. J. Dropwise Condensation Modeling Suitable for Superhydrophobic Surfaces. *ASME Journal of Heat Transfer* **133** (2011).

112 Carey, V. P. Liquid-vapor phase-change phenomena. *Hemisphere Publishing Corporation*, 413-472 (1992).

113 A. K. Das, H. P. Kilty, P. J. Marto, G. B. Andeen & A. Kumar. The Use of an Organic Self-Assembled Monolayer Coating to Promote Dropwise Condensation of Steam on Horizontal Tubes. *J. Heat Transfer* **122**, 278-286 (1999).

114 K. O. Zamuruyev *et al.* Continuous Droplet Removal upon Dropwise Condensation of Humid Air on a Hydrophobic Micropatterned Surface. *Langmuir* **30**, 10133-10142 (2014).

115 J. R. Lara & M.T. Holtzapple. Experimental investigation of dropwise condensation on hydrophobic heat exchangers. Part II: Effect of coatings and surface geometry. *Desalination* **280**, 363-369 (2011).

116 A. Alizadeh , V. Bahadur , A. Kulkarni, M. Yamada & J. A. Ruud. Hydrophobic surfaces for control and enhancement of water phase transitions *MRS Bulletin* **38**, 407-411 (2013).

117 Xuemei Chen *et al.* Nanograssed Micropyramidal Architectures for Continuous Dropwise Condensation. *Advance Functional Materials* **21**, 4617-4623 (2011).

118 Anderson, D. M. *et al.* Using Amphiphilic Nanostructures to Enable Long-Range Ensemble Coalescence and Surface Rejuvenation in Dropwise Condensation. *ACS Nano* **6**, 3262-3268 (2012).

119 Cheng, J. T., Vandadi, A. & Chen, C. L. Condensation Heat Transfer on Two-Tier Superhydrophobic Surfaces. *Applied Physical Letter* **101** (2012).

120 Lo, C. W., Wang, C. C. & Lu, M. C. Spatial Control of Heterogeneous Nucleation on the Superhydrophobic Nanowire Array. *Advance Functional Materials* **21**, 1211-1217 (2013).

121 Y. Hou, M. Yu, X. Chen, Z. Wang & S. Yao. Recurrent Filmwise and Dropwise Condensation on a Beetle Mimetic Surface. *ACS Nano* **9**, 71-81 (2015).

122 Kumagai, S., Tanaka, S., Katsuda, H., Shimada, R. On the enhancement of filmwise condensation heat transfer by means of the coexistence with dropwise condensation sections. . *Experimental heat transfer an International Journal* **4**, 71-82 (1991).

123 Zou, L., Wang, H., Zhu, X., Ding, Y., Chen, R., & Liao, Q. Droplet splitting on chemically striped surface. *Colloids and Surfaces A: Physicochemical and Engineering Aspects* **537**, 139-148 (2018).

124 Morita, M., Koga, T., Otsuka, H., & Takahara, A. Macroscopic-wetting anisotropy on the line-patterned surface of fluoroalkylsilane monolayers. *Langmuir* **21**, 911-918 (2005).

125 Drelich, J., Wilbur, J. L., Miller, J. D., & Whitesides, G. M. . Contact angles for liquid drops at a model heterogeneous surface consisting of alternating and parallel hydrophobic/hydrophilic strips. . *Langmuir* **12**, 1913-1922 (1996).

126 Raj, R., Enright, R., Zhu, Y., Adera, S., & Wang, E. N. . Unified model for contact angle hysteresis on heterogeneous and superhydrophobic surfaces. *Langmuir* **28**, 15777-15788 (2012).

127 Kita, Y., Mackenzie-Dover, C., Askounis, A., Takata, Y., & Sefiane, K. Drop mobility on superhydrophobic microstructured surfaces with wettability contrasts. *Soft Matter* (2018).

128 R. D. Narhe & D. A. Beysens. Growth Dynamics of Water Drops on a Square-Pattern Rough Hydrophobic Surface. *Langmuir* **23**, 6486-6489 (2007).

129 A. Chatterjee, M. M. Derby, Y.Peles & M. K. Jensen. Condensation heat transfer on patterned surfaces. *Int. J. Heat Mass Transfer* **66**, 889-897 (2013).

130 Leipertz, A. Dropwise condensation. *Stephan P (ed) VDI heat atlas VDI-GVC*, 933-937 (2010).

131 Jakob, M. Heat transfer in evaporation and condensation. *Mech Eng* **58**, 643-660 (1936).

132 McCormic, J. L. & Baer, E. On the mechanism of heat transfer in dropwise condensation. *J Collide Sci* **18**, 208-216 (1963).

133 Eucken, A. Energie- und Stoffaustausch an Grenzflächen. *Die Naturwissenschaften* **25**, 209-218 (1937).

134 Sikarwar, B. S., Khandekar, S. & Muralidhar, K. Mathematical modeling of dropwise condensation on textured surfaces. *Sadhana* **38**, 1135-1171 (2013).

135 Rose, J. W. Further aspects of dropwise condensation theory. *Int. J. Heat Mass Transfer* **19**, 1363-1370 (1976).

136 Khandekar, S. & Muralidhar, K. Dropwise condensation on inclined textured surfaces. *SpringerBriefs in Thermal Engineering and Applied Science* (2014).

137 Liu, X. & Cheng, P. Dropwise condensation theory revisited Part II. Droplet nucleation density and condensation heat flux. *Int. J. Heat Mass Transfer* **83**, 842-849 (2015).

138 N. Miljkovic, R. Enright & E. N. Wang. Modeling and Optimization of Superhydrophobic Condensation. *J. Heat Transfer* **135** (2013).

139 AbuOrabi, M. Modeling of Heat Transfer in Dropwise Condensation. *Int. J. Heat Mass Transfer* **41**, 81-87 (1998).

140 Le Fevre, E. J. & Rose, J. W. A theory of heat transfer by dropwise condensation. *Proc. 3rd international heat transfer conference* **2**, 362-375 (1966).

141 Glicksman, R. L. & Hunt, W. A. Numerical simulation of dropwise condensation. *Int. J. Heat Mass Transfer* **15**, 2251-2269 (1972).

142 P. Dimitrakopoulos & J. Higdon. On the gravitational displacement of three-dimensional fluid droplets from inclined solid surfaces. *J. Fluid Mech.* **395**, 181-209 (1999).

143 W. H. Wu & J. R. Maa. On the heat transfer in dropwise condensation. *Chem. Eng. J.* **12**, 225-231 (1976).

7. Appendix 1 - Gas Chromatography/Mass Spectrometry (GC/MS) Analysis

Gas chromatography/mass spectrometry (GC/MS) is an analytical method that combines the features of gas chromatography and mass spectrometry to quantify and identify different substances in a sample. In the total ion current display (TIC: Y-axis signal intensity; X-axis chromatographic retention time), peak areas of the components are proportional to their abundance in the sample, and the fragmentation pattern of each component (Z-axis) produced when electron impact is the ionization mode, can be used to identify the component.

For penguin feather preen oil composition analysis, weighed samples of feathers (typically 50 mg) were extracted in glass test tubes with chloroform/methanol (2/1 ratio) using vigorous mixing and sonication in a bath ultra-sonicator (30 mins). The samples were then centrifuged and the supernatants were transferred to clean tubes and dried in a vacuum centrifuge. The dried samples were then redissolved and transferred to GC injector vials, and 1 μL aliquots were injected (splitless mode) into a GC injector port (250°C) connected to a bonded-phase medium polarity fused silica capillary column (Thermo Scientific TG-5SILMS, phenyl/dimethylpolysiloxane 5/95, 30 m x 0.25 mm, 0.25 μm film thickness) and eluted (99.999% helium, constant flow at 1 mL/min, Thermo Trace 1310 GC system) over a 63-minute temperature ramp (min/°C; 0'/50, 3'/50, 53'/300, 63'/300). The end of the column (GC/MS transfer line at 250°C) was directly inserted into the EI source (180°C, 70 eV) of an orbitrap mass spectrometer (Thermo Q Exactive GC, calibrated with perfluorotributylamine immediately prior to the analysis of each batch of samples) scanning from m/z 40-650 (0.9 sec/scan at a resolution (FWHM) of 70,000) with a 15 minute solvent delay. Data were collected with instrument manufacturer-supplied software (Thermo Xcalibur).

The analyses were performed to compare the preen oil composition and component relative abundances between two groups of samples, the feathers used in the experiment and feathers freshly collected from the same birds after preening. Simultaneously-prepared blank samples (no feather, only solvent) were also included in the analyses. The TICs from matched Emperor and Gentoo samples and the solvent control are shown in Figure 28 panel (a), and select regions of the chromatograms are shown in panel b-i to display the less-abundant components. The details of the compounds that were identified by spectral matching are presented in Table 5. The results reveal that samples subject to the experiment and control samples have profiles that are comparable, with the intensity of the components in reasonable agreement and easily distinguishable from the blank sample. The difference in the abundances between the experimental samples and control can be justified by the randomness of sample collection and reflects the natural variability between samples.

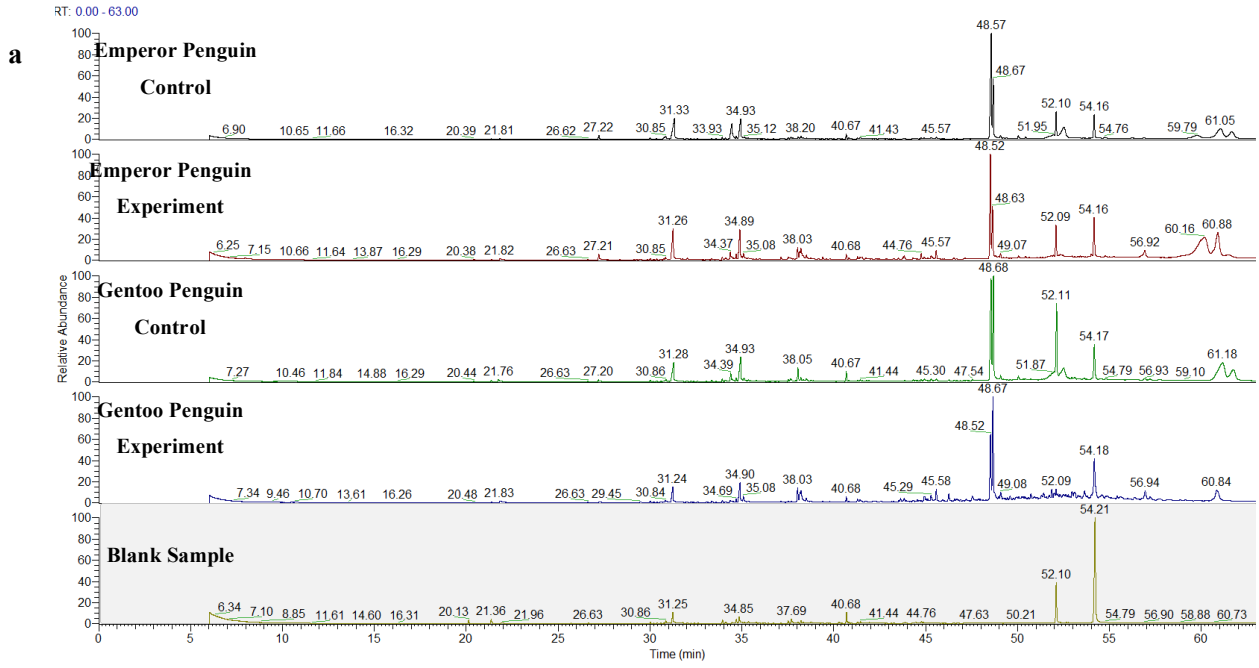

b

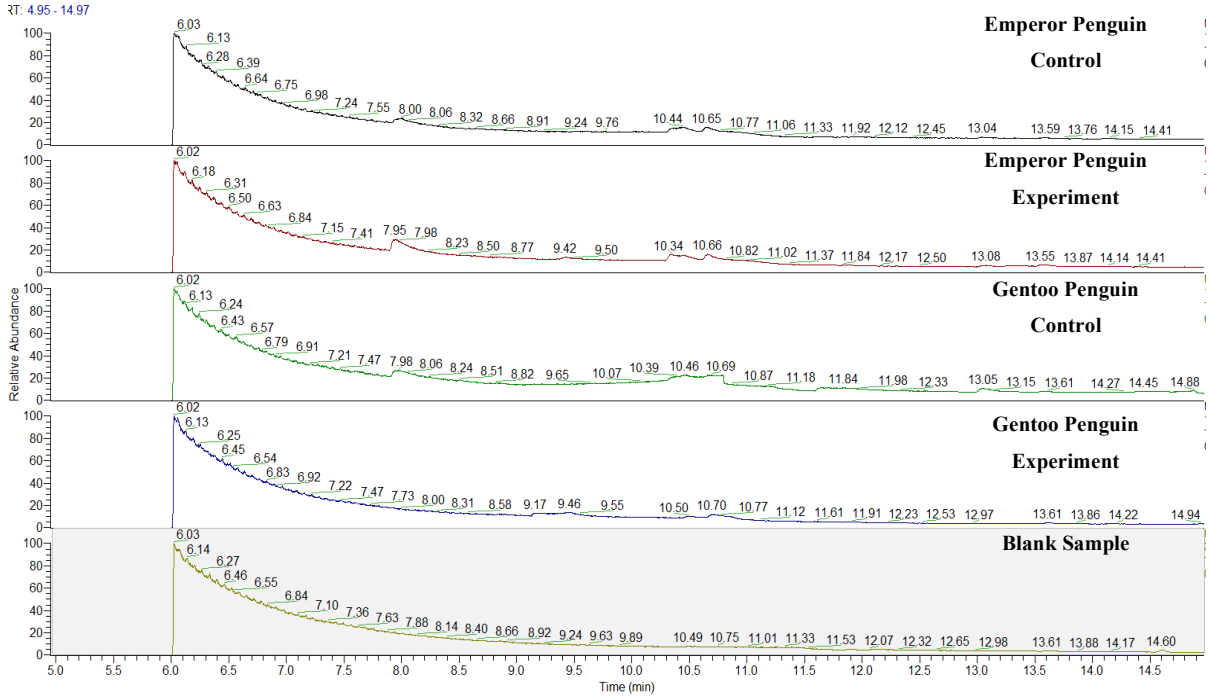
RT: 4.95 - 14.97
Emperor Penguin
Control
Emperor Penguin
Experiment
Gentoo Penguin
Control
Gentoo Penguin
Experiment
Blank Sample
Relative Abundance
Time (min)

c

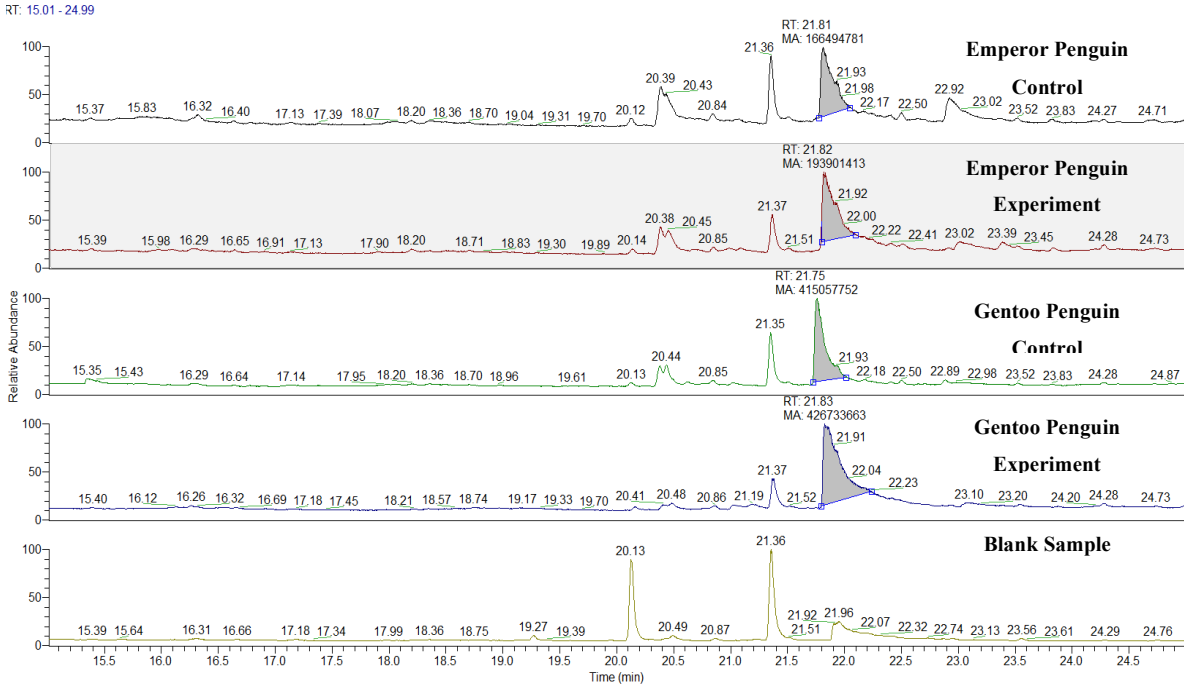
RT: 15.01 - 24.99
RT: 21.81
MA: 166494781
Emperor Penguin
Control
RT: 21.82
MA: 193901413
Emperor Penguin
Experiment
RT: 21.75
MA: 415057752
Gentoo Penguin
Control
RT: 21.83
MA: 426733663
Gentoo Penguin
Experiment
Blank Sample
Relative Abundance
Time (min)

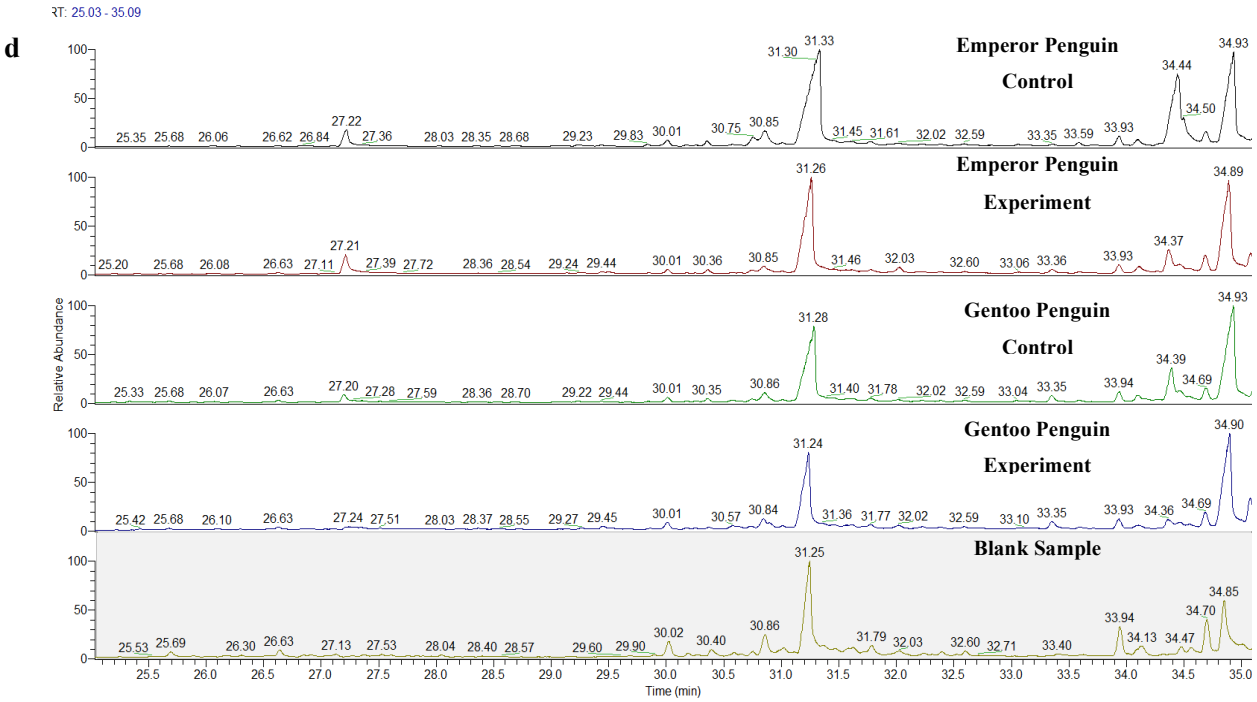
d
RT: 25.03 - 35.09
Emperor Penguin
Control
Emperor Penguin
Experiment
Gentoo Penguin
Control
Gentoo Penguin
Experiment
Blank Sample
Relative Abundance
Time (min)

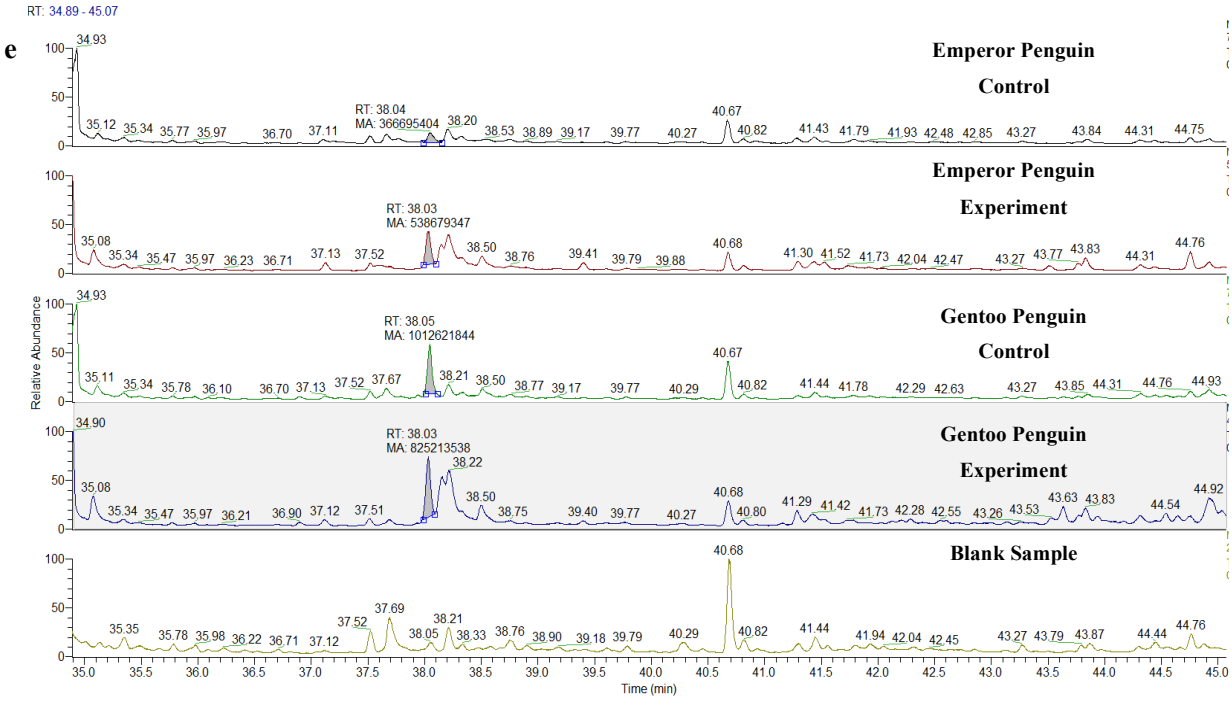
e
RT: 34.89 - 45.07
Emperor Penguin
Control
RT: 38.04
MA: 366695404
Emperor Penguin
Experiment
RT: 38.03
MA: 538679347
Gentoo Penguin
Control
RT: 38.05
MA: 1012621844
Gentoo Penguin
Experiment
RT: 38.03
MA: 825213538
Blank Sample
Relative Abundance
Time (min)

f

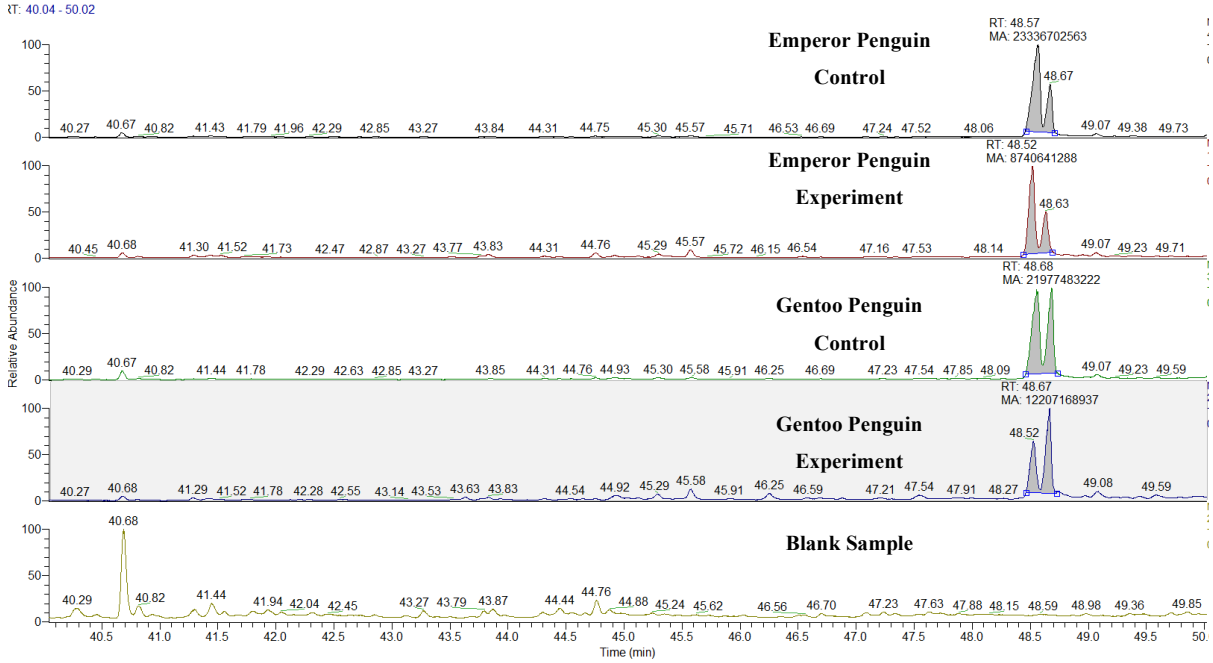
RT: 40.04 - 50.02
Emperor Penguin
Control
RT: 48.57
MA: 23336702563
Emperor Penguin
Experiment
RT: 48.52
MA: 8740641288
Gentoo Penguin
Control
RT: 48.68
MA: 21977483222
Gentoo Penguin
Experiment
RT: 48.67
MA: 12207168937
Blank Sample
Relative Abundance
Time (min)

g

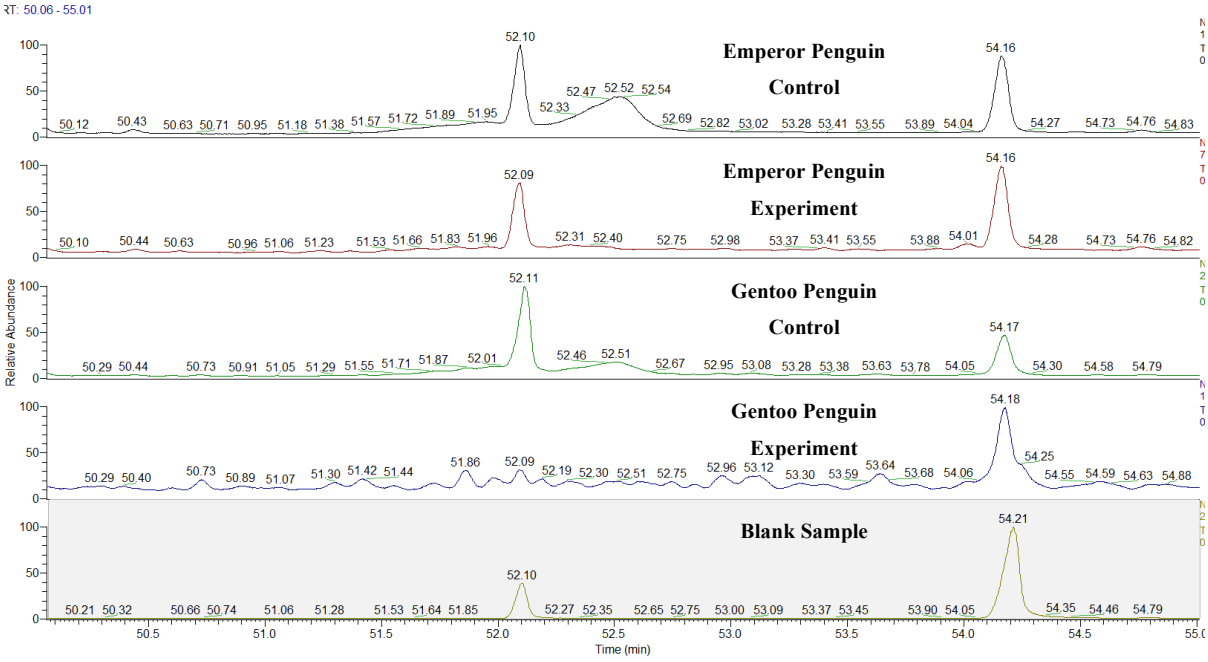
RT: 50.06 - 55.01
Emperor Penguin
Control
Emperor Penguin
Experiment
Gentoo Penguin
Control
Gentoo Penguin
Experiment
Blank Sample
Relative Abundance
Time (min)

h

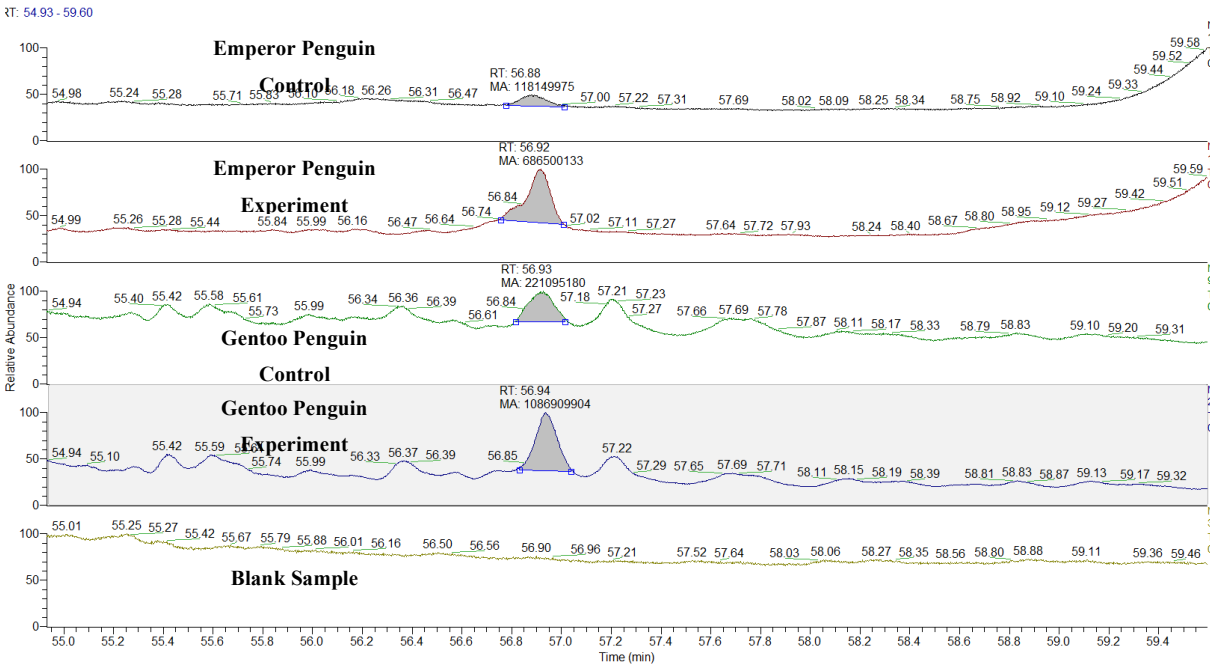
RT: 54.93 - 59.60
Emperor Penguin Control
RT: 56.88
MA: 118149975
Emperor Penguin Experiment
RT: 56.92
MA: 686500133
Gentoo Penguin Control
RT: 56.93
MA: 221095180
Gentoo Penguin Experiment
RT: 56.94
MA: 1086909904
Blank Sample
Relative Abundance
Time (min)

i

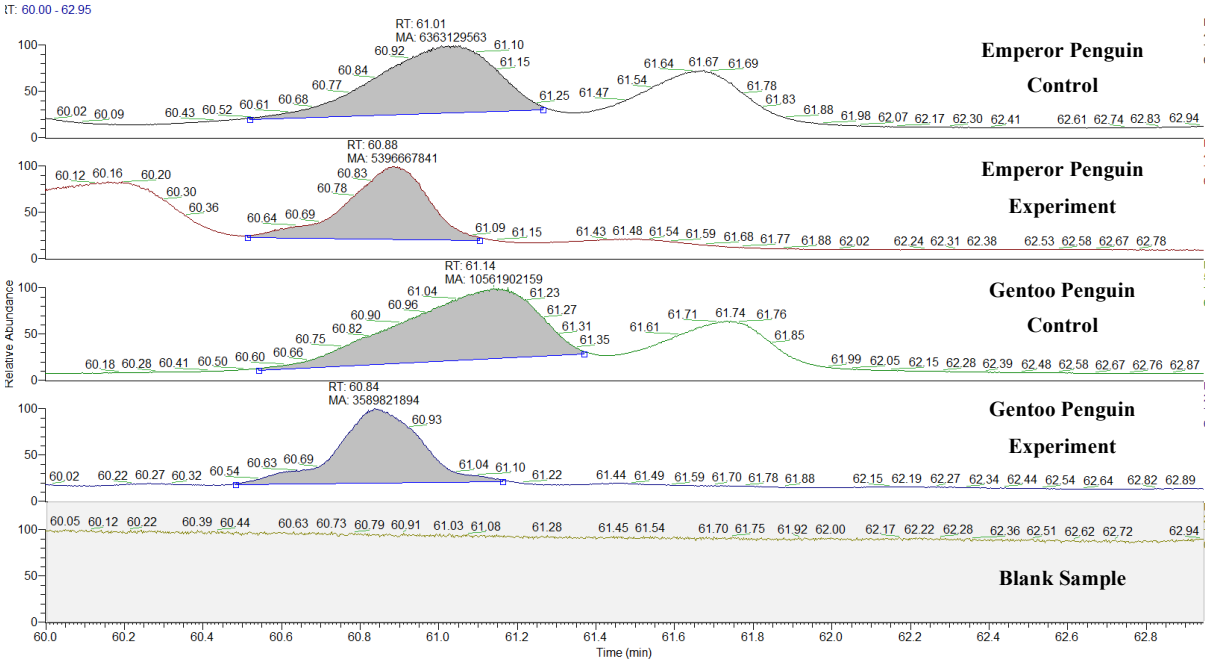
RT: 60.00 - 62.95
Emperor Penguin Control
RT: 61.01
MA: 6363129563
Emperor Penguin Experiment
RT: 60.88
MA: 5396667841
Gentoo Penguin Control
RT: 61.14
MA: 10561902159
Gentoo Penguin Experiment
RT: 60.84
MA: 3589821894
Blank Sample
Relative Abundance
Time (min)

Figure 28. GC/MS TIC profiles of feather extracts. a, the TIC for all five samples (Emperor control, Emperor experiment, Gentoo control, Gentoo experiment, and Blank). Every peak shows a compound and its relative abundance in the sample. In sub-plots b, c, d, e, f, g, h, i, select regions of chromatograms are displayed to reveal the less abundant components.

Table 5. List of compounds identified in the penguin extracts (not present in the blank) by spectral matching, and their relative abundances. Retention times (RT) are compound-specific, and on the system used are reproducible to about 5 seconds (0.083 min). The measured peak areas (MA) from the TIC provide an estimate of the relative abundance of the compound in the sample. As shown below, the compounds identified in the feather extracts are almost the same between samples, and the variation in their abundance is what might be expected naturally between different samples of feathers from the same bird.

Sample	RT	MA	Identity	Formula
G exp	21.83	4.26e8	Benzoic acid	C11H14O3
G cont	21.75	4.15e8	Benzoic acid	C11H14O3
E exp	21.82	1.93e8	Benzoic acid	C11H14O3
E cont	21.81	1.66e8	Benzoic acid	C11H14O3
G exp	38.03	8.25e8	9-Octadecenamide	C18H35NO
G cont	38.05	10.1e8	9-Octadecenamide	C18H35NO
E exp	38.03	5.38e8	9-Octadecenamide	C18H35NO
E cont	38.04	3.66e8	9-Octadecenamide	C18H35NO
G exp	44.92	3.84e8	1-Cholestene	C27H46
G cont	44.93	1.96e8	1-Cholestene	C27H46
E exp	44.92	1.25e8	1-Cholestene	C27H46
E cont	44.92	1.04e8	1-Cholestene	C27H46
G exp	48.67	1.22e10	Cholestanol	C27H48O
G cont	48.68	2.19e10	Cholestanol	C27H48O
E exp	48.52	0.87e10	Cholestrol	C27H46O
E cont	48.57	2.33e10	Cholestrol	C27H46O
G exp	56.94	10.86e8	Cholest	C33H54O3
G cont	56.93	2.21e8	Cholest	C33H54O3
E exp	56.92	6.68e8	Cholest	C33H54O3
E cont	56.88	1.18e8	Cholest	C33H54O3
G exp	60.84	0.35e10	Myristic acid	C16H30O2
G cont	61.14	1.05e10	Myristic acid	C16H30O2
E exp	60.88	5.39e10	Myristic acid	C16H30O2
E cont	61.01	6.36e10	Myristic acid	C16H30O2
G exp	61.48	2.29e8	Palmitic acid	C36H72O3
G cont	61.74	35.30e8	Palmitic acid	C36H72O3
E exp	61.50	7.69e8	Palmitic acid	C36H72O3
E cont	61.67	29.74e8	Palmitic acid	C36H72O3